Applied Physics Laboratory
University of Washington

1013 NE 40th Street
Box 355640
Seattle, WA 98105-6698

206-543-1300
FAX 206-543-6785
www.apl.washington.edu

29 December 2014

To: Dr. Robert Headrick, Code 32
Office of Naval Research
875 N. Randolph St, Suite 1425
Arlington, VA 2203-1995

From: Dajun Tang, Principal Investigator

Subj: ONR Grant # N00014-11-1-0188, "Mid-Frequency Reverberation Measurements with Full Companion Environmental Support."

Encl: (1) Final Report for the subject grant.
(2) Publications (seven).
(3) SF298 for above grant.

Please see the enclosures listed above, which constitute the Final Performance/Technical Report for the subject grant.

Dajun Tang

cc: Administrative Grants Officer, ONRRO Seattle
Grant & Contract Administrator, APL-UW
Office of Sponsored Programs, UW
Naval Research Lab, Code 5596
Defense Technical Information Center (electronic file with SF 298)

DISTRIBUTION STATEMENT A. Approved for public release; distribution is unlimited.

FINAL REPORT

MID-FREQUENCY REVERBERATION MEASUREMENTS WITH FULL COMPANION ENVIRONMENTAL SUPPORT

Dajun (DJ) Tang

Applied Physics Laboratory
University of Washington
1013 NE 40th Street
Seattle, Washington 98105

Phone: (206) 543-1290
Fax: (206) 543-6785
Email: djtang@apl.washington.edu

Sponsor: Office of Naval Research

Award Number: N00014-11-1-0188

Period of Performance:
1 November 2010 – 30 September 2014

Background and Scope:

Mid-frequency (1-10 kHz) shallow water acoustics is of important Naval interest, but had been an area where concentrated basic research was relatively lacking before the year 2000. This might have been a consequence that while long-range propagation (low frequency, 100's of Hz) dominated ASW work, direct-path (high frequency >10 kHz) found applications in MCM, leaving mid-frequency research being covered under either program, but without sufficient emphasis. As an outgrowth of APL-UW's high-frequency tradition, we started planning mid-frequency, shallow water research, approaching the subject by emphasizing contemporaneous environmental and acoustics studies in order to quantitatively understand dominant physical mechanisms. The major components of the research are transmission loss, bottom and sub-bottom impact on propagation and scattering, surface and water column influence on propagation, culminating in a full understanding of the physics of shallow water mid-frequency reverberation. Under this project, we conducted a series of theoretical and numerical studies, supplemented by existing data, to plan for a comprehensive shallow water reverberation experiment, which resulted in the TREX13 field project.

Modeling shallow water reverberation is a problem that consists of two-way propagation (including multiple forward scatter) and a single backscatter. In order to understand the reverberation problem at the basic research level, both propagation and scattering physics need to be properly addressed. Some aspects of reverberation are better treated stochastically ─ roughness scattering from the bottom and surface, for example. Other aspects can be more successfully treated deterministically, such as waveguide propagation and target scattering. Yet there are aspects where experience is limited, and the approach used to model them would likely be determined based on further empirical investigations. Scattering from fish schools and shipwrecks along with biological aggregates around them falls into this category. Clutter is a major issue and often unexplainable by known objects in the waveguide. We proposed a new hypothesis for clutter: Some of the clutter is due to the combination of (1) forward scattering of propagating sound from low-grazing angle to high-grazing angle, and (2) backscattering of the high-grazing angle energy, creating a target-like clutter because high-grazing angle backscatter is much greater than low-grazing angle backscatter.

Although there had been reverberation measurements at various frequencies, there had not been a true 6.1 level reverberation experiment where the environment has been sufficiently measured to support full modeling of the data. It is only after all components that contribute to reverberation are well measured and modeled that a true understanding of the reverberation problem can be achieved. During this funding period, we concentrated on making preparations for the TREX13 experiment, which included both theoretical development and data analysis.

Results

The main result of is work manifested in the successful field experiment, TREX13. While TREX13 had a broad design scope and covered almost all aspects of shallow water acoustics, a central theme based on a SONAR equation as given in Fig. 1 summaries the philosophy and general approach. The SONAR equation appropriate for the project is:

$$RL = SL - 2x\ TL + ISS$$

where RL is reverberation level, SL the source level, 2xTL the two-way transmission loss, and ISS the scattering strength integrated over the scattering patch for given sonar beam. Two unique features of TREX13 are that: 1) all components of the SONAR equation are designed to be individually measured in the same frequency band over the same environment, 2) an extensive environmental measurements at the appropriate temporal and spatial resolutions would be made such that basic research questions concerning predictability and uncertainty of shallow water reverberation can be quantitatively addressed. The approach to data analysis can be summarized into the following steps:

1. Based only on acoustic measurements, assess to what degree the measured reverberation, transmission, and scattering quantities satisfy the SONAR equation? This first step establishes a complete data set that enables detailed follow-up analysis. It also bounds the predictability and uncertainty of reverberation.

2. Incorporating environmental data, assess the predictability and uncertainty of the individual terms in the SONAR equation. Identify key environmental parameters that contribute to the variability.

3. Review available reverberation predictive models, and if necessary, develop new models to incorporate environmental knowledge in order to improve model accuracy and/or speed.

4. With both acoustics and environments measured, divide model environmental parameters into categories, e. g., those that can be inferred from acoustic data and those where databases are necessary.

5. Given prediction requirements and uncertainty tolerance, provide a set of key environmental parameters necessary as input to models.

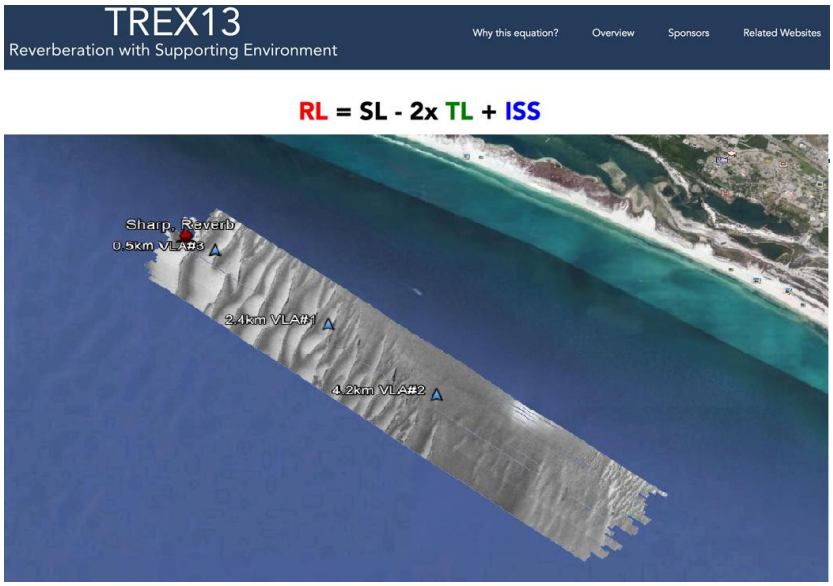

Figure 1. Schematic of TREX13 based on TREX13 website under development. The 400 kHz backscatter strength from the multibeam survey (de Moustier) is shown as the gray swath along the Main Reverberation Track where focused environmental characterization was conducted. Main acoustic assets are shown here: The reverberation sources and receiving arrays are deployed from the R/V Sharp and are labeled "Sharp, Reverb". The three vertical line arrays fielded by Scripps Institution of Oceanography are shown as triangles with labels given distances to the reverberation source.

Some of the specific results documented in the literature and are summarized as follows:

1. Shallow water reverberation modeling. A key question for evaluating reverberation models is speed vs. fidelity. Without fidelity, a model would not be able to make appropriate prediction; without speed, the model could not be effective in applications. During this funding phase, we developed a Monte Carlo reverberation model [2] based on PE and perturbation theory which allows incorporating specific environmental knowledge while still maintaining reasonable computational speed. The parabolic equation method is used to handle the two-way propagation, and first order perturbation theory is used to handle the backscatter. Because the calculation time is independent of the number of realizations, this method is much faster numerically than any models available. Another advantage of this method is that it can easily handle complications such as internal waves and swells.

2. Clutter is often considered to come from large scatterers. We hypothesized that reverberation clutter can often result from a combination of forward scatter and backscatter. As an example, we investigated the case where non-linear internal waves can change sound propagation path to high grazing angles, and those high angle sound would in turn be backscattered, resulting in a 'ghost' clutter' [1]. This line of investigation will continue in the analysis phase of the TREX13 data.

3. Transmission Loss is one of the major issues in shallow water acoustics because it is a quantity against which detection predictions are made. A couple of papers [5, 6] were devoted to this topic where influences of oceanographic variability are considered.

4. How to measure through either direct method or inversion techniques is a key to a successful for a 6.1field project because understanding the environmental impact on acoustics is the foundation for any quantitative analysis. A couple of papers [3,7] address the environmental issues, one concerns the inversion of geo-acoustic parameters from chirp sonar data, the other documents progress of a piece hardware which can take direct measurements on sediment sound speed and dispersion. Both techniques have been further developed during TREX13.

Now that the TREX13 field work has been accomplished, the next phase is to analyze the collected data and document the results. The anticipated areas of advances are shallow water transmission loss and reverberation clutters, both are areas having basic research and application needs.

PUBLICATIONS:

1. Henyey, F. S., and D. Tang, "Reverberation clutter induced by nonlinear internal waves in shallow water," *J. Acoust. Soc. Am.* **131**, EL302-308 (2013).

2. Tang, D. and D. R. Jackson, "Application of small-roughness perturbation theory to reverberation in range-dependent waveguides," *J. Acoust. Soc. Am.* **131 (6)**, 4428- 4441 (2012).

3. Tang, D. and B. T. Hefner, "Modeling interface roughness scattering in a layered seabed for normal-incident chirp sonar signals," *J. Acoust. Soc. Am.* **131**, EL302-308 (2012).

4. Yang, J., D. R. Jackson, and D. Tang, "Mid-frequency geoacoustic inversion using bottom loss data from the Shallow Water 2006 Experiment," *J. Acoust. Soc. Am.* **131 (2)**, 1711- 1721 (2012).

5. Henyey, F. S., K. L. Williams, J. Yang, and D. Tang, "Simultaneous nearby measurements of acoustic propagation and high-resolution sound speed structure containing internal waves", *IEEE J. of Oceanic Engineering*, Vol. 35, 684-694 (2010).

6. Yang, J., D. Rouseff, D. Tang, and F. S. Henyey, "Effect of the internal tide on acoustic transmission loss at mid-frequencies", *IEEE J. of Oceanic Engineering*, Vol. 35, 3-11 (2010).

7. Yang, J., D. Tang, and K. L. Williams, "Direct measurement of sediment sound speed in ShallowWater '06," *J. Acoust. Soc. Am.* **116**, EL116-121 (2008).

CrossMark

Reverberation clutter induced by nonlinear internal waves in shallow water

Frank S. Henyey and Dajun Tang
Applied Physics Laboratory, University of Washington, 1013 Northeast 40th Street, Seattle, Washington 98105-6698
frank@apl.washington.edu, djtang@apl.washington.edu

Abstract: Clutter is related to false alarms for active sonar. It is demonstrated that, in shallow water, target-like clutter in reverberation signals can be caused by nonlinear internal waves. A nonlinear internal wave is modeled using measured stratification on the New Jersey shelf. Reverberation in the presence of the internal wave is modeled numerically. Calculations show that acoustic energy propagating near a sound speed minimum is deflected as a high intensity, higher angle beam into the bottom, where it is backscattered along the reciprocal path. The interaction of sound with the internal wave is isolated in space, hence resulting in a target-like clutter, which is found to be greater than 10 dB above the mean reverberation level.

© 2013 Acoustical Society of America
PACS numbers: 43.30.Gv, 43.30.Hw, 43.30.Bp, 43.30.Cq [AL]
Date Received: June 17, 2013 **Date Accepted:** August 1, 2013

1. Introduction

One major factor hindering the performance of active systems is false alarms due to clutter. Clutter refers to target-like signals appearing in reverberation. Clutter has been attributed to strong backscattering strength from, for example, seafloor features[1] and fish schools.[2] Another possible mechanism for clutter, discussed in this paper, is a propagation effect, with ordinary backscattering strength. A sound speed feature, such as a nonlinear internal wave (NLIW) with large amplitude, deflects sound into the bottom as a beam, causing a higher insonification at a higher grazing angle, both aspects resulting in increased backscatter. We demonstrate that observed NLIWs in measured stratification can give a greater than 10 dB target-like return above the general reverberation level. For purposes of realism, our oceanographic and acoustic modeling is based on measured stratification and observed wave amplitudes on the New Jersey shelf during the SWARM experiment.[3] Ray tracing is performed that shows, qualitatively, the physical effect of deflection by the internal wave of sound into the bottom at higher grazing angle. A full wave model then gives quantitative results for the clutter.

2. Swarm NLIW model and ray tracing

Nonlinear internal waves are very common on the continental shelf where a thermocline exists. Several experiments, including SWARM, combining oceanography and acoustics have been carried out on the New Jersey shelf. Furthermore, this region is of continuing interest for additional experimental study in the near future, therefore, the predictions presented here could be investigated in future field programs.

The sound speed profile used for modeling is derived from a typical conductivity, temperature, and depth (CTD) cast from the SWARM experiment[3] and is shown in the left panel of Fig. 1, where a mixed layer extends down to 10 m. A warm salty layer near the bottom due to the shelf-break front resulted in a minimum in the sound speed at 35 m depth. This is a typical feature on the New Jersey coast and occurs in all SWARM and Shallow Water 2006 profiles[4] on the outer part of the shelf. In this

Author's complimentary copy

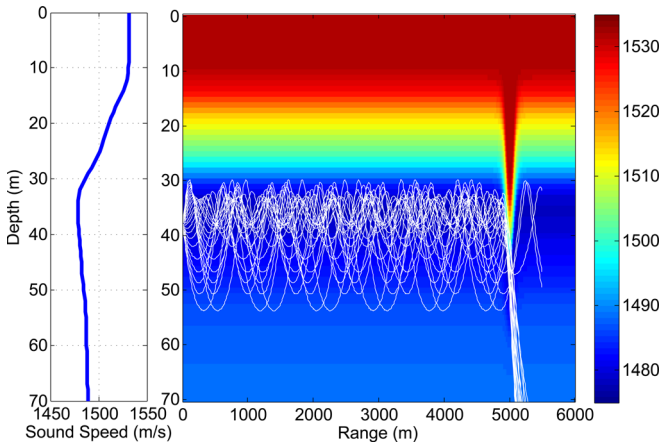

Fig. 1. (Color online) Sound speed profile (left), sound speed field with solitary wave at 5 km in color and superimposed ray trace with grazing angles within ±6 deg. Almost all rays are deflected into the bottom by the wave.

paper, we investigate the situation where a train of nonlinear internal waves approaches the acoustic source and receiver. In this case, the leading wave usually has the largest amplitude, and the sound speed profile is relatively range independent before reaching that wave. The effect of a leading wave of sufficient amplitude is to deflect the ducted sound near the sound speed minimum into a beam that strikes the bottom, leading to a target-like clutter signal. The subsequent behavior of that deflected beam depends on the details of the following waves in the train. Dispersion of the beam leads to lower and more time spread reverberation, unlikely to look like a target. Therefore, we model only the leading wave as a solitary wave, and ignore the following waves. The leading wave is almost a solitary wave, which we model as a solution of the fully nonlinear Dubriel-Jacotin-Long (DJL) equation (formerly referred to as Long's equation).[5] For a given stratification, the DJL equation has a set of one-parameter solutions. The amplitude of the wave used for modeling is chosen as typical of waves observed in SWARM and is shown as a sound speed field in color in Fig. 1 in the online version. The DJL equation models the two-dimensional structure of a NLIW of that amplitude much more accurately than does weakly nonlinear equations, such as the Korteweg-deVries equation. The wave is assumed to be at a 5 km range from the source and receiver in order to give quantitative clutter to reverberation.

To picture the mechanism, a set of rays was launched from a source at range zero and depth 38 m, close to the sound speed minimum. Figure 1 shows rays between ±6°, which stay in the sound channel and contribute to the clutter mechanism of this paper, although the detailed calculations to follow use an omnidirectional source, including propagation at the larger angles responsible for the reverberation at earlier times. When the rays encounter the solitary wave they are deflected to a higher angle of about 11 deg, and leave the channel as a beam, impinging onto the bottom. This beam, of higher grazing angle sound, is then backscattered around the reciprocal path to the receiver near the source, arriving as a strong target-like clutter signal. In order for this deflection of sound to occur, the amplitude of the internal wave needs to be large. Smaller wave would not change the direction of the propagating sound out of the channel. Ray tracing is unlikely to quantitatively predict this phenomenon for frequencies of a few kilohertz. Therefore, we resort to a full wave method in Sec. 3 for the quantitative study; however, ray tracing still offers an intuitive picture.

3. Reverberation and clutter

For quantitative results on reverberation, we resort to a full wave method to handle the two-way propagation, and perturbation theory for reverberation.[6] The bottom is

Author's complimentary copy

assumed to be a fluid half-space with sound speed of 1650 m/s, density of 2000 kg/m^3, and an attenuation of 0.5 dB/wavelength, so seabed absorption is included in the calculation. The acoustic field of an omnidirectional point source is expanded in unperturbed modes, and the equation for their evolution including mode coupling by the wave is solved following Eq. (29) of Ref. 7, where we make their forward-scattering approximation by dropping the second line and we refrain from expanding K^2 in the sound speed perturbation. Higher order modes were included in the calculation so the high angle waves from the point source are properly included. Alternatively, one could use another full wave approach, such as a parabolic equation method, to obtain the same results. We choose a point source of 3 kHz at the common choice of being near the sound axis; specifically, our source depth is 38 m. The solitary wave is at a range of 5 km, and extends the calculation to 10 km. Figure 2 shows the calculated horizontal flux. Before encountering the solitary wave, most of the sound energy propagating to long distances is trapped in the sound channel in the middle of the water column. At 5 km range, the internal wave converts most of the sound at low modes (small angle) to higher modes (larger angle), in a beam which interacts strongly with the seafloor. This result is qualitatively consistent with the ray analysis shown in Fig. 1. The deflected beam is refracted by the sound speed profile, periodically hitting the bottom. At these subsequent bottom interactions, the beam has significantly broadened.

Target-like clutter occurs when the narrow beam backscatters from the bottom. To calculate the reverberation and clutter, the rough seafloor backscatter model,[6] based on perturbation theory, is used. The water/sediment interface is assumed to have small-scale roughness with a typical roughness power spectrum as defined in the Office of Naval Research Reverberation Workshop.[8] The reverberation vs time is given in Fig. 3, with a 100 Hz bandwidth centered on 3 kHz. At slightly before 7 s, corresponding to the range where the deflected rays of Fig. 1 hit the bottom, a large arrival appears more than 10 dB above the background reverberation level with a time spread consistent with the inverse bandwidth of the transmitted pulse. Additional calculations with twice the bandwidth around the same center frequency show a 2-dB increase of the clutter arrival while the width remains to be consistent with the inverse bandwidth. The large return is the result of both larger insonification at the place the deflected beam strikes the bottom and the stronger backscatter at higher grazing angles. Because the deflected sound behaves like a narrow beam impinging onto the bottom, the arrival shows up like a target. Following the large arrival, the reverberation is generally higher

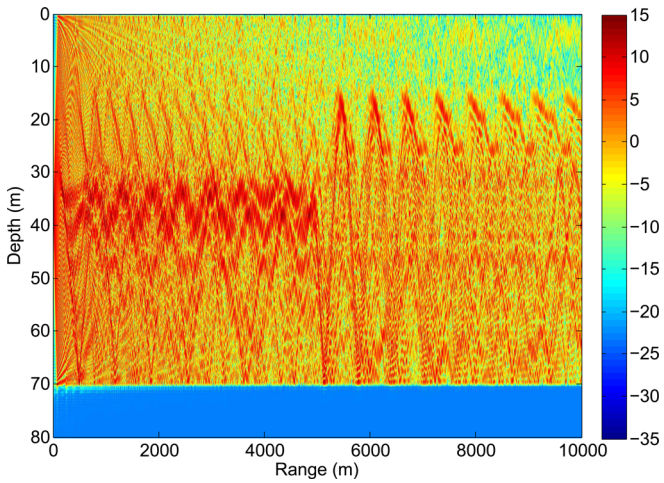

Fig. 2. (Color online) Horizontal intensity flux of one way coupled mode solution at 3000 Hz. Source at 38 m depth and zero range, water column sound speed field as in Fig. 1, and sediment parameters given in text.

Author's complimentary copy

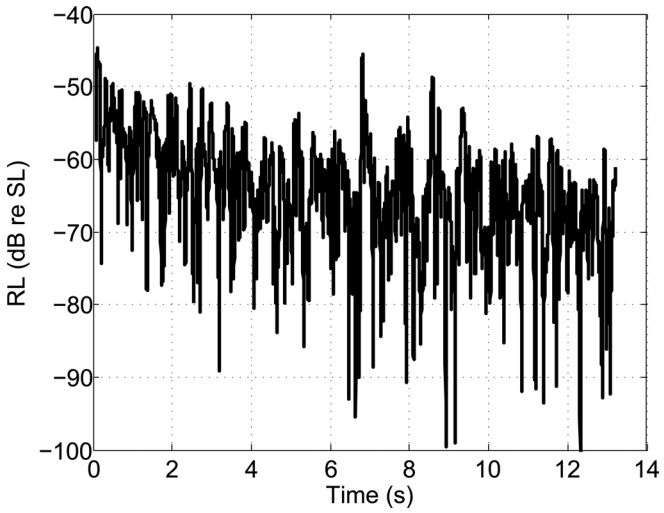

Fig. 3. Monostatic reverberation level normalized to source level and as a function of time with a point source at 38 m, 5000 m away from the solitary wave.

than the level extrapolated from before the arrival of the internal wave. There are additional individual arrivals due to the repeated interaction of the deflected beam with the bottom. However, even in the absence of the rest of the wave train, they are more spread out in time and smaller in amplitude than the first peak because of the spreading of the deflected beam.

4. Discussion

Nonlinear internal waves are a common phenomenon on the continental shelf when strong stratification exists. Under the right conditions, such a wave induces a false target in an active system due to strong insonification at high angle of the bottom just behind the deflecting wave. Considering typical internal waves on the shelf move at a speed of order 1 m/s, the induced false target could be tracked as a slowly moving target. When the source is near the channel minimum, as was shown in the previous calculation, the effect is most pronounced; a source outside the duct does not have as dramatic an effect. To experimentally verify the effect presented, a monostatic reverberation system properly placed in the duct aimed toward the oncoming nonlinear internal waves, and a means of monitoring the location of such waves, such as radar or visual, would suffice.

Acknowledgments

This work was supported by the Office of Naval Research.

References and links

[1]D. A. Abraham and A. P. Lyons, "Novel physical interpretations of *K*-distributed reverberation," IEEE J. Ocean. Eng. **27**(4), 800–813 (2002).

[2]D. E. Weston and J. Revie, "Fish echoes on a long-range sonar display," J. Sound Vib. **17**, 105–106 (1971).

[3]J. R. Apel, M. Badiey, C.-S. Chiu, S. Finette, R. Headrick, J. Kemp, J. F. Lynch, A. Newhall, M. H. Orr, B. H. Pasewark, D. Tielbuerger, A. Turgut, K. von der Heydt, and S. Wolf, "An overview of the 1995SWARM shallow water internal wave acoustic scattering experiment," IEEE J. Ocean. Eng. **22**, 465–500 (1997).

[4]D. Tang, J. N. Moum, J. F. Lynch, P. Abbot, R. Chapman, P. H. Dahl, T. F. Duda, G. Gawarkiewicz, S. Glenn, J. A. Goff, H. Graber, J. Kemp, A. Maffei, J. D. Nash, and A. Newhall, "Shallow Water'06: A joint acoustic propagation/nonlinear internal wave physics experiment," Oceanogr. **20**(4), 156–167 (2007).

Author's complimentary copy

[5]A. Turkington, A. Eydeland, and S. Wang, "A computational method for solitary internal waves in a continuously stratified fluid," Stud. Appl. Math. **85**, 93–127 (1991).
[6]D. Tang and D. R. Jackson, "Application of small-roughness perturbation theory to reverberation in range-dependent waveguides," J. Acoust. Soc. Am. **131**(6), 4428–4441 (2012).
[7]L. B. Dozier and F. D. Tappert, "Statistics of normal mode amplitudes in a random ocean. I. Theory," J. Acoust. Soc. Am. **63**(2), 353–365 (1978).
[8]E. I. Thorsos and J. Perkins, "Overview of the reverberation modeling workshops," in *Proceedings of the International Symposium on Underwater Reverberation and Clutter* (2008), pp. 3–22.

Author's complimentary copy

Simultaneous Nearby Measurements of Acoustic Propagation and High-Resolution Sound-Speed Structure Containing Internal Waves

Frank S. Henyey, Kevin L. Williams, Jie Yang, and Dajun Tang

***Abstract*—During the 2006 Shallow Water (SW06) experiment, simultaneous measurements were made of the sound-speed field as a function of range and depth associated with nonlinear internal waves and acoustic propagation at frequencies of 2–10 kHz over a 1-km path. The internal waves were measured by a towed conductivity–temperature–depth (CTD) chain to get high resolution. These measurements were coordinated so that the nonlinear waves could be interpolated onto the acoustic path, allowing predictions of their effects on the acoustics. Using the measured sound-speed field, the acoustic arrivals under the influence of the internal waves are modeled and compared to data. The largest impact of measured moderate amplitude internal waves on acoustics is that they alter the arrival time of the rays which turn at the thermocline.**

***Index Terms*—Acoustics propagation, conductivity–temperature–depth (CTD) chain, nonlinear internal waves.**

I. Introduction

THE 2006 Shallow Water (SW06) experiment was a major field effort conducted in July–September 2006 off the coast of New Jersey, involving ships, moorings, aircraft, and satellite coverage, as well as modeling [1]. Topics in ocean acoustics, physical oceanography, and marine geology were studied. Oceanographically, the shelfbreak front, the local eddy field, and the nonlinear internal wave field were of interest. Acoustically, SW06 included both low-frequency (50–1600 Hz) and midfrequency (1600–20 000 Hz) components, and examined issues in forward propagation, scattering, and inverse theory. For acoustics transmissions, both moored and shipboard sources and receivers were used. The low-frequency component concentrated on two issues: geoacoustic inversion and azimuthal dependence of shallow-water sound propagation, specifically its strong dependence upon the angle between the acoustic path and the propagation direction of the nonlinear internal wave field. The midfrequency efforts of SW06 were concentrated on receiving arrays moored in the central area where the water depth is about 80 m. In this central area, extensive environmental measurements were made to support midfrequency acoustics. Measurements include short-range acoustics interaction with the bottom and surface, short-range propagation through internal waves, and longer range propagation to 10 km along the same track with multiple source depths, frequency bands, and times. The location of the nominal center of the experiment was 39° N, 73° W. In this paper, we choose this point to be $(x, y) = (0, 0)$ with x pointing to the east and y pointing to the north. One of the major themes of the program was highly nonlinear internal waves (NLIWs). While oceanographic studies were concerned with the creation, propagation, and decay of those waves, acoustic studies were concerned with their effects on propagation. This paper reports a study of sound propagation through NLIWs, which were concurrently measured to enable deterministic model/data comparisons. This study was originally planned for August 11, but it turned out (very unusually) that no mode 1 NLIWs were observed near the experimental site that day. It was rescheduled, and performed on August 13.

The impact of internal waves on sound propagation in coastal areas has been studied quite extensively in the past two decades. For examples, SWARM [2] on the New Jersey shelf north of the SW06 site, the Slope to Shelf Primer [3], and the 2001 Asian Sea International Acoustics Experiment (ASIAEX) in the South China Sea [4]. These programs have concentrated on propagation of low-frequency sound (<1 kHz) [5]. Mode conversion and acoustic propagation in directions other than the NLIW propagation direction dominate these low-frequency studies.

One part of SW06 was designed to provide sufficient oceanographic measurements of NLIWs so that the 2-D sound-speed fields (range and depth) in the acoustic path at the time of sound transmissions could accommodate deterministic modeling of the effects of NLIWs on sound propagation. The instrument used for measuring these NLIWs was a towed conductivity–temperature–depth (CTD) chain, which provides a 2-D sound-speed field over time. The towed CTD chain data are augmented by conventional CTD casts.

Under the usual summer conditions with a thinner warm upper mixed layer, a strong thermocline, and a thicker, less stratified lower layer, NLIWs are waves of depression. In SW06, the waves had the common property of coming in wave trains with larger waves tending to occur near the front of the train [1, Fig. 2]. NLIWs in the experiment moved with a speed between 0.5 and 1.0 m/s, and had horizontal widths perpendicular to the propagation direction of the NLIW on the order of 100 m. These result in variations of sound propagation over time. To model such variations, the sound-speed field along the

Manuscript received May 28, 2009; revised December 11, 2009; accepted February 22, 2010. Date of publication August 26, 2010; date of current version November 30, 2010. This work was supported by the U.S. Office of Naval Research.

Associate Editor: J. F. Lynch.

The authors are with the Applied Physics Laboratory, University of Washington, Seattle, WA 98105-6698 USA (e-mail: frank@apl.washington.edu).

Color versions of one or more of the figures in this paper are available online at http://ieeexplore.ieee.org.

Digital Object Identifier 10.1109/JOE.2010.2044671

0364-9059/$26.00 © 2010 IEEE

acoustic path must be known as a function of time. The speed and spatial structure of the NLIWs make it impractical to move a single CTD vertically through the water fast enough to resolve a wave's structure well. Multiple CTDs positioned vertically are needed for good resolution. They can either be mounted on a mooring or lowered from a ship or float. Viewed from the reference frame moving with the wave, the wave's evolution over time is slow. Hence, a towed chain has the advantage over a mooring because the slow wave evolution can be measured (and was in SW06), in addition to the rapid time dependence with the wave speed.

The planning of the acoustics experiment was based on historical NLIW data on the New Jersey shelf in the summer. The summer sound-speed profiles of the area typically have a relatively thin mixed layer near the surface with a high sound speed, a thin thermocline to reach a minimum sound speed, and a thicker region of less variable sound speed extending to the bottom. At the time and place of concern in this paper, as frequently happens in this area, a warm, salty bottom layer intruded from off the shelf, making the sound-speed gradient near the bottom somewhat higher than with an adiabatic profile. The result is a sound channel with higher speed both near the surface and near the bottom. Such a channel favors propagation and reduces the influence of the surface and bottom, especially if the sound source is placed near the sound axis. At the experimental site, the water depth is 80 m. The sound axes varied in depth from 30 to 40 m during the experiment.

Acoustic intensity fluctuations are largely due to spatially small sound-speed perturbations, and a deterministic interpolation of such perturbations is unlikely to give correct results. Rather, we concentrate on phenomena sensitive to large spatial scales, which are associated with the travel time of acoustic arrivals.

Historical oceanographic data suggested that NLIWs in the area come in trains [2] with spacing on the order of 100 m and they propagate from the southeast to northwest generally in the direction along a 300° compass bearing.

The sound source and receiver were separated by 1000 m along the 300° compass direction. The CTD chain, towed by the *R/V Endeavor*, circled close to the acoustic path, typically 200 m from the path, while midfrequency sound propagation data were collected. The tow track is shown in Fig. 1 together with the source and receiving array positions. The source was suspended from the stern of the *R/V Knorr* that was dynamically positioned at 39.0203° N, 73.0277° W, facing due north, putting the source at $(x, y) = (-2.3999, 2.2133)$ km, 40 m due south of the global positioning system (GPS) position. The receiving array, moored at 39.0245° N, 73.0377° W, is about 1000 m from the source, at a bearing of 300°. During this joint acoustic/oceanographic measurement period, NLIWs crossed the acoustic path, allowing the study of their impact on sound propagation.

In the following, we first present the oceanic and acoustic data in Section II, and then in Section III, we model the oceanic data to interpolate the sound-speed field onto the acoustic path. In Section IV, we model the acoustic propagation through the sound-speed field. In Section V, we attempt to interpret the systematic features of acoustic arrivals using ray trace ideas. We finish with a discussion in Section VI.

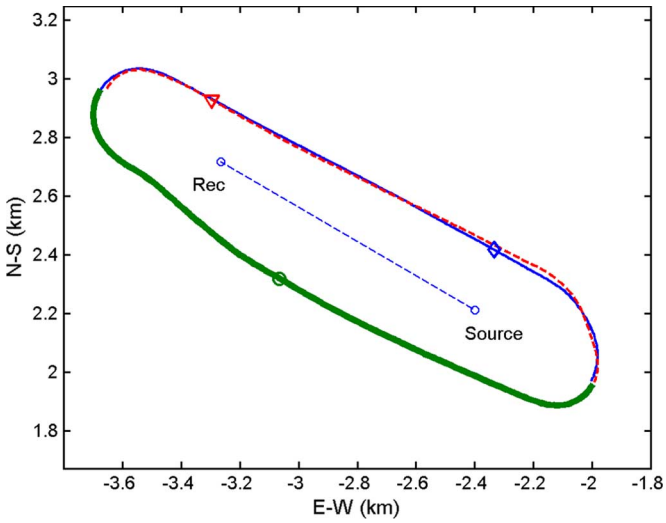

Fig. 1. Positions of the acoustic and oceanographic measurements. Distances are relative to longitude 73°W and from 39°N. The *R/V Endeavor* track, 16:42:00Z to 17:15:00Z August 13, circling around the acoustic source and receiving array. Thin solid line: leg 1, 16:42:00Z to 16:53:00Z ; thick solid line: leg 2, 16:53:00Z to 17:04:00Z; and dashed line: leg 3, 17:04:00Z to 17:15:00Z. Encounters with the center of the first wave are indicated by the diamond, circle, and triangle for legs 1, 2, and 3, respectively.

II. Experimental Data

A. Oceanic Data

During the acoustic transmissions, the density and sound speed were measured by a CTD chain towed by the *R/V Endeavor*.

The towed CTD chain system comprises a set of individual CTD fins arranged on a single cable that is towed behind a ship. The chain is deployed from a 2-m diameter divided drum. To facilitate recovery, the drum is optimally situated so that the fins come off the bottom of the drum, allowing the fins to orient themselves properly with the drum during recovery. The chain threads through a specially designed block suspended from the A-frame. To maximize the chain depth while towing, a large V-wing depressor is attached to the end of the chain cable.

The CTD fins are molded rubber approximately 190 mm long by 100 mm tall with a rounded body that tapers from 50 to 30 mm. The insulated cable acts as both strength member for towing and as power/communication line for data collection. Individual sensors are threaded onto the tow cable through a hole parallel to the 100-mm side, at the wide end of the body. The sensors are free to rotate around the cable so that they self-align to decrease drag while being towed. The sensors are distributed along the wire according to the number of sensors available and the desired sampling in depth. They are held in place using split collars clamped to the cable 5 mm above and below each sensor. Each CTD fin contains sensors to measure pressure (P), temperature (T), and conductivity (C). Power and data transmission are achieved through inductive coupling of each sensor with the tow cable.

As configured on August 13, 48 sensors were spaced about 1 m vertically (1.5 m along the slant of the chain), and the chain was towed at about 6 kn. GPS positions and time and the measured pressure converted to depth are used for the determination

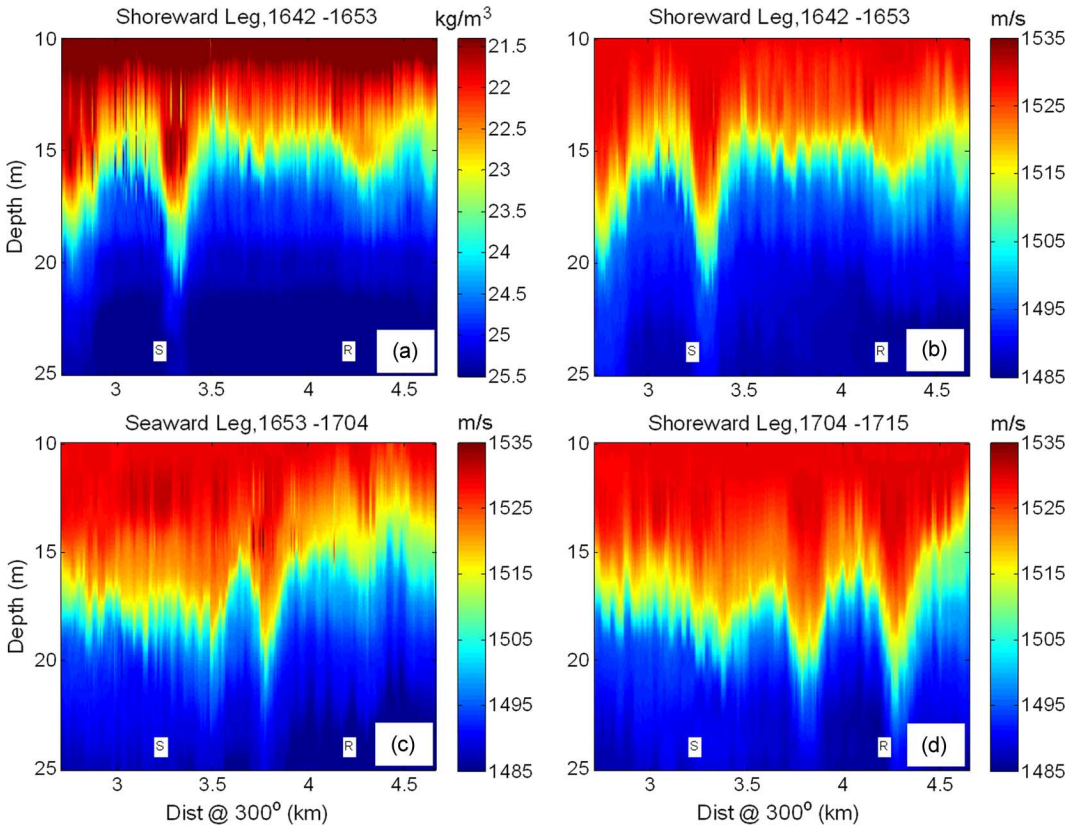

Fig. 2. Fields obtained from the towed CTD chain. (a) Density -1000 kg/m^3 on the first shoreward leg (leg 1); (b) sound speed corresponding to (a); (c) sound speed from seaward leg (leg 2); (d) sound speed from the second shoreward leg (leg 3). The source and receiver locations relative to the waves are also shown for each leg. The density and sound speed show the same features, except that the density shows calibration inaccuracies. Similar relationships, not shown, hold on the other two legs. We use sound speed as a surrogate for density. The same two nonlinear internal waves show up on all three legs.

of the actual sensor positioning. The measurements dedicated to acoustics lasted for 2.5 hours, during which the CTD chain was towed in seven circuits around the propagation path. At this time, there were two simultaneous trains of NLIWs along the acoustic path. These two trains merged into one train along a line that passed a short distance southwest of the circuits, and the merge was clearly visible from the *R/V Endeavor* from which the CTD chain was deployed. After the acoustics support phase, the *R/V Endeavor* proceeded northwest to the merge region of the fronts of the trains, to study the merging process.

One and a half circuits (which we call three legs shown in Fig. 1) in the middle of this time period are selected for analysis, as the large waves at the front of the packets passed the acoustic path during this time.

The legs extended some distance beyond the source and the receiver. This was done so that the chain would have a constant shape and be directly behind the *R/V Endeavor* when the track was along the acoustic path. The measured density and sound speed on the first leg are shown in Fig. 2(a) and (b). The sound speed is nearly a unique function of the density; very little "spice" variability occurs. This is true of the other two legs as well, and only the measured sound speed is shown in Fig. 2(c) and (d). By comparing Fig. 2(c) and (d) to their corresponding densities, we find that they also have very little "spice" variability and the sound-speed-density relation is the same as that of the first leg. Two large waves are seen in all three legs. The spacing between these waves is the same in the first and third legs, but is less in the second leg, even after accounting for the relative motion of the ship and the waves on all legs. The shape of the second wave is also different in the second leg. The second leg is 400 m to the southwest of legs 1 and 3, closer to the merging region of the wave trains, so these differences are along-crest variability of the waves.

One profile taken at 15:30:00Z on August 13 with the ship's CTD on the *R/V Knorr* is important in our analysis. This profile was taken at the approximate location of the acoustic source in our experiment, and is shown in Fig. 3(a). For reasons of cost, CTD units on the towed chain are not as high quality as a ship's CTD. Accuracy, reliability, and calibrations (especially relative calibrations between different fins) are issues that have not been adequately resolved for detailed quantitative use. Therefore, the ship's CTD profile was used to complement the towed chain data in obtaining the sound-speed field for acoustics simulations. The method of combining the data is described below.

B. Acoustic Data

The acoustic range is nominally 1000 m, the source was positioned at 30 m depth, and the receiver used in this analysis was 25 m deep. The total water depth is 80 m at the experimental site. The acoustic source was deployed from the stern of the *R/V Knorr*, which was dynamically positioned at a fixed point. The acoustic path was at a bearing of 300°. Because of the

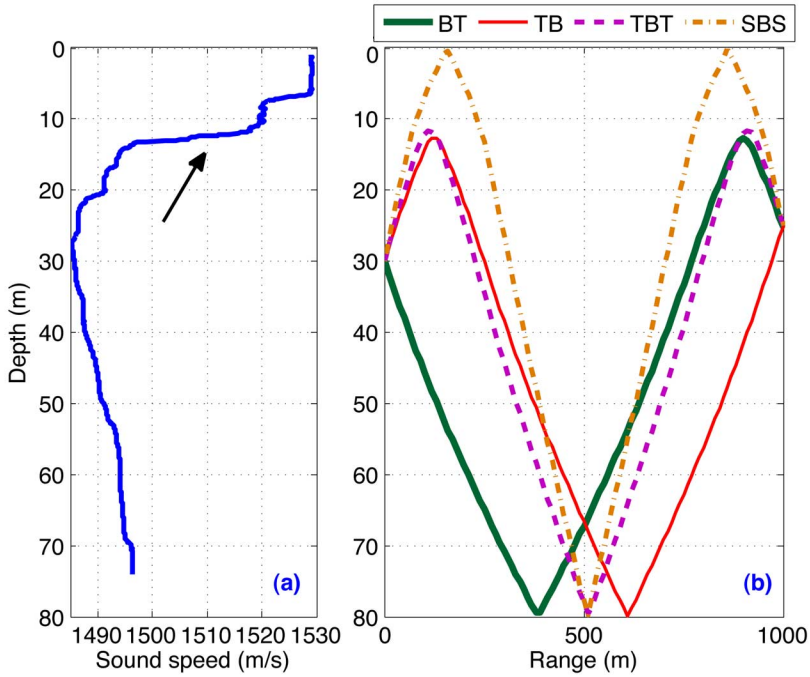

Fig. 3. (a) Sound speed from a CTD profile taken at 15:30:00Z on August 13 near the source position as given in Fig. 1. The arrow points to 1510 m/s, which is used to define the thermocline depth. Small errors in this sound-speed value in the towed chain measurement would make little difference to the thermocline depth. (b) Rays between the source and the receiver using a range-independent sound speed extracted from this CTD profile. The rays are named bottom-turn (BT), turn-bottom (TB), turn-bottom-turn (TBT), and surface-bottom-surface (SBS).

source deployment method, there is an uncertainty of $O(1\text{ m})$ in the acoustic range.

The transmitted acoustic signal spanned the frequencies 1.5 and 10.5 kHz. A set of direct-path propagation data was collected at the 50-m range as calibration, so the transmitted waveforms were known. In the frequency band, the source has a 10-dB notch near 6 kHz. However, because the signal-to-noise ratio (SNR) was high at the 1-km range, data from the full band can be utilized. The pulse was compressed by dividing the Fourier transform of the received pulse by the Fourier transform of the sent pulse and multiplying by $\sin(\pi((f - 1.5\text{ kHz})/9\text{ kHz}))$ between 1.5 and 10.5 kHz. The time resolution is estimated as the full width at half maximum intensity of this compressed analytic signal, which is 0.13 ms. The sidelobes are down by 23 dB.

Acoustic transmission started at 14:14:00Z and ended 18:49:00Z on August 13 with a nominal 14-s ping repetition rate, resulting in 1100 pings recorded. The uncertainty of the source position excluded the possibility of coherent ping-to-ping processing and motivated use of the highest arrival of each ping as reference time zero to line up all the pings. The highest arrival almost always occurred during the arrival of sound propagating near the minimum sound-speed depth. Internal waves have little effect on the sound speed near its minimum, making this a good reference. We define the reduced travel time as the actual travel time shifted by the amount corresponding to the reference time. In Fig. 4, acoustic arrival intensity for the 25-m receiver is plotted against geotime on the vertical axis and the reduced travel time on the horizontal axis for all the transmissions.

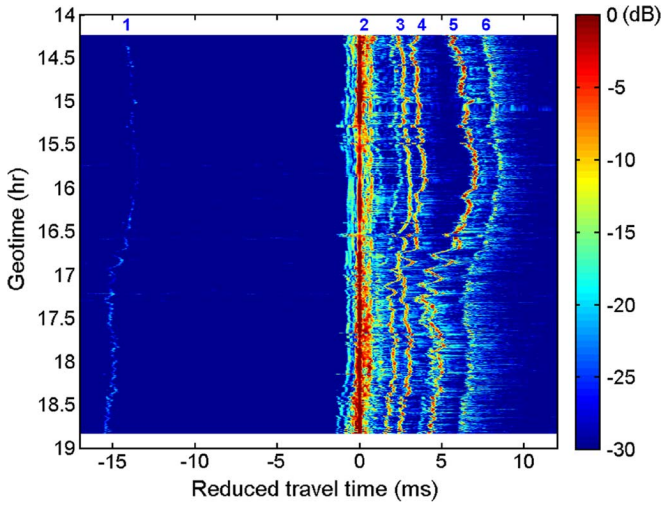

Fig. 4. Acoustic intensity level during this experiment. The level is relative to the highest intensity observed during this period. Six arrivals are labeled near the top of the figure. Arrival #1 is a faint arrival that has propagated through the surface mixed layer, arrival #2 is the direct arrival used to define the reduced travel time, and arrivals #3–#6 are the arrivals associated (by travel time) with the rays of Fig. 3(b). The correspondence is #3 = BT, #4 = TB, #5 = TBT, and #6 = SBS. The oscillations in arrival time around 16:30:00Z, most clearly seen in arrival #5, are the primary concern of our modeling.

In the 30-ms time window shown in Fig. 4, six separated arrivals are identified and labeled. Between geotime 14:20:00Z and 16:00:00Z, before the waves are present, the arrival structure is relatively stable: arrival #1 being very weak at about −15 ms, followed by arrival #2 with the highest amplitude defining 0 ms, in turn followed by arrivals # 3, #4, and #5,

between 2 and 5.5 ms, ending by a weaker arrival #6 at about 7.0 ms.

Ray tracing was performed using a sound-speed profile from a CTD cast from the *R/V Knorr* at 15:30:00Z geotime as given in Fig. 3(a) to identify the different arrivals. The rays associated with each of the labeled arrivals in Fig. 4 based on travel time are as follows. Arrival #1, a faint arrival, is a ray leaving the source upward, traveling near the surface, and reaching the receiver going downward. Arrival #2, with the highest amplitude, is a superposition of two kind of rays; the first kind is a group of axial arrivals traveling close to the sound axis at 30-m depth without reaching the high gradient part of the thermocline and the second kind is a ray labeled B in the convention of Fig. 3, leaving the source downward, bouncing off the bottom once then reaching the receiver upward. The two kinds of arrivals reach the receiver spread out in time over 1 ms, hence are not resolved. The next four labeled arrivals are identified with the rays shown in Fig. 3(b). Arrival #3 starts downward, bounces once off the bottom, then turns downward in the thermocline, reaching the receiver going downward (BT). Arrival #4 can be considered a reciprocal of arrival #3, which starts upward, turns downward in the thermocline, then bounces at the bottom, reaching the receiver going upward (TB). Arrival #5 is a ray that has two upper turning points and one bottom bounce between them (TBT). Arrival #6 is a ray bouncing twice at the sea surface and once at the bottom (SBS).

The arrivals in Fig. 4 have a changing structure versus geotime. They tend to get closer to one another starting from about 16:30:00Z. Notably, three of the arrival times have oscillatory patterns. The "TBT" arrival has four fluctuations to earlier arrival times, whereas the "BT" and "TB" arrivals have two such fluctuations in each. However, the arrival "SBS," though it has a similar ray path to "TBT," does not show apparent fluctuations in its arrival time. In addition, the overall spread in arrival times is reduced by about 1 ms after 16:30:00Z, with the reduction occurring between arrivals #4 and #5.

III. Environmental Modeling

The first step of modeling the sound-speed field is to interpolate the CTD chain data in space and time to estimate the positions of the waves along the acoustic path. The wave speeds, their directions, and their time crossing a reference position [which we extrapolate to $(x, y) = (0, 0)$] need to be determined. The observed spacing between the waves on the two shoreward legs is nearly the same (and the ship speed was the same), so the two waves are traveling at about the same speed. The wave speed in the direction of the acoustic path is primarily determined by the position and time spacing between the observations of the same wave on consecutive shoreward passes. The wave widths, and the distance between them, differ from the raw observation because the ship speed is only several times the wave speed. The wave propagation directions also depend on the measurements on the seaward leg. Rather than a sequential determination of the parameters, we fit all simultaneously from the data on all three legs and interpolate to the acoustic path, avoiding assumptions such as that the tow path be exactly parallel to the acoustic path.

There is a complex structure at smaller scales than the two waves, and it is unlikely that the smaller structure is traveling in the same direction with the same speed as the large waves. Thus, we only want to interpolate the large scale features. We define the center of the thermocline by sound speed $= 1510$ m/s, as indicated in Fig. 3(a). We refer to the depth at which this is the sound speed as the "thermocline depth." For every towed chain measurement (every 2 s), we estimate the thermocline depth. We then lowpass filter the resulting time series of depths to eliminate the small waves. This lowpass filter also eliminates about 0.30 m from the deepest excursions of the large wave (where the smallest horizontal scales occur), and this extra depth was replaced at the end of the processing.

In each case, the lowpass curve intersects the raw curve near the places where the curves are 2 m above the deepest point on the lowpassed first wave. For each leg, these points are taken to define the front and the back of the two waves, except that the back of the second wave can only be determined on leg 3. On leg 1, the back was outside the tow path, while on leg 2, the thermocline stayed deep for some distance behind the second wave. It is assumed that the front and the back of the first wave and the front of the second wave move at constant speed and they form straight lines. The three legs provide exactly enough information to solve for each speed, direction, and position of each wave feature examined. Table I summarizes the solutions. The propagation directions are a little more northward than the 300° assumed in pre-experiment modeling, as were most of the waves observed in SW06. The intersections of the lines with the acoustic path are the modeled positions of those features along that path. The speeds as observed along the path of all three points are nearly the same, so we use their average, 0.6447 m/s, fixing the positions at the time 16:59:00Z, when the waves were near the center of the acoustic path. The maximum difference of any feature on the acoustic path between using the individual speeds and using the average speed was only 15 m. Finally, the assumed back of the second wave was chosen so that the ratio of widths of the two waves was the same as the ratio observed on the third leg, very nearly parallel to the acoustic path. The center of each wave is placed half way between its front and back.

In addition to the two waves shown in Fig. 2, the towed chain data show a change in the thermocline depth, which changed from about 15 m before the waves to about 17 m after the wave. These estimates ignore smaller waves that appear in the data, but cannot be connected between the different legs. This change of thermocline depth is the solibore aspect of a train of NLIWs, as discussed by Henyey and Hoering [6]. Between the two waves, the lowpass curve shows the thermocline depth at about 16 m, half way through the bore. The thermocline depth at the centers of the waves is linearly interpolated between the lowpass values on the three legs, with an extra depth of 0.30 m added. This extra thermocline depth makes its integral between the front and the back of the first wave very nearly equal to that of the raw curve on each of the three legs. Thus, we have seven points specified on the thermocline depth, as well as the two asymptotes. With the seven points on the curve identified, plus the two asymptotes, the remainder of the curve is obtained by Hermite interpolation using the algorithm of Fritsch and Carlson [7]. This method places the local extrema at the centers of the waves and

TABLE I
PARAMETERS OF MEASURED NLIW FEATURES INFERRED FROM THEIR OBSERVATION BY THE TOWED CTD CHAIN ON THREE LEGS. THE LAST ROW IS SPEED AS OBSERVED ALONG THE ACOUSTIC PATH AT A BEARING OF 300°. THEY ARE DEDUCED FROM THE SPEED AND WAVE BEARING IN ROWS 1 AND 2. THE WIDTH OF THE SECOND WAVE BETWEEN FRONT AND BACK IS ASSUMED TO HAVE THE SAME RATIO TO THE WIDTH OF THE FIRST WAVE AS OBSERVED ON LEG 3

	Front of first wave	Back of first wave	Front of second wave
Speed	0.587 m/s	0.606 m/s	0.564 m/s
Bearing	324.3°	316.8°	331.4°
Extrapolated time at 73°W, 39°N	15:14:26Z	15:19:57Z	15:23:01Z
Speed along acoustic path	0.643 m/s	0.632 m/s	0.658 m/s

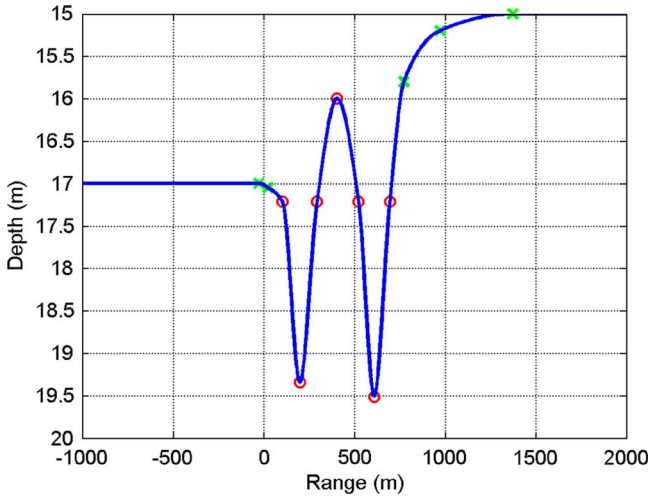

Fig. 5. Model of the thermocline depth (at 16:59:00Z) defined by sound speed = 1510 m/s as a function of range obtained by interpolating the towed chain data onto the acoustic path. Circles: interpolated points using the tow chain data; crosses: auxiliary points selected to make the curve smooth. At the reference time 16:59:00Z, the source is at range 0 m, and the receiver is at 1000 m.

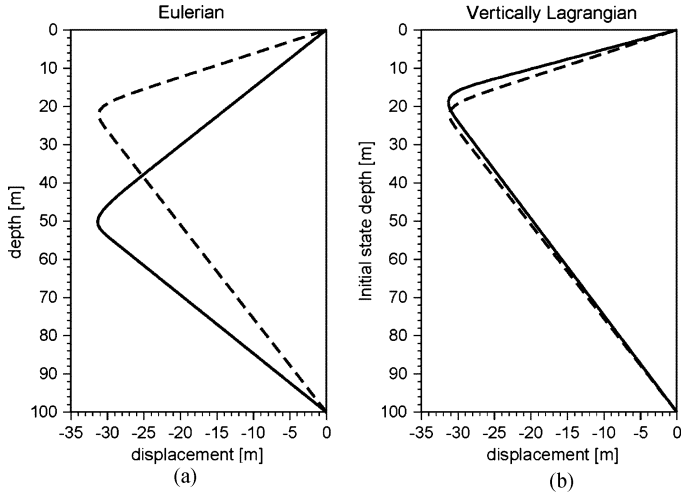

Fig. 6. True displacement (solid) at the center of a large NLIW compared to the linear displacement (dashed) (a) in the Eulerian reference frame and (b) in the Lagrangian reference frame. The Lagrangian reference frame is clearly a much better choice in which to use the linear mode displacement.

at the 16-m point between the waves, as we intend. To ensure a smooth transition from the waves to the asymptotes, five auxiliary points were added in. Fig. 5 shows the result of this interpolation.

Given the thermocline depth as a function of the horizontal position and time, we complete the specification of the sound speed using the data from the CTD profile at 15:30:00Z. We assume that the vertical displacements from that profile are linear mode 1 in a vertically Lagrangian coordinate system, i.e., $c(x, z_0 + \alpha(x)\varphi_1(z_0)) = c_0(z_0)$, where φ_1 is the mode 1 displacement eigenfunction and $c_0(z_0)$ is the sound-speed profile, both from the CTD profile at 15:30:00Z. This assumption is rather accurate for NLIWs when the profile has a sharp thermocline with relatively little stratification above and below [13]. Such a quasi-2 layer profile describes well the conditions during our experiment. Following [13], Fig. 6 compares the linear mode 1 eigenfunction with the displacement at the center of a large NLIW in two coordinate systems, demonstrating the superiority of using the linear displacement in the vertically Lagrangian coordinate system over that in the Eulerian coordinate system. A vertically Lagrangian coordinate system is also appropriate in other internal wave cases [8]. The strength of the linear wave function at each value of $x - vt$ is chosen to place the thermocline depth on our interpolated curve. This model sound-speed field at 16:59:00Z is shown in Fig. 7.

IV. ACOUSTIC MODELING

The acoustic data show that when an NLIW train goes through the acoustic path, different arrivals experience different degrees of variations. The most apparent variation is that some of the arrivals show oscillatory arrival time on the order of 1 ms, whereas others do not. To understand the observed change, both broadband Collins-type "parabolic equation" (PE) [9] and ray tracing techniques are used to simulate acoustic propagations in this changing environment. While ray tracing

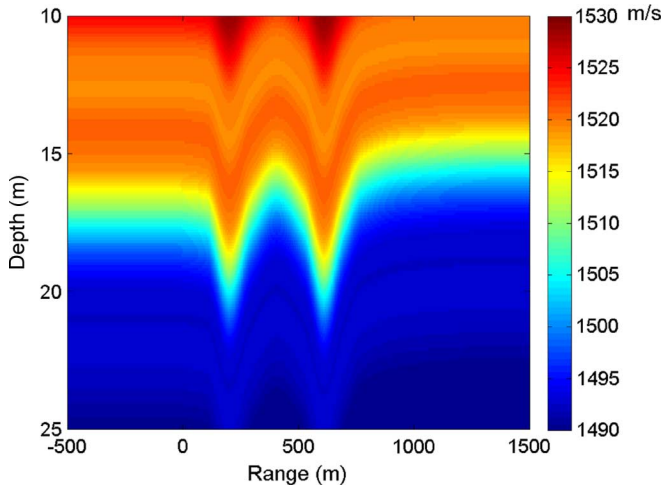

Fig. 7. Sound-speed field generated using the thermocline depth shown in Fig. 5. The vertical dependence at each point is assumed to be given by a vertically Lagrangian mode 1 displacement of the profile shown in Fig. 3(a). At the reference time 16:59:00Z, the source is at range 0 m, and the receiver is at 1000 m.

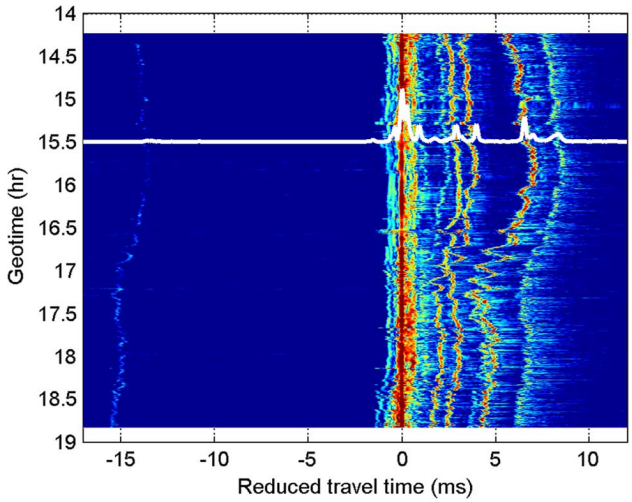

Fig. 8. Comparison of acoustic data with a range-independent broadband PE simulation based on the profile in Fig. 3. The arrivals are well fit at the time of the profile; no NLIWs were present at that time. Even the faint arrival at −15 ms is fit.

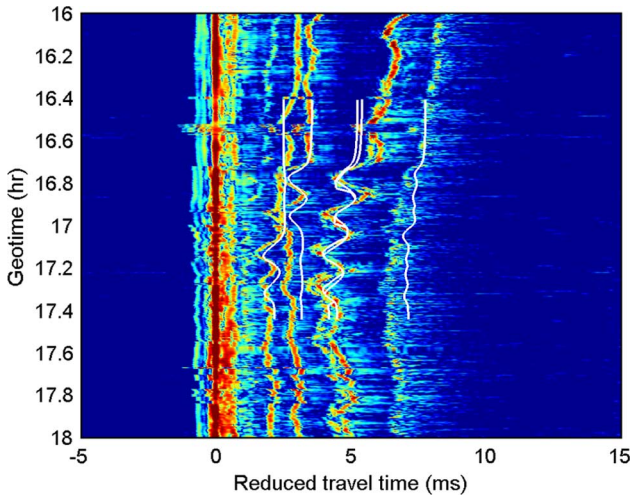

Fig. 9. Comparison of acoustic data with ray tracing results for arrivals (from left to right as indicated by the white curves): TB, BT, TBT, and SBS between 16:24:00Z and 17:26:00Z. Only one overall reference time was adjusted, as the axial arrival was not modeled. The times, temporal extent, and magnitude of travel time oscillations were deterministically calculated, and are close to the measured values.

has the advantage of providing intuitive physical interpretations of observations, the PE method applies to situations in which diffraction is important, where ray tracing might be inaccurate or inapplicable. A disadvantage of the PE simulation is that it does not easily associate features of the sound-speed field with features of the acoustic arrivals, as ray tracing does.

A. PE Modeling Results

The purpose of the PE simulation is to verify if the overall acoustic arrivals identified by ray tracing [Fig. 3(b)] can be reproduced both in their arrival structure and in their relative intensity. The ocean environmental input to the PE simulations is a range-independent model using the CTD profile [Fig. 3(a)] sound speed. The ocean surface is assumed flat and a flat fluid half-space bottom was assumed where the geoacoustic parameters are as follows: sound speed 1620 m/s, density 1850 kg/m^3, and absorption 0.5 dB/λ [10].

Broadband pulses were generated by Fourier synthesizing monochromatic PE runs. In the simulation, the starting frequency is 1.5 kHz, the ending frequency is 10.5 kHz, and the frequency increment is 2.5 Hz. These parameters result in a 400-ms time window, long enough to encompass all desired arrivals without wrap around. In Fig. 8, the envelope of the synthesized pulse is shown as the white line and compared with acoustic data recorded around the time the CTD profile was taken. The simulated waveform matches the acoustic data in terms of number of arrivals, arrival times, and relative strengths, including the very weak early arrival near −15 ms. The PE simulation confirms that the acoustic arrivals are well modeled when *in situ* oceanographic and geophysical input is used. To capture and interpret the variation of the acoustic arrivals when NLIWs are present, we rely on ray tracing simulations.

The broadband PE method shows good agreement with the acoustic data at the time the CTD profile was taken. Presumably, it would work well at other times to the extent that the sound-speed field was properly modeled, including the fluctuations in the arrival times. However, there is no easy way from the PE to say why those fluctuations occurred and why they occurred at the times they did, with the temporal extent and amount of travel time shift they have. Therefore, ray tracing, although not as reliable, will be used to model the propagation when NLIWs are present. The environmental model presented in Section III will be used to provide the range- and time-dependent environmental input.

B. Ray Tracing Results

When NLIWs are within the acoustic path, some of the arrivals show large oscillatory variations, whereas the rest do not. Ray tracing is used to model the arrival time changes using the environmental model presented in Section III as the range- and time-dependent environmental input.

The algorithm used to trace the rays is to integrate the differential equations of the rays with range as the independent variable, and with depth, vertical wave number divided by

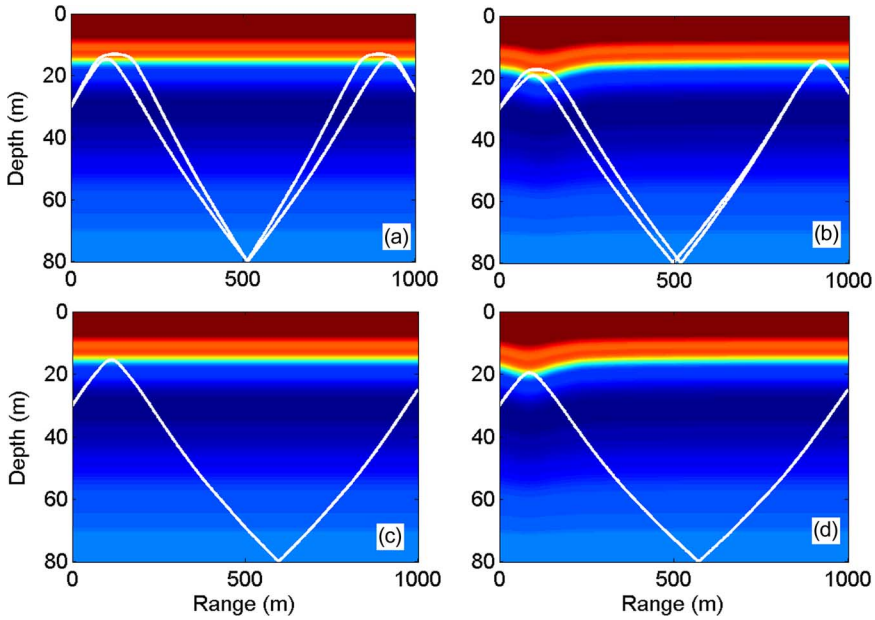

Fig. 10. Comparison of ray paths with and without internal waves: (a) and (b) without and with waves for ray TBT at time 16:48:00Z; (c) and (d) without and with waves for ray TB at time 16:47:00Z.

frequency, and travel time as the dependent variables. The MATLAB routine *ode113* [11] performed the integration.

The sound-speed field (Fig. 7) derived from the CTD chain data and interpolated onto the acoustic path is used as the range-dependent sound-speed field for ray tracing. The time dependence of the sound-speed field is achieved by moving the entire sound-speed field with the wave speed 0.6447 m/s, given in Section III. Range-dependent ray tracing calculations were carried out to simulate acoustic data between 16:24:00Z and 17:26:00Z. The arrival times for rays BT, TB, TBT, and SBS are simulated. At 16:44:00Z, the source is approximately under the peak of the first wave.

The ray tracing results for the four rays are overlaid on acoustic data in Fig. 9. An overall constant travel time of the unmodeled axial arrival used to define the reduced travel time was the only adjustable parameter. It is apparent that the ray tracing results not only successfully captured the times, extents, and magnitudes of the arrival time oscillations (1 ms) but also the gradual arrival time change of rays TBT and SBS due to the depression of the thermocline. Two TBT rays existed most of the time, and the data also often show two separated arrivals.

By closely examining the ray fields for some specific cases, the knowledge of how the rays were affected by the two passing waves was established and a physical interpretation is provided in the following section, including why some of the arrivals show large oscillations, but others do not.

V. Interpretation

Both data and modeling show that for the TB, BT, and TBT arrivals, fluctuations by shortening the travel time by 1 ms are present, but the SBS arrival is much less affected. The rays that have larger travel time fluctuations are those that turn (T) in the strong thermocline. The TBT rays have four fluctuations to shorter time, while the TB and BT rays each have two such fluctuations. All these fluctuations of rays with upper turning points have the shorter travel times when the position of the NLIWs coincide with the upper turning points. Rays that pass through the thermocline without turning, such as the SBS rays, have smaller fluctuations. We would like to be able to explain the lowering of the travel time by the following argument: The sound speed in the wave is greater than it is at the same depth when the wave is absent. Thus, the travel time along any path that passes through the wave is shorter than the travel time along the same path without the wave. We choose this path $p0$ to be the ray in the absence of the wave. By Fermat's principle, with the wave present, the actual ray $p1$ has a shorter travel time than the path $p0$. The ray $p1$ with the wave has shorter travel time than the path $p0$ with the wave, which in turn has a shorter travel time than the ray $p0$ without the wave. Therefore, the ray travel time with the wave is shorter than that without the wave. The trouble with this argument is that Fermat's principle only requires the ray to be a (local) minimum before it reaches a caustic. Beyond the caustic, it is only a saddle point [12]; there are distortions of the ray that give shorter travel times. Each of the rays TBT, TB, and BT has at least one caustic. Thus, the argument must be modified.

The following modified argument also uses Fermat's principle, but allows the ray travel time to be a saddle point, rather than only a minimum. When the sound-speed field changes slightly, the travel time difference between the physical rays in the original and changed environments can be evaluated in two steps. In the previous argument, we first changed the sound speed along the original ray path, and then changed the path from the original ray to the ray for the changed sound-speed field. We also consider the two steps taken in the opposite order. For small changes of the sound-speed field, the travel time change along a fixed path is linear in the size of the perturbation. Therefore, that step always reduces the travel time. The vertical deviation $\delta z(x)$ of a ray due to a small change in the sound speed is linear in the magnitude of that change, because the bending of the ray is proportional to the gradient of the sound speed. For either a minimum or a saddle point, the

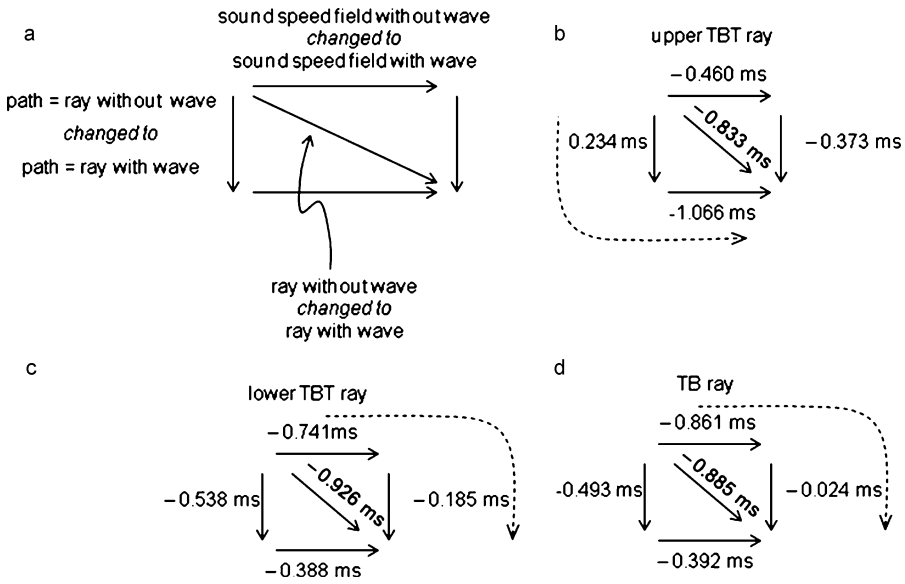

Fig. 11. Computed travel time differences between rays when the wave is absent and when the wave is present, for three ray species. Block "a" shows how to read the entries in blocks "b," "c," and "d." Each travel time difference, shown on the diagonal, is decomposed into the sum of that due to changing the sound-speed field without changing the path, represented by a horizontal arrow, and that due to changing the path without changing the sound-speed field, represented by a downward arrow. Either of the two partial changes can be done first, leading to a horizontal arrow at the top of the block added to a downward arrow on the right, or a downward arrow on the left added to a horizontal arrow on the bottom. Blocks "b," "c," and "d" are labeled by the three ray species. Only one of the two ordering of the partial changes, which is indicated by a dashed arrow, has the quadratic path distortion effect much smaller than the linear sound-speed change effect, but the other ordering has approximately equal partial changes.

travel time in a given sound-speed field is a stationary point in $\delta z(x)$, hence quadratic in the deviation of the path from a ray. In particular, the difference in travel times between the rays for two sound-speed fields differing by a small perturbation, when both times are calculated with either one of the sound-speed fields, is quadratic in the sound-speed difference. For small enough sound-speed field perturbations, the linear effect of the sound-speed difference along either curve is greater than the quadratic effect due to the two paths being different. Since the linear effect reduces the travel time, the total effect reduces the travel time.

It only remains to be seen whether the path distortion effect is indeed small enough between the absence and presence of the wave, allowing one to interpret the shortened travel time as primarily due to the increased sound speed in the wave. We choose three cases to examine. There are actually two TBT rays. Two of our cases are the fluctuations of these two rays at time 16:48:00Z. The third case is the fluctuation of the TB ray at 16:47:00Z. These times are those of the minimum travel time in the first fluctuation, when the first (or only) turning point coincides with the first NLIW. The rays with and without turning in an NLIW are shown in Fig. 10.

The computed travel time differences for these three rays are given in Fig. 11. Each corner of each block "b," "c," and "d" represents the time for a particular path in a particular sound-speed field. The upper corners are for the path that is the ray when the wave is absent, and the lower corners for the path that is the ray with the wave. The left corners are for the sound-speed field without the wave, and the right for the sound-speed field with the wave. Thus, the upper left and lower right corners are the physical cases where the paths are the rays. The arrows with numbers indicate the time difference between the corner at the head of the arrow and that at the tail. The travel times for all the paths decrease (horizontal arrows) with the wave present, as they must, because the sound speed everywhere is larger or equal to that without the wave.

Let us first examine the upper TBT ray in some detail. The two possible ways of taking the two steps to change from the ray without the wave to that with the wave are shown in block "b" of Fig. 11. Starting from the top left corner and moving vertically from downward, we distort the path. This causes the travel time to lengthen by 0.234 ms. Now moving from left to right, the sound-speed field is changed to include the waves, causing the travel time to shorten by 1.066 ms, considerably greater than the amount due to path distortion. Therefore, the modified argument works here; the quadratic change due to path distortion is considerably smaller than that due to the sound-speed field change. However, if we start from the upper left corner, but move horizontally first, the travel time shortens by 0.460 ms due to the change of sound-speed field. Then, moving downward, the travel time shortens further by 0.373 ms due to path distortion. The amount of change in the two steps is of the same order of magnitude. The argument that the quadratic change due to path distortion is much smaller than that due to the sound-speed field change does not work for this order of taking the two steps.

The lower TBT ray and the TB ray are shown in blocks "c" and "d" of Fig. 11. Similar results are obtained for these rays as for the upper TBT ray, except that the modified argument works when the sound-speed change step is taken before the path distortion step. In the order that works for the upper TBT ray, the two steps reduce the travel time in roughly equal amounts.

In each case, for one of the two orders, the change of sound speed can be considered small enough to make the quadratic contribution small compared to the linear contribution. However, for the other order, the contributions are about equal; the quadratic term is never much greater than the linear term. In

summary, the modified argument can be taken in two ways: if the favorable order is taken, the argument works; otherwise, the argument is borderline.

The SBS ray has much smaller travel time fluctuations (0.3 ms) than the rays with upper turning points. There are four passes through the thermocline, and each pass may hit one of the two waves, leading to eight opportunities for a travel time decrease. There are five such fluctuations found in the data; the eight possible decreases overlap in time and the travel time does not return to its no-wave value. This ray passes through the thermocline at an angle of about 12° and, because the angle is large, it encounters the wave for only a short distance, so the travel time change is small.

VI. Discussion

The nonlinear internal waves observed with the towed CTD chain measurements have been interpolated in time and space onto the acoustic path well enough to be able to deterministically model the travel time data fairly well. The interpolation is not entirely straightforward, as the two sides of the acoustic path were rather different. Assumptions had to be made, such as to what to do about the absence of the back of the second wave on the southwest leg going seaward, and with the first northeast leg, going shoreward, not starting far enough southeast to contain the back of the second wave. No attempt was made to interpolate smaller waves, which primarily influence the intensity rather than the travel time.

The NLIWs have a significant effect on the travel time, even though the waves during this experiment were rather small in amplitude. Based on experience from the nearby SWARM [2] experiment, several times larger waves were expected. If they had been bigger, more pronounced effects would have occurred. If the thermocline was depressed enough so that it went below the depth that had been the sound axis, even the direct path would have been strongly affected. (This path is a bunch of rays, rather than one, at a 1-km range with the sound-speed profile that occurred.)

Travel times decreased most notably when the upper turning point of a ray was in (or near) the thermocline and an NLIW encountered this upper turning point. Every time this encounter occurred, the travel time decreased by about 1 ms. The presence of caustics invalidates a straightforward Fermat's principle interpretation with a minimum travel time for the ray. Our attempt to interpret this systematic behavior based on Fermat's principle of stationary, rather than minimum travel time, where ray path change effects are assumed small was only partly successful. A two-step process was used to move from the ray without the wave to that with the wave. The effect of ray path change depended on the order of the two steps. Only one order, and not always the same one, resulted in a small travel time difference due to the distortion of the ray path by the NLIW. For the other order, it was comparable to the travel time decrease due to the higher sound speed along the ray path.

The study has only been concerned with the direct problem. The ability to carry out the inverse problem would depend on what is assumed known. With only the acoustic data, it is unlikely that a meaningful inverse could be done. If the acoustics and the CTD profile from 15:30:00Z were available, there would be a much better chance of useful inversion, although the deepening of the thermocline over the hour from the time of the CTD would have to be allowed for in the inversion method.

Acknowledgment

The authors would like to thank Dr. K. Becker and the members of his team who maintained and operated the CTD chain throughout these and other measurements during SW06.

References

[1] D. Tang, J. N. Moum, J. F. Lynch, P. Abbot, R. Chapman, P. H. Dahl, T. F. Duda, G. Gawarkiewicz, S. Glenn, J. A. Goff, H. Graber, J. Kemp, A. Maffei, J. D. Nash, and A. Newhall, "Shallow Water '06: A joint acoustic propagation/nonlinear internal wave physics experiment," *Oceanography*, vol. 20, no. 4, pp. 156–167, 2007.

[2] J. R. Apel, M. Badiey, C.-S. Chiu, S. Finette, R. Headrick, J. Kemp, J. F. Lynch, A. Newhall, M. H. Orr, B. H. Pasewark, D. Tielbuerger, A. Turgut, K. von der Heydt, and S. Wolf, "An overview of the 1995 SWARM shallow-water internal wave acoustic scattering experiment," *IEEE J. Ocean. Eng.*, vol. 22, no. 3, pp. 465–500, Jul. 1997.

[3] G. Gawarkiewicz, K. H. Brink, F. Bahr, R. C. Beardsley, M. Caruso, J. F. Lynch, and C.-S. Chiu, "A large-amplitude meander of the shelfbreak front during summer south of New England: Observations from the shelfbreak PRIMER experiment," *J. Geophys. Res.*, vol. 109, 2004, 10.1029/2002JC001468, C03006.

[4] T. F. Duda, J. F. Lynch, A. E. Newhall, L. X. Wu, and C.-S. Chiu, "Fluctuation of 400-Hz sound intensity in the 2001 ASIAEX South China Sea experiment," *IEEE J. Ocean. Eng.*, vol. 29, no. 4, pp. 1264–1279, Oct. 2004.

[5] M. Badiey, B. G. Katsnelson, J. F. Lynch, and S. Pereselkov, "Frequency dependence and intensity fluctuations due to shallow water internal waves," *J. Acoust. Soc. Amer.*, vol. 122, pp. 747–760, 2007.

[6] F. S. Henyey and A. Hoering, "Energetics of borelike internal waves," *J. Geophys. Res.*, vol. 102, no. C2, pp. 3323–3330, 1997.

[7] F. N. Fritsch and R. E. Carlson R, "Monotone piecewise cubic interpolation," *SIAM J. Numer. Anal.*, vol. 17, pp. 238–246, 1980.

[8] J. Sherman and R. Pinkel, "Estimates of the vertical wavenumber-frequency spectra of vertical shear and strain," *J. Phys. Oceanogr.*, vol. 21, pp. 292–303, 1991.

[9] M. D. Collins, "Applications and time-domain solution of higher-order parabolic equations in underwater acoustics," *J. Acoust. Soc. Amer.*, vol. 86, pp. 1097–1102, 1989.

[10] J. Yang, D. Tang, and K. L. Williams, "Direct measurement of sediment sound speed using SAMS in SW06," *J. Acoust. Soc. Amer.*, vol. 124, 2008, EL116.

[11] L. F. Shampine and M. K. Gordon, *Computer Solution of Ordinary Differential Equations: The Initial Value Problem*. San Francisco, CA: W. H. Freeman, 1975.

[12] M. Born and E. Wolf, *Principles of Optics*, 7th ed. Cambridge, U.K.: Cambridge Univ. Press, 1999, pp. 136–139.

[13] K. Lamb, *Private Comunication.* 1998.

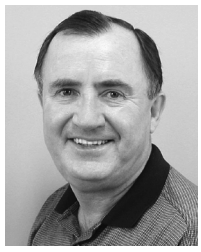

Frank S. Henyey received the Ph.D. degree in theoretical physics from the California Institute of Technology, Pasadena, in 1967.

He held postdoctoral and faculty positions at the University of Michigan and research positions at the LaJolla Institute (where he was Associate Director of the Center for Studies of Nonlinear Dynamics) and Areté Associates. Since 1991, he has been at the University of Washington, Seattle, as a Principal Physicist in the Ocean Physics Department of the Applied Physics Laboratory. He is a seagoing theoretical physicist with interests in ocean acoustics and small-scale ocean hydrodynamics.

Dr. Henyey is a Fellow of the Acoustical Society of America and a member of the American Physical Society and the American Geophysical Union.

Kevin L. Williams received the B.S., M.S., and Ph.D. degrees in physics from Washington State University, Pullman, in 1979, 1983, and 1985, respectively.

He worked at the Naval Coastal Systems Center, Panama City, FL, from 1985 to 1988, where his primary focus was in acoustic scattering from finite bodies and propagation into ocean sediments. In 1988, he moved to the Applied Physics Laboratory, University of Washington, Seattle, where he has worked in the area of high-frequency environmental acoustics, studying propagation through ocean internal waves and arctic ice and propagation and scattering in ocean sediments. He is currently a Principal Physicist at the Applied Physics Laboratory. He is also an Associate Professor in the Oceanography Department, University of Washington.

Dr. Williams is a Fellow of the Acoustical Society of America.

Jie Yang received the B.S. degree in physics from the Ocean University of Qingdao, Qingdao, China, in 1999 and the Ph.D. degree in mechanical engineering from the Georgia Institute of Technology, Atlanta, in 2007.

Since 2007, she was a Postdoctoral Fellow supported by the U.S. Office of Naval Research and then a Physicist with the Applied Physics Laboratory, University of Washington, Seattle. Her research interests are ocean acoustics and acoustical oceanography.

Dr. Yang is a member of the Acoustical Society of America.

Dajun Tang received the B.S. degree from the University of Science and Technology, Hefei, China, in 1981, the M.S. degree from the Institute of Acoustics, Beijing, China, in 1985, and the Ph.D. degree in oceanographic engineering from the Joint Program of Massachusetts Institute of Technology and the Woods Hole Oceanographic Institution, Cambridge/Woods Hole, in 1991.

From 1991 to 1996, he was first an Assistant Scientist and then an Associate Scientist at Woods Hole Oceanographic Institution. In 1996, he moved to the Applied Physics Laboratory, University of Washington, Seattle, where he is currently a Senior Oceanographer. His research encompasses acoustics in shallow water, emphasizing impacts on acoustics by the sea bottom and water column variability.

Dr. Tang was Co-Chief Scientist for the Shallow Water 2006 (SW06) experiment.

Modeling interface roughness scattering in a layered seabed for normal-incident chirp sonar signals

Dajun Tang[a] **and Brian T. Hefner**
Applied Physics Laboratory, University of Washington, 1013 NE 40th Street, Seattle, Washington 98105
djtang@apl.washington.edu, hefner@apl.washington.edu

Abstract: Downward looking sonar, such as the chirp sonar, is widely used as a sediment survey tool in shallow water environments. Inversion of geo-acoustic parameters from such sonar data precedes the availability of forward models. An exact numerical model is developed to initiate the simulation of the acoustic field produced by such a sonar in the presence of multiple rough interfaces. The sediment layers are assumed to be fluid layers with non-intercepting rough interfaces.

© 2012 Acoustical Society of America
PACS numbers: 43.30.Hw, 43.30.Gv, 43.30.Ma [JL]
Date Received: December 5, 2011 **Date Accepted:** February 7, 2012

I. Introduction

Chirp sonar is widely used as a survey tool to image shallow water sediment structure. Usually, it has a beam pattern aimed vertically toward the seafloor and operates at a nominal center frequency of several kilohertz with a wide frequency band on the order of 10 kHz, providing a depth resolution on the order of 10 cm. Chirp sonar data inversion has been used to determine sediment layering and physical properties in underwater acoustics applications.[1–4] A curious fact is that an exact forward model predicting the received sound field by such a sonar for a given physical sediment structure has not been developed. The availability of such predictive models would help the interpretation of chirp sonar data and validation of geo-acoustic inversion results based on such data. This paper is an initial step toward such a forward model and strives for an exact solution of interface roughness scattering using the integral equation method. It is not meant for direct application to real sonar systems, but to provide a basis on which practical models, such as the recent model based on a transfer function approach,[5] can be validated.

The sediment is modeled in the two-dimensional space and consists of a set of fluid layers separated by one-dimensional rough interfaces. Each layer is assumed to be homogeneous with constant sound speed, density, and attenuation coefficient. The rough interfaces are assumed to be single-valued and never to cross one another, but otherwise allowed to be arbitrary. This initial model does not allow for sediment volume heterogeneity. In addition to sediment acoustics, this model has potential application in imaging Arctic ice from underneath the ice layer. When the roughness is small compared to the acoustic wavelength, perturbation method can be used to treat multiple rough layers.[6] Here we do not make such an assumption and the rough surface amplitudes are allowed to be large as compared to the acoustics wavelength.

2. Single rough interface problem

Let the one-dimensional rough interface $\zeta(x)$ separate two fluid half-spaces. The coordinate system is defined such that the positive z-axis points upward and the x-axis to the right. A monochromatic incident wave $p_{\text{inc}}(\mathbf{r})$ with frequency f impinges from above the interface, where $\mathbf{r} = (x,z)$. The upper medium has sound speed c_1, density ρ_1,

[a]Author to whom correspondence should be addressed.

 © 2012 Acoustical Society of America

Downloaded 15 Jun 2012 to 128.95.76.55. Redistribution subject to ASA license or copyright; see http://asadl.org/journals/doc/ASALIB-home/info/terms.jsp

and attenuation factor δ_1, which is the ratio of the imaginary part to the real part of the wavenumber $k_1 = (2\pi f/c_1)(1 + i\delta_1)$, and the lower medium has corresponding sound speed c_2, density ρ_2, and attenuation factor δ_2, as well as wavenumber k_2. Following Thorsos,[7,8] the coupled integral equations with two unknown quantities $p_1(\mathbf{r})$ and $\frac{\partial p_1(\mathbf{r})}{\partial n}$ on the rough interface are

$$\begin{cases} p_1(\mathbf{r}) = 2p_{\text{inc}}(\mathbf{r}) - \dfrac{\mathrm{i}}{2}\displaystyle\int \left[H_0^1(k_1|\mathbf{r}-\mathbf{r}'|)\dfrac{\partial p_1(\mathbf{r}')}{\partial n'} - \dfrac{\partial H_0^1(k_1|\mathbf{r}-\mathbf{r}'|)}{\partial n'} p_1(\mathbf{r}') \right] ds' \\ p_1(\mathbf{r}) = \dfrac{i}{2}\displaystyle\int \left[H_0^1(k_2|\mathbf{r}-\mathbf{r}'|)\dfrac{\rho_2}{\rho_1}\dfrac{\partial p_1(\mathbf{r}')}{\partial n'} - \dfrac{\partial H_0^1(k_2|\mathbf{r}-\mathbf{r}'|)}{\partial n'} p_1(\mathbf{r}') \right] ds', \end{cases} \tag{1}$$

where $\partial/\partial n'$ is the surface normal derivative, and H_0^1 is the Hankel function of the first kind. The integrals are along the rough interface and all quantities in Eq. (1) are evaluated on the interface. The unknowns in Eq. (1) are chosen to be the field and its normal derivative in the upper medium. Corresponding quantities in the lower medium are found through the boundary conditions

$$\begin{cases} p_1(\mathbf{r}) = p_2(\mathbf{r}) \\ \dfrac{1}{\rho_1}\dfrac{\partial p_1(\mathbf{r})}{\partial n} = \dfrac{1}{\rho_2}\dfrac{\partial p_2(\mathbf{r})}{\partial n}. \end{cases} \tag{2}$$

When $p_1(\mathbf{r})$ and $\frac{\partial p_1(\mathbf{r})}{\partial n'}$ are solved, the scattered field anywhere in media 1 and 2 are given by

$$\begin{cases} p_{1s}(\mathbf{r}) = p_1(\mathbf{r}) - p_{\text{inc}}(\mathbf{r}) = \dfrac{i}{4}\displaystyle\int \left[H_0^{(1)}(k_1|\mathbf{r}-\mathbf{r}'|)\dfrac{\partial p_1(\mathbf{r}')}{\partial n'} - \dfrac{\partial H_0^{(1)}(k_1|\mathbf{r}-\mathbf{r}'|)}{\partial n'} p_1(\mathbf{r}') \right] ds' \\ p_2(\mathbf{r}) = \dfrac{i}{4}\displaystyle\int \left[H_0^{(1)}(k_2|\mathbf{r}-\mathbf{r}'|)\dfrac{\rho_2}{\rho_1}\dfrac{\partial p_1(\mathbf{r}')}{\partial n'} - \dfrac{\partial H_0^{(1)}(k_2|\mathbf{r}-\mathbf{r}'|)}{\partial n'} p_1(\mathbf{r}') \right] ds'. \end{cases} \tag{3}$$

By discretizing the interface into N equal segments $\Delta x = L/N$, where L is the total length of the ensonified interface, the integral Eq. (1) is recast into the matrix form

$$\mathbf{q} = \mathbf{A}\mathbf{y}, \tag{4}$$

where $\mathbf{q}$ is a known column vector of length $2N$. The jth element of $\mathbf{q}$ is

$$q_j = \begin{cases} p_{\text{inc}}(\mathbf{r}_j), & j = 1, 2, \ldots, N \\ 0, & j = (N+1), (N+2), \ldots, 2N, \end{cases} \tag{5}$$

and $\mathbf{y}$ is an unknown column vector of length $2N$. The mth element of $\mathbf{y}$ is

$$y_m = \begin{cases} \dfrac{\Delta x \gamma_m}{4i}\dfrac{\partial p_1(\mathbf{r}_m')}{\partial n'}, & m = 1, 2, \ldots, N \\ \dfrac{\Delta x \gamma_m}{4i} p_1(\mathbf{r}_m'), & m = (N+1), (N+2), \ldots, 2N, \end{cases} \tag{6}$$

where $\gamma_m = \sqrt{1 + \left(\frac{d\zeta(x_m)}{dx}\right)^2}$. In Eq. (4), $\mathbf{A}$ is a $2N \times 2N$ matrix, which can be more conveniently expressed as four $N \times N$ sub-matrices: $\mathbf{A} = \begin{pmatrix} \mathbf{A}^{11} & \mathbf{A}^{12} \\ \mathbf{A}^{21} & \mathbf{A}^{22} \end{pmatrix}$, where the element at the jth row and mth column of each of the sub-matrices is, respectively,

Downloaded 15 Jun 2012 to 128.95.76.55. Redistribution subject to ASA license or copyright; see http://asadl.org/journals/doc/ASALIB-home/info/terms.jsp

$$A_{jm}^{11} = \begin{cases} -H_0^{(1)}\left(k_1\left|\mathbf{r}_j - \mathbf{r}_m{}'\right|\right), & j = 1,2,\ldots,N; \quad m = 1,2,\ldots,N; \quad (j \neq m) \\ -H_0^{(1)}\left(k_1 \Delta x \gamma_j/(2e)\right), & j = 1,2,\ldots,N; \quad (j = m), \end{cases}$$

$$A_{jm}^{21} = \begin{cases} \dfrac{\rho_2}{\rho_1} H_0^{(1)}\left(k_2\left|\mathbf{r}_j - \mathbf{r}_m{}'\right|\right) & j = 1,2,\ldots,N; \quad m = 1,2,\ldots,N; \quad (j \neq m) \\ \dfrac{\rho_2}{\rho_1} H_0^{(1)}\left(k_2 \Delta x \gamma_j/(2e)\right), & j = 1,2,\ldots,N; \quad (j = m), \end{cases}$$

$$A_{jm}^{12} = \begin{cases} \dfrac{\partial H_0^{(1)}\left(k_1\left|\mathbf{r}_j - \mathbf{r}_m{}'\right|\right)}{\partial n'}, & j = 1,2,\ldots,N; \quad m = 1,2,\ldots,N; \quad (j \neq m) \\ i\left(\dfrac{2\zeta''}{\gamma_j \Delta x} - \dfrac{(jx)\Delta}{\pi \gamma_j^3}\right), & j = 1,2,\ldots,N; \quad (j = m), \end{cases} \tag{7}$$

$$A_{jm}^{22} = \begin{cases} -\dfrac{\partial H_0^{(1)}\left(k_2\left|\mathbf{r}_\mathrm{j} - \mathbf{r}_{\mathrm{m},}{}'\right|\right)}{\partial n'}, & j = 1,2,\ldots,N; \quad m = 1,2,\ldots,N; \quad (j \neq m) \\ i\left(\dfrac{2\zeta''}{\gamma_j \Delta x} + \dfrac{(jx)\Delta}{\pi \gamma_j^3}\right), & j = 1,2,\ldots,N; \quad (j = m). \end{cases}$$

The matrix Eq. (4) can be solved

$$\mathbf{y} = \mathbf{S}\mathbf{q}, \tag{8}$$

where $\mathbf{S} = \mathbf{A}^{-1}$. The matrix $\mathbf{A}$, hence $\mathbf{S}$, is a function of the rough interface and media properties above and below the interface, and is independent of the incident wave $p_{\mathrm{inc}}(\mathbf{r})$, or $\mathbf{q}$. This property will be exploited in problems of scattering from multiple rough interfaces. Another useful property of the matrix $\mathbf{A}$ is how the matrix Eq. (4) would change when the incident wave impinges from below the interface. In Eq. (1), interchange the subscripts 1 and 2, and still express $p_1(\mathbf{r}')$ and $\frac{\partial p_1(\mathbf{r}')}{\partial n'}$ as the unknowns using boundary conditions (2), one finds that the matrix equation for an incident wave coming from the lower medium has the same matrix form as Eq. (4)

$$\underline{\mathbf{q}} = \mathbf{A}\mathbf{y}, \tag{9}$$

where the elements of $\underline{\mathbf{q}}$ are similar to $\mathbf{q}$, but its second half is the incident wave

$$\underline{q}_j = \begin{cases} 0, & j = 1,2,\ldots,N \\ p_{\mathrm{inc}}\left(\mathbf{r}_j\right), & j = (N+1),(N+2),\ldots,2N. \end{cases} \tag{10}$$

This symmetry property means that the scattering matrix $\mathbf{S}$ uniquely governs sound scattering from a particular rough interface for incident waves coming either from above or below. Once $\mathbf{S}$ is obtained, scattering from the interface for a given frequency for any normal incident wave is uniquely determined.

Once $\mathbf{y}$ is known, the scattered field anywhere in space can be calculated using Eq. (3), or its equivalent matrix form. For M observation points in the upper medium, the scattered field is

$$\mathbf{q}_1 = \mathbf{T}_u \mathbf{y}, \tag{11}$$

Downloaded 15 Jun 2012 to 128.95.76.55. Redistribution subject to ASA license or copyright; see http://asadl.org/journals/doc/ASALIB-home/info/terms.jsp

where $\mathbf{q}_1$ is a vector of length $2M$, whose first M elements are zero, and the second M elements are the scattered field $p_{1s}(\mathbf{r}_m)$ evaluated at the M points $\mathbf{r}_m$, $m=1,2,\ldots,M$ in medium 1. The upward propagation matrix $\mathbf{T}_u$ is a $2M\times 2N$ matrix whose first M rows are zero, and the rest are

$$T_{umj}=\begin{cases} H_0^{(1)}\left(k_1\left|\mathbf{r}_m-\mathbf{r}_j'\right|\right), m=(M+1),(M+2),\ldots,2M, j=1,2,\ldots,N \\ -\dfrac{\partial H_0^{(1)}\left(k_1\left|\mathbf{r}_m-\mathbf{r}_j'\right|\right)}{\partial n'}, m=(M+1),(M+2),\ldots,2M, j=(N+1),(N+2),\ldots,2N. \end{cases} \tag{12}$$

Similarly, for any M observation points in the lower medium, the scattered field is

$$\mathbf{q}_2=\mathbf{T}_d\mathbf{y}, \tag{13}$$

where $\mathbf{q}_2$ is a vector of length $2M$, whose second M elements are zeros, and whose first M elements are the scattered field $p_2(\mathbf{r}_m)$ evaluated at the M points $\mathbf{r}_m$, $m=1,2,\ldots,M$ in medium 2. The downward propagation matrix $\mathbf{T}_d$ is also a $2M\times 2N$ matrix, though its second M rows are zero, and the first M rows are

$$T_{dmj}=\begin{cases} -\dfrac{\rho_2}{\rho_1}H_0^{(1)}\left(k_2\left|\mathbf{r}_m-\mathbf{r}_j'\right|\right), & m=1,2,\ldots,M, \quad j=1,2,\ldots,N \\ \dfrac{\partial H_0^{(1)}\left(k_2\left|\mathbf{r}_m-\mathbf{r}_j'\right|\right)}{\partial n'}, & m=1,2,\ldots,M, \quad j=(N+1),(N+2),\ldots,2N. \end{cases} \tag{14}$$

3. Multiple rough interfaces problem

For a single rough interface we have shown that each rough interface $\zeta(x)$ has an associated scattering matrix $\mathbf{S}$ that is a function of the parameters of the media above and below the interface, and uniquely determines the scattered field for any incident field. Two propagation matrices, $\mathbf{T}_u$ and $\mathbf{T}_d$, allow calculation of the scattered field above or below the rough interface once the field and its normal derivative on the interface are calculated. When there are two or more rough interfaces, the previous results are used to construct the scattered field.

In a scenario of two rough interfaces, let $\zeta_1(x)$ be a rough interface situated above another rough interface $\zeta_2(x)$. Also assume that the two interfaces never intersect with each other, or $\zeta_1(x)>\zeta_2(x)$. While the parameters above and below $\zeta_1(x)$ are the same as those for a single rough interface, the medium beneath $\zeta_2(x)$ has sound speed c_3, density ρ_3, attenuation factor δ_3, as well as wavenumber k_3. Each rough interface has an associated scattering matrix and a pair of propagation matrices, and are given the names $\mathbf{S}_j$, and $\mathbf{T}_{ju}$ and $\mathbf{T}_{jd}$, $j=1,2$. The discretized unknown field and its normal derivative for each rough interface are always chosen to be the ones above the corresponding interface. They are designated as $\mathbf{y}_1$ and $\mathbf{y}_2$ and are expressed in the same manner as those given in Eq. (6) for each interface. For interface $\zeta_1(x)$, there are two waves impinging onto it: one is the original incident wave $\mathbf{q}$ coming from above, the other is $\mathbf{T}_{2u}\mathbf{y}_2$ that is scattered upward by $\zeta_2(x)$ from below. Whereas for $\zeta_2(x)$, there is only one incident wave, $\mathbf{T}_{1d}\mathbf{y}_1$, forward scattered by $\zeta_1(x)$. Using Eqs. (8) and (9) and linear superposition yields

$$\begin{cases} \mathbf{y}_1=\mathbf{S}_1\mathbf{q}+\mathbf{S}_1\mathbf{T}_{2u}\mathbf{y}_2 \\ \mathbf{y}_2=\mathbf{S}_1\mathbf{T}_{1d}\mathbf{y}_1. \end{cases} \tag{15}$$

Solving the equations for the unknown on the first interface yields $\mathbf{y}_1=\mathbf{S}_1\mathbf{q}+(\mathbf{S}_1\mathbf{T}_{2u}\mathbf{S}_2\mathbf{T}_{1d})\mathbf{y}_1$, or

Downloaded 15 Jun 2012 to 128.95.76.55. Redistribution subject to ASA license or copyright; see http://asadl.org/journals/doc/ASALIB-home/info/terms.jsp

$$\mathbf{y}_1 = \frac{1}{1-\mathbf{R}_{1,2}}\mathbf{S}_1\mathbf{q}, \tag{16}$$

where $\mathbf{R}_{1,2} = \mathbf{S}_1\mathbf{T}_{2u}\mathbf{S}_2\mathbf{T}_{1d}$ is the multiple scattering matrix for the two-layer system. The result in Eq. (16) has a "ray" interpretation and it can be more explicitly seen if the matrix in the denominator is expressed using the binomial expansion

$$\mathbf{y}_1 = \frac{1}{1-\mathbf{R}_{1,2}}\mathbf{S}_1\mathbf{q} = \sum_{n=0}^{\infty}\mathbf{R}_{1,2}^n\mathbf{S}_1\mathbf{q}, \tag{17}$$

where the $n=0$ term is for the case where the second interface is absent, and the $n=1$ term is used where the second interface scatters once. In general, the nth term is for the case where the wave has been reflected between the two interfaces n times.

For N rough interfaces, a procedure similar to Eq. (15) can be used to construct the multiple scattered field. In particular, if one is interested in finding the field scattered back to medium 1, as would be used for chirp sonar, a general multiple scattering matrix $\mathbf{R}_{1,N}$ can be derived to be

$$\mathbf{y}_1 = \frac{1}{1-\mathbf{R}_{1,N}}\mathbf{S}_1\mathbf{q}, \tag{18}$$

where the multiple scattering matrix is given recursively

$$\mathbf{R}_{1,N} = \frac{\mathbf{R}_{1,N-1}}{1-\mathbf{R}_{N-1,N}}. \tag{19}$$

For example, when there are three rough interfaces

$$\mathbf{R}_{1,3} = \frac{\mathbf{R}_{1,2}}{1-\mathbf{R}_{2,3}} = \frac{\mathbf{S}_1\mathbf{T}_{2u}\mathbf{S}_2\mathbf{T}_{1d}}{1-\mathbf{S}_2\mathbf{T}_{3u}\mathbf{S}_3\mathbf{T}_{2d}}. \tag{20}$$

4. Numerical example

To demonstrate the application for two rough interfaces, consider a sound source and receiver co-located 20 m above the mean seafloor. The point source emits 1 μPa at 1 m range and has a Gaussian beam pattern such that the incident sound amplitude on the mean seafloor drops to $1/e$ at 5.6 m from the center of the beam. The source has a center frequency of 3500 Hz, and a Gaussian spectrum such that the baseband has half power at 1000 Hz. The sediment is a layer of sand with a mean thickness of 3 m, which is in turn on top of a mud half space. The parameters for the three layers are given in Table 1. Both interfaces have the same power spectrum as provided by the ONR Reverberation Modeling Workshop:[9,10] $P = \frac{h^2 K_L}{\pi\left(K_L^2+K_x^2\right)}$, with $h = 0.316$ m, $K_L = 2.510^{-3}$ m^{-1} for the water–sand interface specified as "typical," and $h = 0.1$ m, $K_L = 1$ m^{-1} for the sand–mud interface specified as "rough." The scattered fields are calculated at a set of 172 frequencies around the center frequency with 37.5-Hz increments; Fourier synthesis is used to obtain time domain fields. In this example (Fig. 1),

Table 1. Medium parameters.

	C (m/s)	ρ (kg/m^3)	δ
Water	1500	1000	0
Sand	1740	2000	0.01
Mud	1485	1400	0.001

Downloaded 15 Jun 2012 to 128.95.76.55. Redistribution subject to ASA license or copyright; see http://asadl.org/journals/doc/ASALIB-home/info/terms.jsp

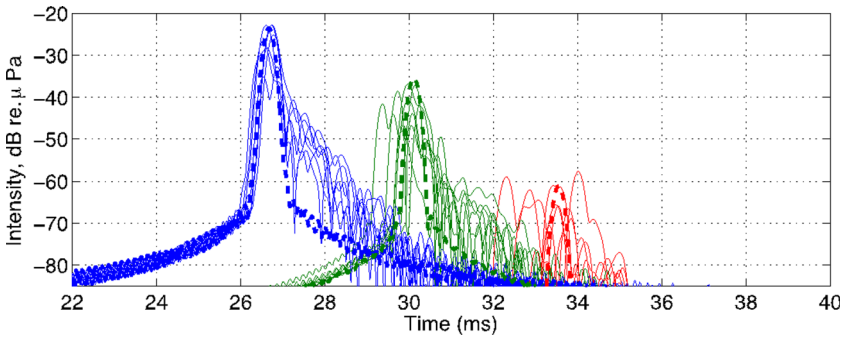

Fig. 1. (Color online) The first three arrivals: the first is from the water–sand interface with roughness described by the "typical" spectrum, the second from the sand–mud interface with roughness described by the "rough" spectrum, and the third also from the sand–mud interface with a round trip between the two interfaces. The dashed curves are for flat interfaces. The thin solid curves are arrivals from seven rough interfaces.

there are three arrivals. The first is the scattered field by the water–sand interface (blue), the second is (a) forward scattered by the water–sand interface onto the sand–-mud interface, (b) backscattered to the water–sand interface, and then (c) forward scattered to the water column (green). The third is similar to the second but with an additional round trip inside the sand layer (red). Results for the flat interfaces are also given (Fig. 1, dashed) which has a 16 dB loss from propagation from the 20 m height. The main effects of the roughness as compared to the flat interface are (1) to cause the main return to fluctuate as a function of position, and (2) to produce a coda, or scattered wave that follows the main arrival. Later arrivals have more fluctuation due to multiple scattering. Figure 2 shows results over a range of 100 m containing 100 pings, from which several observations can be made: (i) the low spatial frequency roughness of the interfaces can be traced by the scattered intensities; (ii) the coda appears as "noise" in between the layers, not unlike those observed in chirp data; and (iii)

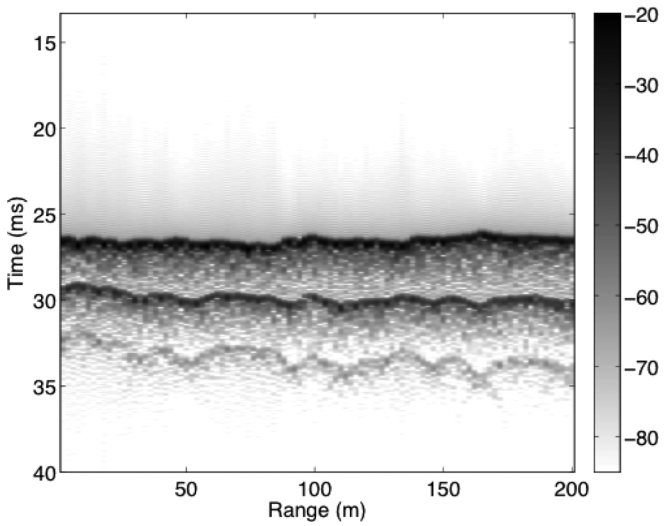

Fig. 2. Simulation for two rough interfaces. There are 100 pings over a 200 m range. The mean distance between the two interfaces is 3 m. The colorbar shows intensity in dB. The faint signals arriving earlier than the water–bottom interface (time earlier than 26 ms) are numerical artifacts due to finite bandwidth in the Fourier synthesis.

Downloaded 15 Jun 2012 to 128.95.76.55. Redistribution subject to ASA license or copyright; see http://asadl.org/journals/doc/ASALIB-home/info/terms.jsp

multiple scattered arrivals are appreciable, though about 20 dB lower than those scattered by the lower interface.

5. Summary

This paper provides a method for calculating exact scattered fields from a system of rough interfaces in two-dimensional space for normal incident sonar. It is intended as a basis of comparison for approximate methods such as the Kirchhoff approximation. It is also a tool for studying statistics of scattered waves and validating techniques for estimating sediment properties using such sonar.

Acknowledgments

The work is supported by the Office of Naval Research, Ocean Acoustics.

References and links

[1]S. G. Schock, "A method for estimating the physical and acoustic properties of the sea bed using chirp sonar data," IEEE J. Ocean. Eng. **26**, 1200–1217 (2001).
[2]S. G. Schock, "Remote estimates of physical and acoustic sediment properties in the South China Sea using chirp sonar data and the Biot model," IEEE J. Ocean. Eng. **29**, 1218–1230 (2004).
[3]A. Turgut, "Performance of one-dimensional chirp sonar inversion in complex environments," J. Acoust. Soc. Am. **107**, 2772 (2000).
[4]M. S. Ballard, K. Becker, and J. A. Goff, "Geoacoustic inversion for the New Jersey Shelf: 3-D sediment model," IEEE J. Ocean. Eng. **35**, 28–42 (1988).
[5]S. Rakotonarivo, M. Legris, R. Desmare, J.-P. Sessarego, and J.-F. Bourillet, "Forward modeling for marine sediment characterization using chirp sonars," Geophysics **76**, T91–T99 (2011).
[6]W. A. Kuperman and H. Schmidt, "Self-consistent perturbation approach to rough surface scattering in stratified elastic media," J. Acoust. Soc. Am. **86**, 1511–1522 (1989).
[7]E. I. Thorsos, "The validity of the Kirchhoff approximation for rough surface scattering using a Gaussian roughness spectrum," J. Acoust. Soc. Am. **83**, 78–92 (1988).
[8]E. I. Thorsos, "Accuracy of scattering approximations for acoustical remote sensing," J. Acoust. Soc. Am. **90**, 2232 (1991).
[9]E. I. Thorsos and J. Perkins, "Reverberation due to bottom roughness using first-order perturbation theory," in *Proceedings of the International Symposium on Underwater Reverberation and Clutter*, edited by P. L. Neilsen, C. H. Harrison, and J.-C. Le Gac, NATO Research Centre, La Spezia, Italy, 9–12 September 2008, pp. 3–14.
[10]J. D. Yang and E. I. Thorsos, "Reverberation due to bottom roughness using first-order perturbation theory," in *Proceedings of the International Symposium on Underwater Reverberation and Clutter*, edited by P. L. Neilsen, C. H. Harrison, and J.-C. Le Gac, NATO Research Centre, La Spezia, Italy, 9–12 September 2008, pp. 81–88.

Downloaded 15 Jun 2012 to 128.95.76.55. Redistribution subject to ASA license or copyright; see http://asadl.org/journals/doc/ASALIB-home/info/terms.jsp

Application of small-roughness perturbation theory to reverberation in range-dependent waveguides

Dajun Tang[a] and Darrell R. Jackson
Applied Physics Laboratory, University of Washington, Seattle, Washington 98105

(Received 27 June 2011; revised 21 February 2012; accepted 28 March 2012)

A rough-interface reverberation model is developed for range-dependent environments. First-order perturbation theory is employed, and the unperturbed background medium can be layered and heterogeneous with arbitrary range dependence. To calculate the reverberation field, two-way forward scatter due to the slowly changing unperturbed environment is handled by fast numerical methods. Backscatter due to small roughness superimposed on any of the slowly varying interfaces is handled efficiently using a Monte Carlo approach. Numerical examples are presented to demonstrate the application of the model. The primary purpose of the model is to incorporate relevant physics while improving computational speed. © *2012 Acoustical Society of America*.
[http://dx.doi.org/10.1121/1.4707437]

PACS number(s): 43.30.Gv, 43.30.Hw [MS] Pages: 4428–4441

I. INTRODUCTION

This paper expands model capabilities for range-dependent shallow water reverberation due to roughness of interfaces, including the sea surface and water-seafloor interface as well as buried interfaces such as the sediment basement. In such problems, scattering is diffusely distributed in space and contributes to background reverberation as compared to distinct returns due to targets and target-like clutter. The practical issue challenging such modeling efforts is fidelity vs speed. When the environment is specified, the reverberation problem can in principle be solved exactly when sufficient computational power is available using numerical methods, such as the finite element method. However, such brute force approaches cannot presently render practically useful solutions. To obtain practical solutions, compromise is needed between computation speed and accuracy. In the foreseeable future, such a compromise will be the primary modus operandi. Then the questions are: First, with given mission-required fidelity versus uncertainty, is there an approximate model that can predict reverberation with sufficient speed? Second, what is the uncertainty in the reverberation prediction? The primary goal of this paper is to address the first question. In particular, this article develops a physics-based model that calculates reverberation in a waveguide with arbitrary range-dependent bathymetry and stratification where the interfaces have randomly distributed roughness. The small-roughness perturbation approximation is used in which the roughness responsible for acoustic backscattering is assumed to be much smaller than the acoustic wavelength. It is important to note that the smallness criterion does not apply to larger-scale bathymetry. On the one hand, the range-dependent propagation is handled by fast numerical methods such as the parabolic equation (PE), hence the computational speed is reasonably fast; on the other hand, because the basis of this approach is physical rather than phenomenological, the results can be used to assess the appropriateness of other faster but possibly less accurate methods.

Except for exact numerical approaches such as the finite element method,[1] which have been made available with increased computer capacity, reverberation models assume the reverberant return is a result of two-way outgoing-and return-propagation with a single backscatter coupling the two. The outgoing-and return-propagation may itself involve a different kind of scattering in the sense that a range-dependent environment alters the waveguide field compared to the range-independent case, but scattering that reverses the direction of propagation is assumed to be negligible. In the following, the term forward scattering is applied to computation of both the outgoing and return field. This multiple forward scatter, single backscatter assumption is reasonable except in cases where the mechanism responsible for backscatter also causes an appreciable change in forward scatter, e.g., a dense bubble cloud.

In many cases, outgoing-and return-propagation is further approximated by range-independent propagation with forward scatter ignored. One of the earliest and most influential models is by Bucker and Morris,[2] who suggested using normal mode intensity to approximate the two-way outgoing-and return-propagation. In their approach, the single bottom backscatter, which is specified by a scattering cross section with Lambert's law as its default form, causes coupling between outgoing and return modes with incident and scattered angles of the cross section related to the mode horizontal wavenumber. They further assumed that cross-mode contributions are unimportant. When the mode group speeds are approximated by the reference water sound speed, the computational speed is fast. This model has been improved in its fidelity in accuracy, with modest cost in speed, to allow the individual normal modes to travel with their own group speeds.[3–6]

Specific scattering mechanisms, such as bottom roughness[7–10] and sediment volume heterogeneity[11] have

[a]Author to whom correspondence should be addressed. Electronic mail: djtang@apl.washington.edu

 0001-4966/2012/131(6)/4428/14/$30.00 © 2012 Acoustical Society of America

Author's complimentary copy

been incorporated into the model discussed in the preceding text, further improving fidelity. In these improvements, the propagation is calculated by normal mode codes such as KRAKEN[12] or wavenumber integration codes such as OASES.[13] In the same category and widely used, ray tracing is sometimes employed to calculate the propagation.[14] This offers competitive speed, but issues encountered in using rays have to be handled carefully.

An especially fast method is based on an energy flux approximation.[3,15–18] The high speed of this approach originates from its closed-form nature when certain assumptions are made regarding the boundary reflection coefficient, water column sound speed, and scattering cross sections. This method may remain the preferred choice for applications when speed is paramount.

In modeling reverberation due to interface roughness, the perturbation method is effective if the roughness deviation from a mean interface is small compared to the acoustic wavelength and if the maximum slope of the interface is sufficiently small.[19,20] The roughness is commonly quantified by a power spectrum, and the rough interface is assumed to be spatially stationary. In reverberation models using the perturbation approximation, the mean interface is typically assumed to be flat; low spatial frequency variations do not exist. In terms of the roughness power spectrum, the assumption is that there is a low-wavenumber scale below which the power spectrum is zero. The interface roughness spectrum is likely to be an approximate power-law over scales from 1 cm to 1 m with no clear-cut division into low-and high-wavenumber parts[21] (Chap. 6). Measurements extending over the scales of interest in low- and medium-frequency reverberation have yet to be made, so the question of separation of large and small scales remains open in these cases.

In this paper, it is assumed that the interface roughness has two separable scales, one low-wavenumber component that may correspond depth changes that are much larger than the acoustic wavelength but that are slowly undulating in space; the other high-wavenumber component corresponds to roughness having vertical scale that is small compared to the acoustic wavelength and horizontal scale comparable to the wavelength. This small-scale roughness is superimposed on the slowly changing low-wavenumber background. One example is small roughness on a sloping bottom. With the two-scale assumption, it is further assumed that the slowly changing component causes forward scatter but no backscatter. The single backscatter is handled using the first-order perturbation approximation against this slowly changing background. With these assumptions, the forward scatter in a gently changing environment can be handled by choosing any efficient, one-way propagation method, such as PE, coupled modes,[22] or the virtual source method,[23] making modeling reverberation in range-dependent environments practical even when mode coupling is significant. However, the validity of the two-scale assumption is not in general justified, and the user should be careful in applying the method to new scenarios.

The formulation to be given here of first-order perturbation theory with a general, non-flat background, is, to the authors' knowledge, a new result. In contrast to most published work, this formulation offers first-order perturbation results on individual surface realizations, rather than the ensemble-averaged intensity.

The structure of the paper is such that the full acoustics problem, including the definition and the main results, is presented in Sec. II, while the details of the derivation are given in Appendix A. Section III gives a range-independent example for a two half-space problem where the numerical result for the scattering cross section is compared to results using known theoretical formulas. Detailed steps of computation, which are common to other sections, are provided. In many applications, the phenomenological Lambert's law is used as the scattering cross section. In Sec. IV, the new formula is applied to a layered environment that has been tailored to mimic Lambert's law over limited angular and frequency ranges. This offers a step toward comparison of results between fast, application driven codes and physics-based methods. Section V is devoted to two reverberation problems in which the reverberation time series is of primary interest. The first example is reverberation in a Pekeris waveguide, where other known numerical results are available for comparison. The second example is reverberation in a wedge-shaped waveguide, demonstrating the new formulation in a range-dependent environment.

II. FORMAL RESULTS

The primary goal of this work is to develop a numerically efficient model for reverberation in range-dependent waveguides, applicable at low to mid-frequencies (nominally 200 Hz to 10 kHz). Attention will be restricted to scattering by roughness of the water-seafloor interface as well as by buried rough interfaces, such as the basement. Both the sediment and basement (if any) will be treated as acoustic fluids, i.e., shear effects will not be included in the model. A two-scale approach[24–26] will be used in which the relief of the seafloor is expressed as the sum of a slowly varying, large-scale part and a small-scale part. It is assumed that the slowly varying part of the seafloor relief (bathymetry) is known and that a propagation solution is available via some efficient method such as the parabolic equation. This will be referred to as the "zeroth-order" solution. This part of the problem incorporates range dependence, and the variation of water depth and seafloor properties may be as extreme as the numerical solution method allows. The small-scale part is responsible for acoustic scattering and will be treated using first-order perturbation theory. This will be referred to as the "first-order" solution.

The primary difference between the present model and previous work lies in the manner in which the large-scale relief is modeled and in the manner in which the large and small scales interact. For example, the parabolic equation method has been applied to calculate reverberation due to bottom roughness,[27] where the details of the roughness are taken into account by taking very small steps, hence this approach is not numerically efficient. In most applications of the two-scale (or composite-roughness) approximation, both large- and small-scale relief are taken to be random with the the effect of large scales treated statistically. The interaction

Author's complimentary copy

of the large and small scales is handled in an *ad hoc* fashion with the large scales assumed to simply tilt the landscape and, in some cases, cause shadowing. In the method of this article, a two-scale approach is developed from first principles, and no *ad hoc* rules are invoked. The price paid for this more physically based approach is that formal-average results are not obtainable, and Monte Carlo methods must be used with the small-scale relief drawn from a random ensemble.

The method of this article faces the same issue of separation of scales that has confronted two-scale models in the past. Scale separation can be viewed as a filtering operation in which a low-pass filter yields the large-scale relief, and a high-pass filter (using the same cutoff) yields the small-scale relief. For a given scenario, one must find a cutoff such that both the zeroth-order and first-order solutions are accurate. In some problems, no such cutoff exists, but when it does exist, the proper choice of cutoff frequency becomes the primary issue. Once this choice is made, the final results should be somewhat insensitive the exact value employed. The authors are unaware of any set of simple, general criteria that will guide the choice of cutoff for the various applications envisioned. The scale separation problem is not at issue in this article as the zeroth-order interface for all problems considered is flat, although it is sloping in one example.

The general problem is illustrated in Fig. 1. A point source is situated at position $\mathbf{r}_0$, and one wishes to predict the bistatic, average reverberation intensity time series at position $\mathbf{r}$. This section will assume a single-frequency source, and the issues of Fourier synthesis of time series and Monte Carlo averaging will be deferred to later sections. The source is assumed to produce unit pressure at unit distance, and the pressure at the general point $\mathbf{r}$ is the Green's function, satisfying the following equation:

$$\rho(\mathbf{r})\nabla\cdot\left[\frac{\mathbf{1}}{\rho(\mathbf{r})}\nabla\mathbf{G}(\mathbf{r},\ \mathbf{r_0})\right]+\mathbf{k^2}(\mathbf{r})\mathbf{G}(\mathbf{r},\ \mathbf{r_0})=-4\pi\delta(\mathbf{r}-\mathbf{r}_0). \tag{1}$$

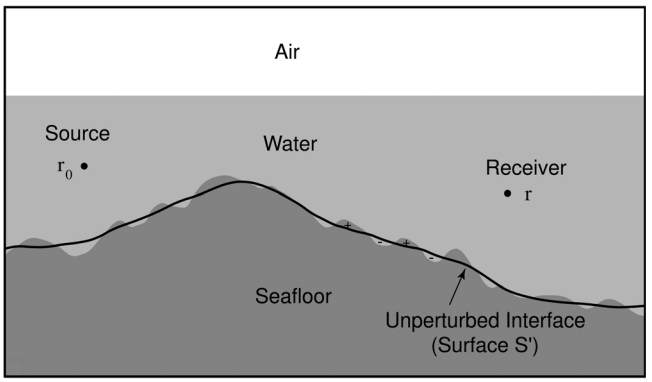

FIG. 1. A range-dependent waveguide with small-scale perturbation in bathymetry. The solid curve indicates the smooth part of the bathymetry for which a field soution is presumed known in the form of the Green's function $G^{(0)}(\mathbf{r},\ \mathbf{r}_0)$. The shaded regions define the "perturbed" problem with the interface between dark and light shades representing the "true" bathymetry. Although not shown in the figure, both the water column and the seafloor may be heterogeneous as long as these heterogeneities are included in the calculation of $G^{(0)}(\mathbf{r},\ \mathbf{r}_0)$.

The density, $\rho(\mathbf{r})$, and wavenumber, $k(\mathbf{r})$, can be position dependent, and attenuation is included by allowing $k(\mathbf{r})$ to be complex. The source and field points are not restricted to the water column; one or the other, or both, may be within the seafloor. Expression (1) assumes that the seafloor behaves as an acoustic fluid, thus the model does not include shear waves. In the remainder of this article, the scattered pressure field at position $\mathbf{r}$, due to a unit point source (defined in the preceding text) at position $\mathbf{r}_0$ will be denoted $p_s(\mathbf{r},\ \mathbf{r}_0)$ and defined as the first-order solution for the field. To simplify the exposition, essential results will be presented in this section with the derivation deferred to Appendix A. The derivation follows a method given by Ivakin[28] and requires somewhat abstract notation for the general result. To avoid immediate involvement in notational issues, the discussion will be initiated with a less general problem: semi-infinite water and sediment half-spaces, each being homogeneous with regard to sound speed and density. The boundary between these two media will be assumed to be flat except for the small-scale roughness. The scattered field at a point $\mathbf{r}=(x,\ y,\ z)$ in the water column due to a unit source in the water column at $\mathbf{r}_0=(x_0,\ y_0,\ z_0)$ is given by the expression

$$\begin{aligned}p_s(\mathbf{r},\mathbf{r}_0)=\frac{\rho_1}{4\pi}\int dx'dy'\Big[&\omega^2(\kappa_2-\kappa_1)G^{(0)}(\mathbf{r}',\mathbf{r})G^{(0)}(\mathbf{r}',\mathbf{r}_0)\\&-\left(\frac{1}{\rho_2}-\frac{1}{\rho_1}\right)\nabla' G^{(0)}(\mathbf{r}',\mathbf{r})|_{z'=0^+}\\&\cdot\nabla' G^{(0)}(\mathbf{r}',\mathbf{r}_0)|_{z'=0^-}\Big]\zeta(x',y').\end{aligned} \tag{2}$$

The integration is over the horizontal plane at $z'=0$ that separates water and seafloor, thus, $\mathbf{r}'=(x',\ y',\ 0)$. The perturbed water-seafloor boundary is given by $z'=\zeta(x',\ y')$. The subscripts 1 and 2 refer to water and seafloor, respectively, and the corresponding compressibilities are denoted

$$\kappa_i=\frac{1}{c_i^2\rho_i},\quad i=1,2 \tag{3}$$

with c_i being the sound speed and ρ_i being the density. Attenuation in the seafloor is incorporated by allowing k_2 (hence c_2) to be complex.

In Eq. (2), the Green's functions for the zeroth-order problem (two semi-infinite half spaces separated by the plane $z'=0$) appear. The zeroth-order solution for this case can be found, e.g., by means of wavenumber integration. The two Green's functions of interest are $G^{(0)}(\mathbf{r}',\ \mathbf{r}_0)$ for the field at the integration point $\mathbf{r}'$ due to a source at the true source position $\mathbf{r}_0$, and $G^{(0)}(\mathbf{r}',\ \mathbf{r})$ for the field at the integration point due to a source at the field point $\mathbf{r}$ The gradient of $G^{(0)}(\mathbf{r}',\ \mathbf{r}_0)$ is to be evaluated immediately below the interface, while the gradient of $G^{(0)}(\mathbf{r}',\ \mathbf{r})$ is to be evaluated immediately above the interface. As the pressure field is continuous across the interface, the factor $G^{(0)}(\mathbf{r}',\ \mathbf{r})G^{(0)}(\mathbf{r}',\ \mathbf{r}_0)$ can be evaluated either above or below. In fact, the same is true for the x'- and y'-partial derivatives. The normal gradient of the pressure field, however, is discontinuous across the interface, so care must be taken in the evaluation of the z' component of the gradient. As noted in Appendix A, the displacement matching

Author's complimentary copy

condition that relates the normal derivative values on either side of the interface can be used to show that it does not matter which of the two normal derivatives in the dot product of Eq. (2) is evaluated above as long as the other is evaluated below. Using this symmetry, it follows that the scattered field obeys reciprocity, that is, $p_s(\mathbf{r}, \mathbf{r}_0) = p_s(\mathbf{r}_0, \mathbf{r})$. An equally important property of this solution is that it agrees with conventional small-roughness perturbation theory. In particular, if the mean-square scattered pressure is used to extract a scattering cross section, the result will agree with formally-average perturbation theory as will be shown in the next section.

Expression (2) applies when both the source and field points are in the water column, $z_0 > 0$, $z > 0$. The case $z_0 > 0$, $z < 0$ is of interest in modeling the acoustic field that penetrates the seafloor. This case has been published by Thorsos and co-workers[29] with a resulting expression that is equivalent to Eq. (2) except with the density prefactor ρ_1 replaced by ρ_2. The opposite case, with source in the seafloor and field point in the water gives an expression identical to Eq. (2), including the prefactor ρ_1. The remaining case, with both source and field point in the seafloor ($z_0 < 0$, $z < 0$), uses the same expression as that for source in the water and field point in the sediment. Note that identity of expressions does not imply identity of scattered pressures because the unperturbed Green's functions that enter these expressions may have different values. All of the preceding relationships lead to the reciprocity statement $p_s(\mathbf{r}_b, \mathbf{r}_a)/\rho_b = p_s(\mathbf{r}_a, \mathbf{r}_b)/\rho_a$ given in Ref. 21 (Chap. 8) for the zeroth-order case, yet applicable in all cases.

Expression (2) is, in fact, much more general than might be first supposed. It is applicable to horizontally stratified waveguides if the zeroth-order Green's functions are evaluated for the waveguide. The source and field points may be either in the water or seafloor, and the density prefactor must be evaluated at the field point. The densities, ρ_i, and compressibilities, κ_i, in the integrand are to be evaluated at $z' = 0^+$ if $i = 1$ (water) or $z' = 0^-$ if $i = 2$ (seafloor). Thus the present model can be applied to range-independent waveguides, where modal calculations can be used to evaluate the zeroth-order Green's functions and their gradients. The following section contains an example in which this model is applied to a finely layered seafloor.

All of the cases discussed in the preceding text are special cases of a more general result for range-dependent waveguides, derived in Appendix A. The general setting is depicted in Fig. 1, and the scattered field is given by

$$p_s(\mathbf{r}, \mathbf{r}_0) = \frac{\rho(\mathbf{r})}{4\pi} \int dS' \Big[\left[\omega^2(\kappa_2 - \kappa_1)\right] G^{(0)}(\mathbf{r}', \mathbf{r}) G^{(0)}(\mathbf{r}', \mathbf{r}_0) - \left(\frac{1}{\rho_2} - \frac{1}{\rho_1}\right) \nabla' G^{(0)}(\mathbf{r}', \mathbf{r})|_{w'=0^+} \cdot \nabla' G^{(0)}(\mathbf{r}', \mathbf{r}_0)|_{w'=0^-} \Big] \zeta(\mathbf{r}'). \quad (4)$$

Because the zeroth-order water-seafloor interface is not flat, a surface integral replaces the x'-y'-integral in Eq. (2). The coordinate w' is normal to the zeroth-order interface at every point. Symmetry with respect to evaluation of the two Green's function factors at either $w' = 0^+$ or $w' = 0^-$ still applies, so reciprocity is respected. The densities, ρ_i, and compressibilities, κ_i, are to be evaluated at $w' = 0^+$ if $i = 1$ (water) or $w' = 0^-$ if $i = 2$ (seafloor). Note that these parameters may be functions of the transverse coordinates involved in the surface integration and that the compressibility is a complex function of position in the seafloor. Furthermore, the scattering interface is not restricted to the water-seafloor interface; it can be a buried interface in the sediment, a sediment-basement interface, for example. Finally, the small roughness $\zeta(\mathbf{r})$ is always measured normal to the local tangent plane of the slowly varying surface.

Computation of the Green's functions and their gradients is more difficult in the range-dependent case. In this article, a parabolic equation method will be used with special effort to compute the gradients near the zeroth-order interface. In Sec. V, reverberation in a wedge-shaped waveguide will be computed as an example of the application of Eq. (4).

III. BOTTOM BACKSCATTER FOR HOMOGENEOUS HALF-SPACE

Equation (2) of the previous section will be applied to a simple backscatter scenario for which the theoretical scattering cross section is available. This provides a partial validation of the simulation results. The environment is appropriate for bottom backscatter measurement where the sea surface is far away so its effects can be easily separated in time. As such, the water depth is assumed to be infinite, and the medium consists of two fluid half-spaces separated by a rough seafloor. The upper half-space is homogeneous water with sound speed c_1 and density ρ_1. The attenuation in water is ignored. The lower half-space is homogeneous sediment with sound phase speed c_{2p}, density ρ_2, and attenuation factor δ_2. The complex speed is $c_2 = c_{2p}/(1 + i\delta_2)$. The coordinate system is defined such that the x and y axes are horizontal. The random seafloor is given by $z = \zeta(x, y)$, assumed to have zero mean. The z axis points upward with the mean seafloor as its origin. This is a special case of the general rough interface discussed in the previous section because the slowly varying component of the roughness is simply a constant.

The source and receiver are co-located at $(0,0,z_0)$. The backscattered sound field is to be calculated for a number of independent realizations of the rough seafloor. These calculations will result in a set of backscattered time series, which will form the statistical ensemble for estimating the bottom scattering cross section. The theoretical scattering cross section for this case is known[21] (Chap. 13) and will be compared with our simulation results. This section contains many details that will be common for other sections. It is divided in subsections to make it easier to follow.

A. Synthesis of rough surfaces

In this special backscatter geometry with range-independent environment, the only quantity depending on the azimuth angle ϕ under the integral (2) is the rough surface $\zeta(x, y) = \zeta(R, \phi)$ when the horizontal dimensions are expressed in polar coordinates. Therefore, if one-dimensional realizations of the roughness are obtained by pre-summing

Author's complimentary copy

over the azimuth, $\eta(R) = \int_0^{2\pi} \zeta(R,\phi)d\phi$, Eq. (2) is simplified to the one-dimensional integral:

$$p_s(z_0) = \frac{\rho_1}{4\pi}\int_0^\infty R'dR'\eta(R')\left[\omega^2(\kappa_2-\kappa_1)(G^{(0)}(r'))^2 - \left(\frac{1}{\rho_2}-\frac{1}{\rho_1}\right)\left(\frac{\partial G^0}{\partial R'}\right)^2 - \frac{\rho_2}{\rho_1}\left(\frac{1}{\rho_2}-\frac{1}{\rho_1}\right)\left(\frac{\partial G^{(0)}(z')}{\partial z'}\right)^2\right]\Bigg|_{z'=0^+}, \quad (5)$$

where the matching relationship between the vertical gradients in the upper and lower media has been used. For convenience, the dependence of the Green's functions on the source and receiver coordinates [both equal to $(0,0,z_0)$] has been suppressed. The characteristics of the rough interface $\zeta(x, y)$ are specified by the two-dimensional power-law power spectrum

$$W(\mathbf{K}) = \frac{w_2}{(K_0^2+K^2)^{\gamma_2/2}}, \quad (6)$$

where $\mathbf{K} = [K_x, K_y]$, $K_0 = 2\pi/L_0$, and L_0 defines the outer scale of the roughness. For examples in this section and next, $\gamma_2 = 3.25$, $L_0 = 10$ m, and $w_2 = 8.496\times10^{-6}\,\mathrm{m}^{4-\gamma_2}$. The procedure of obtaining realizations of $\eta(R) = \int_0^{2\pi}\zeta(R,\phi)d\phi$ through Hankel transforms is given in Appendix B and can also be found in Li *et al.*[30]

B. Zeroth-order field

To calculate the backscattered field in Eq. (5), the zeroth-order pressure field and its horizontal and vertical derivatives on the flat interface are needed. For the present range-independent problem, these quantities can be obtained by separation of variables and wavenumber synthesis[31] (Chap. 1). They are

$$\begin{aligned} G^{(0)}(r') &= \int_0^\infty \frac{i}{\beta_1}\{\exp[i\beta_1(z_0-z')] + V\exp[i\beta_1(z'+z_0)]\}\big|_{z'=0^+}J_0(KR')KdK,\\ \frac{\partial G^{(0)}(r')}{\partial z'} &= \int_0^\infty \{\exp[i\beta_1(z_0-z')] - V\exp[i\beta_1(z'+z_0)]\}\big|_{z'=0^+}J_0(KR')KdK,\\ \frac{\partial G^{(0)}(r')}{\partial R'} &= -\int_0^\infty \frac{i}{\beta_1}\{\exp[i\beta_1(z_0-z')] + V\exp[i\beta_1(z'+z_0)]\}\big|_{z'=0^+}J_1(KR')K^2dK, \end{aligned} \quad (7)$$

where V is the plane-wave reflection coefficient:

$$V = \frac{\rho_2\beta_1 - \rho_1\beta_2}{\rho_2\beta_1 + \rho_1\beta_2}, \quad (8)$$

with $\beta_1 = \sqrt{k_1^2-K^2}$, and $\beta_2 = \sqrt{k_2^2-K^2}$. In the first equation of (7), the first term is the direct arrival from the source to the seafloor and the second term the reflected arrival. The quantities in Eq. (7) are numerically evaluated along the interface to be fed into Eq. (5). When the integration point is in the far field of the source/receiver ($k_1z_0 \gg 1$), a ray form of Eq. (7) can be used through the stationary phase approximation:

$$\begin{aligned} G^{(0)}(r') &= \frac{e^{ik_1r'}}{r'}(1+V_0),\\ \frac{\partial G^{(0)}(r')}{\partial z'}\bigg|_{z=0^+} &= -i\beta_1^0(1-V_0)G^{(0)}(r'),\\ \frac{\partial G^{(0)}(r')}{\partial R'} &= ik_r^0(1+V_0)G^{(0)}(r'), \end{aligned} \quad (9)$$

where $\beta_1^0 = k_1\sin\theta_0$, $\beta_2^0 = \sqrt{k_2^2-(k_1\cos\theta_0)^2}$, $\tan\theta_0 = z_0/R'$, and V_0 is the reflection coefficient evaluated at the grazing angle θ_0. When these approximate zeroth-order terms are used, the scattered field is simplified to

$$p_s(z_0) = \frac{k_1^2}{2\pi}\int_0^\infty R'dR'\eta(R')\frac{e^{2ik_1r'}}{r'}\tau(R'), \quad (10)$$

where

$$\begin{aligned} \tau(R') &= \frac{1}{2}(1+V_0)^2\left[\frac{\rho_1}{k_1^2}\omega^2(\kappa_2-\kappa_1) + \left(\frac{1}{\rho}-1\right)\frac{a_k^2-\cos^2\theta(1-\rho)}{\rho}\right]\\ &= \frac{1}{2}(1+V_0)^2\left[\left(\frac{a_k^2}{\rho}-1\right) + \left(\frac{1}{\rho}-1\right)\frac{a_k^2-\cos^2\theta(1-\rho)}{\rho}\right] \end{aligned} \quad (11)$$

where $a_k = k_2/k_1$. It is shown in Appendix D that Eq. (10) results in the same expression for backscattering cross section as predicted by first-order perturbation theory. When the zeroth-order fields are obtained through either Eq. (7) or (9), the first-order scattered field at any frequency can be calculated using Eq. (5) or (10). For backscatter simulations, the zeroth-order field from the source to the scatterers and that from the scatterers to the receiver are the same, hence the computation time is half of that for the bistatic geometry. For different realizations for the rough interface, the same zeroth-order fields are used, making it efficient to calculate large numbers of scattered field realizations.

C. Fourier synthesis

Fourier synthesis is used to obtain a simulated pressure time series. In this case, the elapsed time after transmission

Author's complimentary copy

provides angular resolution of the scattered signal, hence of the scattering cross section. A Gaussian pulse with center frequency f_c is chosen in the form

$$s(t) = s_e(t)\cos(2\pi f_c t), \tag{12}$$

where

$$s_e(t) = \exp[-2(\pi\Omega t)^2] \tag{13}$$

is the baseband envelope. The pulse peaks at time zero with value unity and falls off exponentially versus the square of time. The baseband envelope has the following Fourier transform:

$$\begin{aligned} S_e(f) &= \frac{1}{2\pi}\int s_e(t)\exp(i2\pi ft))dt \\ &= \frac{1}{\Omega\sqrt{2\pi}}\exp\left(-\frac{f^2}{2\Omega^2}\right). \end{aligned} \tag{14}$$

The bandwidth is controlled by the parameter

$$\Omega = f_b/\sqrt{\log_e(2)}, \tag{15}$$

where f_b is the baseband frequency at which the signal frequency spectrum equals half peak power ($f_b = f_c/40$ in our simulations, giving a bandwidth of 5% of the center frequency). The highest difference frequency on either side of the center frequency is chosen to be at a value where the spectrum is X decibels below the peak spectrum,

$$|f - f_c| = \Omega\sqrt{\frac{X}{10\log_{10}(e)}}. \tag{16}$$

The value $X = 60$ is used for all examples in this paper. This determines the bandwidth over which the scattered field must be calculated. The choice of the frequency increment is dictated by the time window over which the time-domain scattered field is desired. This is achieved by choosing a maximum range r_{max} at which the roughness terminates. This termination point determines the smallest grazing angle that can be obtained.

D. Results

For the set of parameters given in Tables I and II, the zeroth-and first-order scattered field for a set of 100 realizations of the rough seafloor is obtained. The roughness relief realizations are statistically independent. Consequently, the scattered intensity realizations are also statistically independent. Thus the variance of the mean intensity from N realizations is reduced by a factor of $1/N$ compared to a single realization. For example, 100 realizations will reduce the variance to $1/100$, or the standard deviation to $1/10$ of the mean.

Small-roughness perturbation theory should be accurate for this example in which the product of RMS roughness and acoustic wavenumber is 0.115. The numerical data are used to estimate the backscattering cross section following the steps given in Appendix C. The results are compared to the theoretical backscattering cross section in Fig. 2. The model is for the same environment as the simulations, and the frequency is 1000 Hz. The angular range shown for the comparison is 4° to 60°, over which the two are consistent, including the abrupt change near 28°, the critical angle.

TABLE I. Environmental parameters used in simulations. All simulations use water sound speed 1500 m/s and density 1000 kg m^{-3}.

Case	Layer No.	Thickness (m)	Sound speed (m/s)	Density (kg m^{-3})	Attenuation (dB/λ)
Two half spaces	1	∞	1700	2000	0.5
Approximate Lambert	1	0.2	1446.2	1400	0.05
	2	∞	1700	2000	0.5
Waveguide	1	∞	1700	2000	0.5
Wedge	1	∞	1700	1500	0.5

IV. APPROXIMATE LAMBERTIAN SCATTERING

Lambert's law is a bottom scattering cross section widely used in both applied and theoretical models because of its simplicity. For backscatter, the cross section is proportional to the second power of the sine of the grazing angle:

$$\sigma_l(\theta) = \mu\sin^2\theta, \tag{17}$$

where μ is a constant. Lambert's law is a concept related to multiple scattering in low-loss media, and single-scattering theory cannot give Lambert's law over all angles and frequency. However, it is desirable to have a physics-based model that resembles the Lambert model in some useful angular and frequency range, so that results from the physics-based model can be compared to those obtained from codes that assume Lambertian scattering. Here first-order rough interface scattering theory is applied to mimic Lambertian scattering. Because small grazing angles are often the important regime for long-range propagation and reverberation, our limited goal is to find a region of small grazing angles for a given frequency where the first-order rough interface theory fits Lambert's law.

As the grazing angle approaches zero, the interface scattering cross section also necessarily goes to zero as required by conservation of energy. The scattering cross section of first-order rough surface scattering theory approaches zero as the fourth power of grazing angle, the same as that predicted for the rough sea surface (pressure release boundary condition). For this theory to mimic Lambertian scattering, which is proportional to the second power of the grazing angle, a thin, soft layer above the rough interface is added, hence making the local grazing angle steeper. Adding a single layer can only fit the Lambert cross section in a finite range of grazing angles for fixed frequency. Adding multiple layers, in principle, can increase the angular range of fit. In adding a single layer, one new feature of the theory will also be shown.

The environment is shown in Fig. 3, where all the environmental parameters are the same as in those of the

Author's complimentary copy

TABLE II. Geometrical and other simulation parameters.

Case	f_c (Hz)	Source coordinate (m)	Rec. coordinate (m)	No. Realiz.	Surface length, L (m)	No. points, N
Two half spaces	1000	150 (From bottom)	150 (From bottom)	100	8,000	20,000
Approximate Lambert	1000	150 (From bottom)	150 (From bottom)	100	8,000	20,000
Waveguide	250	15 (From surface	25 (From surface)	100	10,000	10,000
Wedge	250	35 (From surface)	35 (From surface)	100	4,000	4,000

previous section except that a 20-cm mud layer with sound speed lower than the water sound speed is put above the rough sand sediment half-space (Table I). The thin, slow layer will tend to increase the local grazing angle when the incident acoustic wave impinges on the rough interface, hence decreasing the rate at which the cross section approaches zero at small grazing angles.

The formula applicable to this problems is

$$p_s(z_0) = \frac{\rho(z_0)}{4\pi}\int_0^\infty R'dR'\eta(R')\left[\omega^2(\kappa_2-\kappa_1)(G^{(0)}(r'))^2 - \left(\frac{1}{\rho_2}-\frac{1}{\rho_1}\right)\left(\frac{\partial G^0}{\partial R'}\right)^2 - \frac{\rho_2}{\rho_1}\left(\frac{1}{\rho_2}-\frac{1}{\rho_1}\right)\left(\frac{\partial G^{(0)}(z')}{\partial z'}\right)^2\right]\Bigg|_{z'=-0.2^+}. \quad (18)$$

This expression is very similar to Eq. (5) with the following differences: First, the mean of the rough interface is at $z=-0.2$ m instead of zero. Second, the density $\rho_1=1400$ kg/m^3 refers to the density in the mud layer, rather than that in water. The density ρ_2 remains that for the sand half-space (Table I). Third, the Green's function is one linking the source to a point on the mean interface at $z=-0.2$ m. The Green's function and its gradients are numerically calculated using wavenumber integration for the three-layer scenario. All other quantities are the same as in the previous section, and simulation parameters are given in Table II. The results in the form of backscattering strength are shown in Fig. 4, where the simulation agrees with perturbation theory as expected. Both, in turn, agree with Lambert's law over the angle range of 5° to 28° with the latter being the critical angle. This demonstrates that one can use the three-layer model to mimic Lambertian scattering over these angles in the neighborhood of 1 kHz.

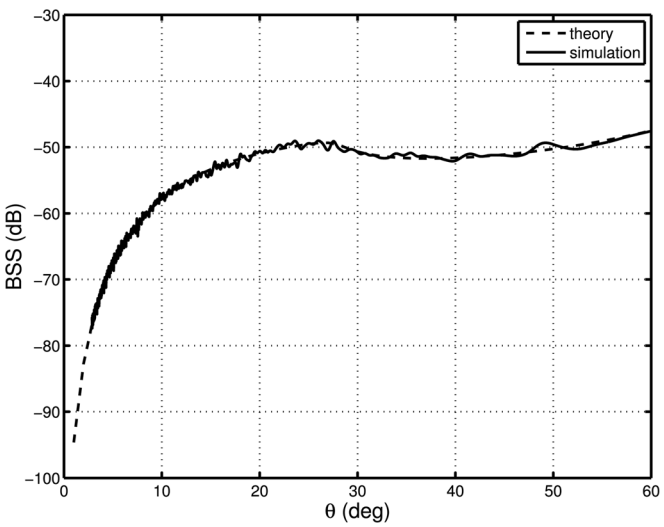

FIG. 2. Comparison of backscattering strength as a function of grazing angle calculated from the mean-square pressure of 100 realizations to the perturbation theory model for the two-half-space case.

V. REVERBERATION IN 2D WAVEGUIDES

The first-order perturbation result will be applied to two waveguide reverberation problems. The first is a range-independent problem for which a solution from numerically averaged perturbation theory is available for comparison. The second is reverberation in a wedge-shaped waveguide. Both examples are in two-dimensional geometry where the environment has no y dependence. In both cases, the parabolic equation[32] is used to calculate the zeroth-order Green's function. The use of PE to calculate reverberation has been reported previously by Lingevitch and LePage.[27] The difference here is that the parabolic equation is used to calculate the Green's function corresponding to the slowly changing environment, leaving the scattering problem to be handled by perturbation theory, hence saving computation time.

The first problem is one defined by the Reverberation Modeling Workshops sponsored by the U.S. Navy.[9,33] The environment is a 50-m deep isovelocity waveguide with a homogeneous sandy sediment half-space. The water-sediment interface is rough with the following 1D power spectrum that was defined for the "typical" roughness case:[9,33]

$$W_{1D}(K) = \frac{h^2 K_L}{\pi(K_L^2+K^2)}, \quad (19)$$

where $h=0.316$ m, and $K_L=0.1$ m^{-1} for the numerical examples for the rest of the paper. The source depth is 15 m

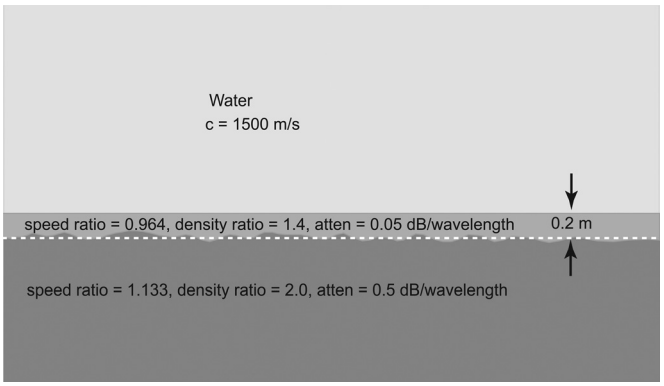

FIG. 3. Layered seafloor model used to mimic Lambertian scattering over limited angular and frequency ranges.

Author's complimentary copy

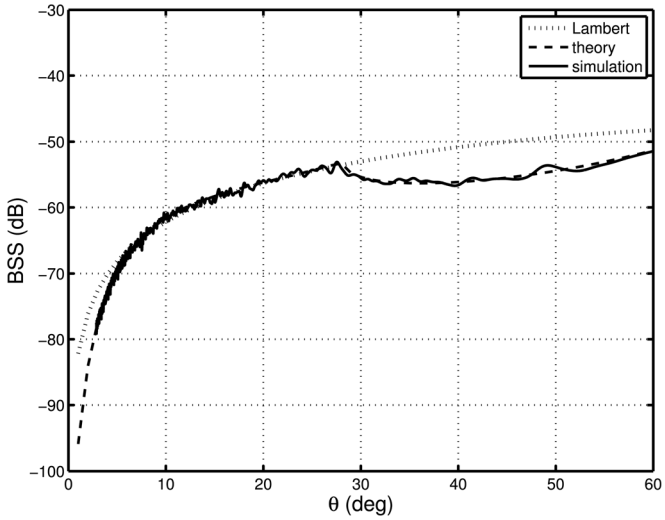

FIG. 4. Comparison of model and simulation approximating Lambert's law. The simulation curve and the model curve from perturbation theory are consistent for all grazing angles. These two are consistent with Lambert's law over the angle range of 5° to 28°.

and the receiver depth is 25 m at the same horizontal range. The narrow-band source has a center frequency of 250 Hz. Details of all parameters involved are found in Yang *et al.*[9]

The formula for this problem takes on the following form:

$$p_s(z,z_0)=\frac{\rho_1}{4\pi}\int_0^\infty x'dx'\zeta(x')\Big[\omega^2(\kappa_2-\kappa_1)\times\left(G^{(0)}(z_0,x',z')G^{(0)}(z,x',z')\right)-\left(\frac{1}{\rho_2}-\frac{1}{\rho_1}\right)\times\left(\frac{\partial G^{(0)}(z_0,x',z')}{\partial x'}\frac{\partial G^0(z,x',z')}{\partial x'}\right)-\frac{\rho_2}{\rho_1}\left(\frac{1}{\rho_2}-\frac{1}{\rho_1}\right)\times\left(\frac{\partial G^{(0)}(z_0,x',z')}{\partial z'}\frac{\partial G^{(0)}(z,x',z')}{\partial z'}\right)\Big]\Big|_{z'=0^+}. \quad (20)$$

In this expression, z_0 is the source depth, and z is the receiver depth. The Green's functions connect the source at $(0, z_0)$ or the receiver at $(0, z)$ to points just above the mean surface (x', z'). These Green's functions and their gradients for the range-independent problem can be obtained through a number of methods, including the normal mode method. The PE method was chosen here because the PE approach can also be used for range-dependent problems. Once the Green's functions and their gradients are obtained, the same steps as those in Sec. III can be taken to calculate reverberation time series for different rough surface realizations. Simulation parameters are given in Table II. Figure 5 compares the results using the PE method to those obtained using the normal mode method.[9] The two results are essentially identical for times greater than 1 s. The discrepancy between the two for times shorter than 1 s is due to the fact that neither method treats high-wavenumber propagation properly as both are intended only for computation of long-range reverberation. The purpose of the comparison is primarily to establish using the PE as a viable method for range-dependent reverberation problems. Incidentally, favorable results from the

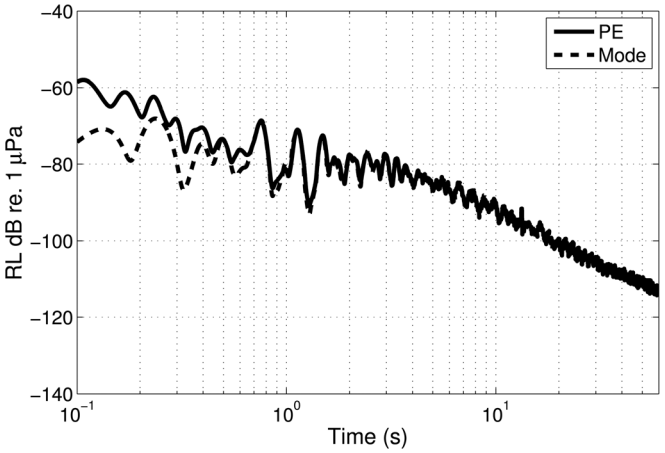

FIG. 5. Comparison of mean reverberation level vs time from 100 rough surface realizations using the PE and normal mode methods.

energy-flux[18] and ray-tracing methods for this range-independent example can be found in Ref. 33.

Reverberation in a wedge-shaped waveguide is discussed next. The waveguide is the "ASA wedge" (Ref. 34). The waveguide has isovelocity sound speed of 1500 m/s and a sloping bottom of 2.86°. The bottom sound speed is 1700 m/s with an attenuation coefficient of 0.5 dB per wavelength and sediment-to-water density ratio of 1.5 (Table I). The source and receiver are co-located at 35 m depth where the water depth is 200 m. The acoustic source spectrum is the same as in the range-independent waveguide. The formula for this case is

$$p_s(z_0)=\frac{\rho_1}{4\pi}\int_0^\infty l'dl'\zeta(l')\Big[\omega^2(\kappa_2-\kappa_1)(G^{(0)}(z_0,l'))^2-\left(\frac{1}{\rho_2}-\frac{1}{\rho_1}\right)\left(\frac{\partial G^0}{\partial l'}\right)^2-\frac{\rho_2}{\rho_1}\left(\frac{1}{\rho_2}-\frac{1}{\rho_1}\right)\left(\frac{\partial G^{(0)}}{\partial n'}\right)^2\Big]\Big|_{above\ \ bottom}. \quad (21)$$

Several items in this expression need clarification. First, l' is along the sloping bottom. Second, the rough interface $\zeta(l)$ is measured normal to the sloping bottom. Third, the gradient in the last term involving $\partial n'$ is the gradient normal to the sloping bottom. Finally, the Green's function and its gradients are calculated using PE and evaluated along and just above the sloping bottom. Because the source and receiver are co-located, the Green's function needs only to be calculated once for each frequency, and the quantities needed are the pressure field and its horizontal and normal gradients along the water-bottom interface. If the source and receiver are not co-located, then the Green's functions from both the source and the receiver to the water-bottom interface will be required, making the computational time twice as long as that for the monostatic case. The number of frequencies for which the Green's functions are needed depends on the acoustic source bandwidth. The number of realizations does not impact the computational load on the Green's functions.

The reverberation level is calculated from 100 realizations with the simulation parameters given in Table II and

Author's complimentary copy

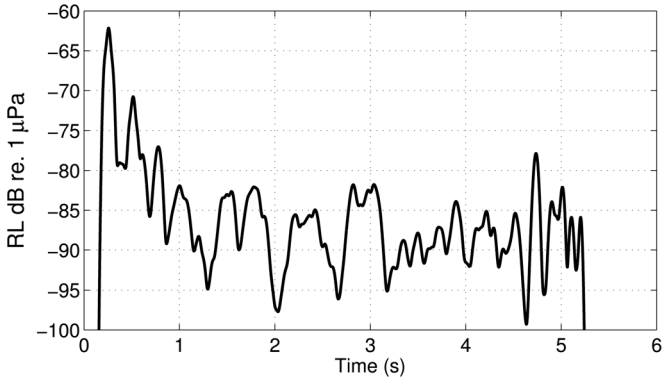

FIG. 6. Mean reverberation level vs time from 100 realizations for a wedge-shaped waveguide.

with the results given in Fig. 6. One interesting feature is that the reverberation level remains roughly a constant for time greater than 1 s. It is known that sound propagating upslope tends to gradually shift energy to higher grazing angles. The portion of energy shifted to angles above the critical angle will be lost in the sediment. From a modal point of view, high-order modes will be cut off first, followed by lower-order modes. Therefore, there seems to be a contradiction that while the total propagating energy decreases going upslope, the reverberation level does not decrease. A closer examination reveals that the sound intensity along the sloping bottom does not have a strong decrease until all modes are cut off toward the end of the wedge. Because the scatterers are on the bottom, the nearly range-independent intensity along the bottom is consistent with the observed steady reverberation level for the two-dimensional case.

VI. SUMMARY

A rough-interface reverberation model has been developed using first-order perturbation theory, where the unperturbed background interface is allowed to be arbitrary in shape, and the medium surrounding the rough interface can be heterogeneous and layered. The advantage of this approach for calculating the reverberation field is that the slowly changing unperturbed environment, which does not contribute to backscatter but alters forward propagation, can be handled by fast numerical methods such as the parabolic equation. In this model, the reverberation field is calculated for realizations of the small roughness superimposed on the slowly varying interface. The overall increased computational speed comes from the fact that numerical steps in range need only accommodate the slow range dependence and are much greater than the acoustic wavelength. This contrasts with the wavelength-scale range steps required by Lingevitch and LePage,[27] for example. The computation speed is further enhanced because the forward propagating field is common to all realizations; obtaining large numbers of realizations does not require additional time proportional to the number of realizations. The primary purpose of this model is to provide a physics-based approach that is reasonably fast, so the accuracy of faster, but possibly less accurate, models can be checked.

ACKNOWLEDGMENTS

The authors appreciate help from Jie Yang, who furnished the normal mode results for example 3. The work was supported by the Office of Naval Research, Ocean Acoustics.

APPENDIX A: PERTURBATION THEORY

This appendix provides a derivation of the main perturbation-theoretic result, (4). The derivation employs the unified approach given by Ivakin[28] in which roughness scattering is treated as a form of volume scattering. Deformation of an interface causes a position-dependent change in acoustic parameters, and an exact integral equation is developed for the resultant change in the pressure field. This equation can be expressed in the following form:

$$G(\mathbf{r},\mathbf{r}_0) = G^{(0)}(\mathbf{r},\mathbf{r}_0) + \frac{\rho(\mathbf{r})}{4\pi}\int\left\{[\omega^2(\kappa-\kappa_0)]G^{(0)}(\mathbf{r}',\mathbf{r})G(\mathbf{r}',\mathbf{r}_0) - \left(\frac{1}{\rho}-\frac{1}{\rho_0}\right)\nabla' G^{(0)}(\mathbf{r}',\mathbf{r})\cdot\nabla' G(\mathbf{r}',\mathbf{r}_0)\right\}d^3r'. \quad \text{(A1)}$$

As in all other parts of this article, $\exp(-i\omega t)$ time dependence is assumed. Equation (A1) includes a prefactor $\rho(\mathbf{r})$ not appearing in Ref. 28 owing to differing definitions of the Green's function. This expression is quite general with no limitations on the structure of the acoustic media (apart from the assumption of fluid behavior) and with no restriction on the location of the source and receiver. With reference to Fig. 1, $G^{(0)}(\mathbf{r}, \mathbf{r}_0)$ in Eq. (A1) is the "zeroth-order" Green's function for the unperturbed, smooth bathymetry. It gives the field at point $\mathbf{r}$ due to a unit point source situated at $\mathbf{r}_0$. This Green's function is the solution of

$$\rho_0(\mathbf{r})\nabla\cdot\left[\frac{1}{\rho_0(\mathbf{r})}\nabla G^{(0)}(\mathbf{r},\mathbf{r}_0)\right] + k_0^2(\mathbf{r})\,G^{(0)}(\mathbf{r},\ \mathbf{r}_0) = -4\pi\delta(\mathbf{r}-\mathbf{r}_0), \quad \text{(A2)}$$

where $\rho_0(\mathbf{r})$ is the position-dependent mass density (for both the unperturbed seafloor and water column), and $k_0(\mathbf{r})$ is the position-dependent unperturbed wavenumber. Wavenumber and sound speed c are related by $\omega = ck$, and both sound speed and wavenumber may be complex with imaginary parts that determine attenuation. In Eq. (A1), κ is the position-dependent compressibility, related to density and sound speed as follows:

$$\kappa = \frac{1}{c^2\rho}. \quad \text{(A3)}$$

The position dependencies of compressibility, sound speed, and density have not been indicated in Eq. (A3) for the sake of simplicity. This equation refers to the true seafloor acoustic parameters, but the same relation holds for the unperturbed parameters.

The "true" Green's function in Eq. (A1) is denoted $G(\mathbf{r}, \mathbf{r}_0)$, and is the solution of Eq. (1) in which the density and wavenumber are given their true values, that is, the values corresponding to the true bathymetry indicated in Fig. 1. Departure of the true bathymetry from the smooth

Author's complimentary copy

bathymetry (solid line in Fig. 1) results in changes in density and compressibility with the new position-dependent acoustic parameters indicated in Eq. (A1) by the symbols ρ and κ. It is important to realize that the new parameters differ from the old only in small lens-shaped regions near the smooth interface. In particular, for the water-sediment interface, the parameters change from water to sediment values for those regions where the true interface lies above the smooth interface. Similarly, they change from sediment to water values for those regions where the true interface lies below the smooth interface. For buried interfaces, the changes are those dictated by the two different sediment types.

Use of the term "perturbed" suggests that the changes between the parameters for the true and zeroth-order problems are small. In fact, Eq. (A1) is exact, and these perturbations can be arbitrarily large. In this article, however, the change in bathymetry is assumed to be small, so that a relatively simple perturbative solution of Eq. (A1) is possible. This solution method parallels one given by Ivakin.[28]

The scattered field will be defined as the difference between the zeroth-order field and the exact field. In the small-roughness approximation, the scattered field is computed to first order in the perturbation of the bathymetry, here denoted $\zeta(\mathbf{r}')$, and illustrated in Fig. 7. The volume integration in Eq. (A1) is taken over the thin lens-shaped regions between the perturbed and unperturbed interfaces. The scattered field to first order in $\zeta(\mathbf{r}')$ can be written as

$$p_s(\mathbf{r},\ \mathbf{r}_0) = \frac{\rho(\mathbf{r})}{4\pi}\int dS' \int dw' \Bigg\{ \omega^2(\kappa-\kappa_0)G^{(0)}(\mathbf{r}',\ \mathbf{r})G^{(0)}(\mathbf{r}',\ \mathbf{r}_0) - \left(\frac{1}{\rho}-\frac{1}{\rho_0}\right)\left[\nabla'_\perp G^{(0)}(\mathbf{r}',\ \mathbf{r})\cdot\nabla'_\perp G^{(0)}(\mathbf{r}',\ \mathbf{r}_0) + \frac{\partial}{\partial w'}G^{(0)}(\mathbf{r}',\ \mathbf{r})\frac{\partial}{\partial w'}G^{(0)}(\mathbf{r}',\ \mathbf{r}_0)\right]\Bigg\}, \tag{A4}$$

where the S' integral is a surface integral over the unperturbed interface and the w' integral is over the coordinate normal to the unperturbed interface. The range of the w' integral is set by the unperturbed and perturbed interfaces and is $[0,\ \zeta]$ for regions where the perturbed interface lies above the unperturbed interface ($\zeta>0$) and $[\zeta,\ 0]$ for the other regions ($\zeta<0$). In the integral over w', the zeroth-order Green's function and its derivatives are approximated as constant. As a result, the w' integral introduces an overall factor ζ, from which it follows that (A4) gives a first-order correction to the zeroth-order field.

In Eq. (A4), the transverse and normal parts of the gradient are treated separately with the transverse part denoted $\nabla'_\perp$. This separation is employed because the normal derivative of the Green's function is discontinuous at the unperturbed boundary. In contrast, in the terms not involving normal derivatives, the Green's function and its transverse gradient are continuous across the unperturbed boundary and may be taken outside the w' integral without regard to whether they are evaluated above or below the smooth interface.

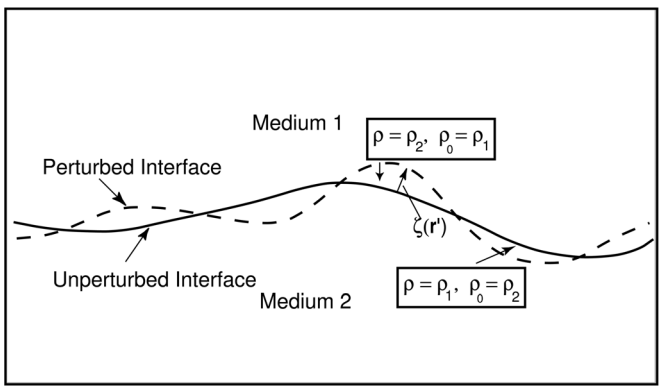

FIG. 7. Illustration of perturbation of smooth bathymetry by a small-scale roughness contribution measured by the normal displacement, $\zeta(\mathbf{r}')$.

In discussing the integral over w', it is necessary to break the integration region into two different parts. The "above" regions are those lens-shaped regions for which $\zeta>0$, and the "below" regions are those for which $\zeta<0$. Consistent with the first-order assumption, all acoustic parameters are taken to be independent of w', although they may be functions of the transverse coordinates. In the "above" regions, $\kappa-\kappa_0=\kappa_2-\kappa_1$, while in the "below" regions, $\kappa-\kappa_0=\kappa_1-\kappa_2$. Similar expressions hold for the density factors. As noted in the preceding text, the integration limits change between the two types of regions with the result that sign differences are cancelled, giving factors $\zeta(\kappa_2-\kappa_1)$ and $\zeta/(1/\rho_2-1/\rho_1)$ for both regions.

For the terms in Eq. (A4) that do not involve normal derivatives, the relevant integrals are, therefore,

$$\int(\kappa-\kappa_0)dw' = (\kappa_2-\kappa_1)\zeta(\mathbf{r}'), \tag{A5}$$

and

$$\int\left(\frac{1}{\rho}-\frac{1}{\rho_0}\right)dw' = \left(\frac{1}{\rho_2}-\frac{1}{\rho_1}\right)\zeta(\mathbf{r}'), \tag{A6}$$

where $\mathbf{r}'$ is evaluated on the unperturbed boundary, S'. Because the integrals are proportional to ζ, the corresponding terms in Eq. (A4) are of first order, as anticipated.

Because of the discontinuity at $w'=0$ in the normal derivative of the zeroth-order Green's function, care is required in treating the last term in Eq. (A4). This term is written in an ambiguous fashion, delaying specification of whether the normal derivatives are to be evaluated above or below

Author's complimentary copy

the smooth boundary. The first normal-derivative factor, $\partial/\partial w' G^{(0)}(\mathbf{r}', \mathbf{r})$, is straightforward and is evaluated at $w' = 0^+$ in the "above" regions and at $w' = 0^-$ in the "below" regions. This follows simply because, in the starting Eq. (A1), it is assumed that this factor is to be evaluated at the integration coordinate, which lies above the smooth interface in the "above" regions and vice versa. In the first-order approximation, this factor is assumed constant with respect to w', but it takes on different values in the "above" and "below" regions.

The second factor, $\partial/\partial w' G^{(0)}(\mathbf{r}', \mathbf{r}_0)$ is more subtle. Two choices are possible, each leading to a different approximation. One must decide whether to evaluate this derivative above or below the smooth boundary. It should be remembered that one seeks an approximation to the derivative of the exact Green's function. For the "above" regions, extrapolation from below should result in a reasonable approximation to the derivative over the region of integration, as this region has the physical properties of the lower medium. For the "below" regions, the opposite should be true. Two attractive properties result from this choice. First, reciprocity is respected, $p_s(\mathbf{r}, \mathbf{r}_0)/\rho(\mathbf{r}) = p_s(\mathbf{r}_0, \mathbf{r})/\rho(\mathbf{r}_0)$. Second, when the zeroth-order interface is flat, the result is found to be identical to that given by conventional small-roughness perturbation theory.

Defining

$$I = \int dw' \left(\frac{1}{\rho} - \frac{1}{\rho_0}\right) \frac{\partial}{\partial w'} G^{(0)}(\mathbf{r}', \mathbf{r}) \frac{\partial}{\partial w'} G^{(0)}(\mathbf{r}', \mathbf{r}_0), \quad \text{(A7)}$$

one finds for the "above" regions

$$I = \left(\frac{1}{\rho_2} - \frac{1}{\rho_1}\right) \frac{\partial}{\partial w'} G^{(0)}(\mathbf{r}', \mathbf{r})|_{w'=0^+} \times \frac{\partial}{\partial w'} G^{(0)}(\mathbf{r}', \mathbf{r}_0)|_{w'=0^-} \zeta(\mathbf{r}'), \quad \text{(A8)}$$

and for the "below" regions

$$I = \left(\frac{1}{\rho_2} - \frac{1}{\rho_1}\right) \frac{\partial}{\partial w'} G^{(0)}(\mathbf{r}', \mathbf{r})|_{w'=0^-} \times \frac{\partial}{\partial w'} G^{(0)}(\mathbf{r}', \mathbf{r}_0)|_{w'=0^+} \zeta(\mathbf{r}'). \quad \text{(A9)}$$

Expression (A9) can be brought into agreement with Eq. (A8) through use of the displacement matching condition

$$\frac{1}{\rho_1} \frac{\partial}{\partial w'} G^{(0)}(\mathbf{r}', \mathbf{r})|_{w'=0^+} = \frac{1}{\rho_2} \frac{\partial}{\partial w'} G^{(0)}(\mathbf{r}', \mathbf{r})|_{w'=0^-}. \quad \text{(A10)}$$

The transverse and normal derivative terms can be combined into a single three-dimensional gradient to obtain the final result, (4). The zeroth-order Green's function and its transverse gradient are continuous across the unperturbed boundary. Consequently, they can be evaluated at either $w = 0^+$ or $w = 0^-$. It should also be noted that the choice of evaluating the first normal derivative factor above the smooth boundary and the second below is arbitrary, and the above equation is still correct if the opposite choice is made. This follows from Eq. (A10). The source position $\mathbf{r}_0$ and the field point $\mathbf{r}$ may be separately chosen to be above or below the unperturbed boundary, so (4) is quite general and can be applied, e.g., to the problem of scattering from the water into the water as well as the problem of scattering from the water into the sediment.

APPENDIX B: PRE-SUMMED ROUGH SURFACE REALIZATIONS

The power spectrum for the 2D rough surface $\zeta(x, y)$ is assumed to be of the form:

$$W_\zeta(\mathbf{K}) = W_\zeta(K_x, K_y) = W_\zeta(K\cos\phi, K\sin\phi), \quad \text{(B1)}$$

which is normalized to the mean-square height of the roughness by $\sigma^2 = \int d^2K W_\zeta(\mathbf{K})$. A realization of the two-dimensional rough surface $\zeta(x, y)$ can be obtained from the two-dimensional wave vector distribution of the rough surface related by the two-dimensional Fourier transform:

$$\zeta(\mathbf{R}) = \zeta(x, y) = \int d^2k Z(\mathbf{K}) e^{i\mathbf{K}\cdot\mathbf{R}},$$
$$Z(\mathbf{K}) = \frac{1}{(2\pi)^2} \int d^2\mathrm{R}\zeta(\mathbf{R}) e^{-i\mathbf{K}\cdot\mathbf{R}}. \quad \text{(B2)}$$

The values of the distribution at two different wave vector values are independent Gaussian random variables, and the wave vector distributions have the following relation to the power spectrum:

$$\langle Z^*(\mathbf{K}) Z(\mathbf{K}')\rangle = W_\zeta(\mathbf{K})\delta(\mathbf{K} - \mathbf{K}'), \quad \text{(B3)}$$

where the brackets stand for ensemble average. Discretizing the first equation of (B2) to get a mean value of the distribution within a bin of wavenumbers:

$$z(\mathbf{K}) = \int_{\mathbf{K}}^{\mathbf{K}+\delta\mathbf{K}} Z(\mathbf{K}') d^2K', \quad \text{(B4)}$$

and using Eq. (B3)

$$\langle z^*(\mathbf{K}) z(\mathbf{K})\rangle = \int_{\mathbf{K}}^{\mathbf{K}+\delta\mathbf{K}} \int_{\mathbf{K}}^{\mathbf{K}+\delta\mathbf{K}} \langle Z^*(\mathbf{K}') Z(\mathbf{K}'')\rangle d^2K' d^2K''$$
$$= \int_{\mathbf{K}}^{\mathbf{K}+\delta\mathbf{K}} \int_{\mathbf{K}}^{\mathbf{K}+\delta\mathbf{K}} W_\zeta(\mathbf{K}')\delta(\mathbf{K}' - \mathbf{K}'') d^2K' d^2K''$$
$$\approx W_\zeta(\mathbf{K})\Delta K_x \Delta K_y, \quad \text{(B5)}$$

a realization of the two-dimensional surface $\zeta(\mathbf{R})$ can be obtained from the following expression:

$$\zeta(m\Delta x, n\Delta y) = \sqrt{2}\mathrm{Re}\left\{\sum_{p=0}^{N_x-1} \sum_{q=0}^{N_y-1} \sqrt{W_\zeta(p\Delta K_x, q\Delta K_y)\Delta K_x \Delta K_y} \times R_{qp} e^{i2\pi mp/N_x + i2\pi nq/N_y}\right\}, \quad \text{(B6)}$$

where $m = 0,1,2\ldots,(N_x - 1)$; $n = 0,1,2\ldots,(N_y - 1)$ and $R_{pq} = [N(0,1) + iN(0,1)]/\sqrt{2}$, with $N(0, 1)$ being a normally distributed random variable with zero mean and unit

Author's complimentary copy

variance. Multiplication by $\sqrt{2}$ and use of the real part of the complex realization yield a surface having the desired power spectrum W_ζ.

Azimuthally summed one-dimensional rough-surface realizations can be generated without resorting to the more numerically demanding generation of two-dimensional realizations. As noted earlier, the azimuthally summed realizations are defined by

$$\eta(R) = \int_o^{2\pi} \zeta\,(R,\ \phi) d\phi, \tag{B7}$$

and it is required that the equivalent two-dimensional realizations $\zeta(R,\ \phi)$ have the specified power spectrum $W_\zeta(\mathbf{K})$. For the one-dimensional surfaces, there exists a wavenumber distribution through Hankel transforms

$$\begin{aligned}\eta(R) &= \int_0^\infty K dK\, H(K) J_0(KR),\\ H(K) &= \int_0^\infty R dR\ \ \eta(R) J_0(KR).\end{aligned} \tag{B8}$$

This distribution is also statistically independent for different wavenumbers:

$$\langle H(K) H(K')\rangle = W_\eta(K)\delta(K-K'). \tag{B9}$$

The goal now is find a relation between the spectra $W_\zeta(\mathbf{K})$ and $W_\eta(K)$. Using Eq. (B8), the following relation can be obtained:

$$\begin{aligned}\langle H(K)H(K')\rangle = &\int_0^\infty RdR \int_0^\infty R'dR' J_0(KR) J_0(K'R')\\ &\times \langle \eta(R)^* \eta(R')\rangle.\end{aligned} \tag{B10}$$

Using Eqs. (B7), (B2), and (B3),

$$\begin{aligned}\langle \eta(R)\eta(R')\rangle &= \int_0^{2\pi} d\phi \int_0^{2\pi} d\phi' \langle \zeta(x,y)\zeta(x',y')\rangle\\ &= \int_0^{2\pi} d\phi \int_0^{2\pi} d\phi' \int d^2K\\ &\quad\times \int d^2K' e^{-i(\mathbf{K}\cdot\mathbf{R}-\mathbf{K}'\cdot\mathbf{R}')} \langle Z^*(K) Z(K')\rangle\\ &= \int d^2K \int d^2K' W_\zeta(\mathbf{K})\, \delta(\mathbf{K}-\mathbf{K}') \int_0^{2\pi} d\phi\\ &\quad\times \int_0^{2\pi} d\phi' e^{-iKR\cos(\phi-\theta)+iK'R'\cos(\phi'-\theta')}\\ &= (2\pi)^2 \int d^2K W_\zeta(\mathbf{K})\, J_0(KR) J_0(KR')\\ &= (2\pi)^3 \int KdK \overline{W}_\zeta(\mathrm{K})\, J_0(KR) J_0(KR')\end{aligned} \tag{B11}$$

where

$$\overline{W}_\zeta(K) = \frac{1}{2\pi}\int_0^{2\pi} W_\zeta(K,\ \phi) d\phi \tag{B12}$$

is the power spectrum averaged over the azimuth. Combining Eqs. (B9), (B10), and (B11),

$$\begin{aligned}W_\eta(K)\delta(K-K') &= \langle H(K)H(K')\rangle\\ &= (2\pi)^3 \int K''dK'' \overline{W}_\zeta(K'')\\ &\quad\times \int RdR J_0(KR) J_0(K''R)\\ &\quad\times \int R'dR'\, J_0(K'R') J_0(K''R')\\ &= (2\pi)^3 \int K''dK'' \overline{W}_\zeta(K'')\\ &\quad\times \frac{\delta(K''-K)}{K}\frac{\delta(K''-K')}{K'}\\ &= (2\pi)^3 \frac{\overline{W}_\zeta(K)}{K}\delta(K-K').\end{aligned} \tag{B13}$$

Comparing the two sides of the preceding equation, the desired relation between $W_\zeta(k)$ and $\overline{W}_\eta(k)$ is obtained:

$$W_\eta(K) = (2\pi)^3 \frac{\overline{W}_\zeta(K)}{K}. \tag{B14}$$

To generate numerical realizations of the azimuthally summed random surface, the second equation in Eq. (B8) must be converted to discrete form. To that end, define the following discrete distribution within a bin of wavenumber:

$$h(K) = \int_K^{K+\Delta K} dK' H(K'). \tag{B15}$$

From Eq. (B9),

$$\begin{aligned}\langle h^2(K)\rangle &= \int_K^{K+\Delta K} dK' \int_K^{K+\Delta K} dK'' \langle H(K')H(K'')\rangle\\ &= \int_K^{K+\Delta K} dK' \int_K^{K+\Delta K} dK'' W_\eta(K')\delta(K'-K'')\\ &= W_\eta(K)\Delta K.\end{aligned} \tag{B16}$$

Let

$$h(K) = \sqrt{W_\eta(K)\Delta K}\, N(0,1). \tag{B17}$$

Then a realization can be generated by the following digitized version of the first equation of (B8):

$$\eta(R) = \sum_n h(K_n) K_n J_0(K_n R), \tag{B18}$$

where $K_n = n\Delta K$, $n = 0,\ 1,\ 2,\ \ldots$. Let the maximum range of the surface be $L/2$, and $\Delta K L = 2\pi$,

$$\begin{aligned}\eta(m\Delta R) &= \sum_{n=0}^{N-1} h(K_n) K_n J_0(K_n m\Delta R)\\ &= (2\pi)^2 \sum_{n=0}^{N-1} \sqrt{\frac{\overline{W}_\zeta(n\Delta K)(n\Delta K)}{L}}\, J_0(mn\Delta K\Delta R) R_{1n}\end{aligned} \tag{B19}$$

Author's complimentary copy

where $R_{1n} = N(0, 1)$, and Eq. (B14) has been used to express the realization using $\overline{W}_\zeta$. To estimate the power spectrum from realizations of rough surfaces, use:

$$W_\eta(K) = \frac{\langle h^2(K)\rangle}{\Delta K} \approx \langle H^2(K)\rangle \Delta K = \frac{2\pi}{L}\langle H^2(K)\rangle = \frac{2\pi}{L}\left\langle \left| \int_0^\infty R dR\, \eta(R) J_0(KR) \right|^2 \right\rangle. \quad \text{(B20)}$$

APPENDIX C: CALCULATING BACKSCATTERING STRENGTH

When an ensemble of backscattered time series $p_s(t)$ is obtained either from measurement or from simulation, the backscattering cross section is calculated according to the definition:

$$\sigma(\theta) = \frac{\left\langle |p_s(t)|^2 \right\rangle r^4}{\int I_0 dA}, \quad \text{(C1)}$$

where $I_0(t)$ is the incident intensity at a unit distance from the source and $dA = 2\pi R dR$ is the ensonified area, where R is the horizontal range. The same expression also applies for the slant range, r, $dA = 2\pi r dr$. It is assumed that the source has no azimuthal directivity. The average denoted by $\langle\rangle$ is over a finite sample of realizations, unlike the infinite ensemble employed in Appendix B. Because $r = c_1 t/2$, $dr = c_1 dt/2$ and $\int I_0(t) dt = E$ is the source energy,

$$\sigma(\theta) = \frac{\left\langle |p_s(t)|^2 \right\rangle r^4}{\pi r E} = \frac{\left\langle |p_s(t)|^2 \right\rangle (c_1 t)^3}{8\pi c_1 E}. \quad \text{(C2)}$$

APPENDIX D: BACKSCATTERING STRENGTH IN PERTURBATION THEORY

It will be shown that eq. (10) leads to a backscattering cross section expression that is the same as given by first-order perturbation theory. First, rewrite Eq. (10) in its two-dimensional form

$$p_s(z_0) = \frac{k_1^2}{2\pi} \int_{-\infty}^{\infty}\int_{-\infty}^{\infty} dx' dy' \varsigma(x', y') \frac{e^{2ik_1 r'}}{r'} \tau(R'). \quad \text{(D1)}$$

Assume that the rough patch of area A is centered at (x_c, y_c). Then

$$k_1 r' \approx k_1 r_c + \delta\mathbf{R} \cdot \delta\mathbf{K}, \quad \text{(D2)}$$

where $r_c = \sqrt{x_c^2 + y_c^2 + z_0^2}$, $\delta\mathbf{R} = (x' - x_c, y' - y_c) = \mathbf{R}' - \mathbf{R}_c$, $\delta\mathbf{K} = (k_1 \cos\theta_c \cos\phi_c, k_1 \cos\theta_c \sin\phi_c)$, $\sin\theta_c = z_0/r_c$, and $\cos\phi_c = (x' - x_c)/|\delta\mathbf{R}|$. Then the mean scatterered intensity is approximately

$$\begin{aligned}\left\langle |p_s(z_0)|^2 \right\rangle &\approx \frac{k_1^4}{(2\pi)^2} \int_{-\infty}^{\infty}\int_{-\infty}^{\infty} dx' dy' \int_{-\infty}^{\infty}\int_{-\infty}^{\infty} dx'' dy'' \langle \zeta(x', y')\zeta(x'', y'')\rangle \frac{e^{2ik_1(r' - r'')}}{r_c^2} |\tau(R_c)|^2 \\ &= \frac{k_1^4}{r_c^2} |\tau(R_c)|^2 dA \frac{1}{(2\pi)^2} \int_{-\infty}^{\infty}\int_{-\infty}^{\infty} d(x' - x'') d(y' - y'') N(x' - x'', y' - y'') e^{2i[\delta\mathbf{K}\cdot(\mathbf{R}' - \mathbf{R}'')]} \\ &= \frac{k_1^4}{r_c^2} |\tau(R_c)|^2 dA W(2\delta\mathbf{K}), \end{aligned} \quad \text{(D3)}$$

where N is the two-dimensional correlation function and W its power spectrum. According to the definition of Appendix C, the backscattering cross section is

$$\sigma(\theta) = \left\langle |p_s(z_0)|^2 \right\rangle r_c^2/dA = k_1^4 |\tau(R_c)|^2 W(2k_1 \cos\theta_c \cos\phi_c, 2k_1 \cos\theta_c \sin\phi_c), \quad \text{(D4)}$$

in agreement with the usual expression[21] (Chap. 13).

[1] M. J. Isakson and N. P. Chotiros, "Finite element modeling of reverberation and transmission loss in shallow water waveguides with rough boundaries," J. Acoust. Soc. Am. **129**, 1273–1279 (2011).
[2] H. Bucker and H. Morris, "Normal-mode reverberation in channels or ducts," J. Acoust. Soc. Am. **44**, 827–828 (1968).
[3] J. X. Zhou, D. H. Guan, E. C. Shang, and E. S. Luo, "Long-range reverberation and bottom scattering strength in shallow water," Chin. J. Acoust. **1**, 54–63 (1982).
[4] R. H. Zhang and G. L. Jin, "Normal mode theory of average reverberation intensity in shallow-water," J. Sound Vib. **119**, 215–223 (1987).
[5] E. C. Shang, "Some new challenges in shallow water acoustics," in *Progress in Underwater Acoustics*, edited by H. M. Merklinger (Plenum, New York, 1987), pp. 461–472.
[6] D. D. Ellis, "A shallow-water normal mode reverberation model," J. Acoust. Soc. Am. **97**, 2804–2814 (1995).
[7] W. A. Kuperman and H. Schmidt, "Self-consistent perturbation approach to rough surface scattering in stratified elastic media," J. Acoust. Soc. Am. **86**, 1511–1522 (1989).
[8] K. Lepage, "Bottom reverberation in shallow water: Coherent properties as a function of bandwidth, waveguide characteristics, and scatterer distributions," J. Acoust. Soc. Am. **106**, 3240–3254 (1999).
[9] J. Yang, D. Tang, and E. I. Thorsos, "Reverberation due to bottom roughness using first-order perturbation theory," in *Proceedings of the International Symposium on Underwater Reverberation and Clutter* (2008), pp. 81–88.
[10] E. C. Shang, T. F. Gao, and J. R. Wu, "A shallow-water reverberation model based on perturbation theory," IEEE J. Ocean. Eng. **33**, 451–461 (2008).
[11] B. H. Tracey and H. Schmidt, "A self-consistent theory for seabed volume scatter," J. Acoust. Soc. Am. **106**, 2524–2534 (1999).

Author's complimentary copy

[12]M. B. Porter and E. L. Reiss, "A numerical method for ocean acoustic normal modes," J. Acoust. Soc. Am. **76**, 244–252 (1984).
[13]H. Schmidt and F. Jensen, "A full wave solution for propagation in multilayered viscoelastic media with application to Gaussian beam reflection at fluid-solid interfaces," J. Acoust. Soc. Am. **77**, 813–825 (1985).
[14]H. Weinberg and R. Keenan, "Gaussian ray bundles for modeling high-frequency propagation loss under shallow-water conditions," J. Acoust. Soc. Am. **100**, 1421–1431 (1996).
[15]D. E. Weston, "Acoustic flux formulas for range-dependent ocean duct," J. Acoust. Soc. Am. **68**, 261–281 (1980).
[16]D. E. Weston, "Acoustic flux methods for oceanic guided waves," J. Acoust. Soc. Am. **68**, 287–296 (1980).
[17]C. H. Harrison, "Closed-form expressions for ocean reverberation and signal excess with mode-stripping and Lambert's law," J. Acoust. Soc. Am. **114**, 2744–2756 (2003).
[18]C. W. Holland, "Reverberation and clutter from sub-bottom mechanisms," in *Proceedings of the International Symposium on Underwater Reverberation and Clutter* (2008), pp. 113–121.
[19]E. I. Thorsos and D. R. Jackson, "The validity of the perturbation approximation for rough surface scattering using a Gaussian roughness spectrum," J. Acoust. Soc. Am. **86**, 261–277 (1989).
[20]E. I. Thorsos, "Acoustic scattering from a Pierson-Moskowitz sea surface," J. Acoust. Soc. Am. **88**, 335–349 (1990).
[21]D. Jackson and M. Richardson, *High-Frequency Seafloor Acoustics* (Springer, New York, 2007), Chap. 6, pp. 171–200; Chap. 8, p. 263; Chap. 13, pp. 332–341.
[22]R. B. Evans, "A coupled mode solution for acoustic propagation in a waveguide with stepwise depth variations of a penetrable bottom," J. Acoust. Soc. Am. **74**, 188–2195 (1983).
[23]A. T. Abawi and M. B. Porter, "Propagation in an elastic wedge using the virtual source technique," J. Acoust. Soc. Am. **121**, 1374–1382 (2007).
[24]B. F. Kur'yanov, "The scattering of sound at a rough surface with two types of irregularities," Sov. Phys. Acoust. **8**, 252–257 (1963).
[25]S. McDaniel and A. D. Gorman, "An examination of the composite-roughness scattering model," J. Acoust. Soc. Am. **73**, 1476–1486 (1983).
[26]D. R. Jackson, D. P. Winebrenner, and A. Ishimaru, "Application of the composite roughness model to high-frequency bottom backscattering," J. Acoust. Soc. Am. **79**, 1410–1422 (1986).
[27]J. F. Lingevitch and K. D. LePage, "Parabolic equation simulations of reverberation statistics from non-Gaussian-distributed bottom roughness," IEEE J. Ocean. Eng. **35**, 199–208 (2010).
[28]A. Ivakin, "A unified approach to volume and roughness scattering," J. Acoust. Soc. Am. **103**, 827–837 (1998).
[29]E. Thorsos, D. R. Jackson, and K. L. Williams, "Modeling of subcritical penetration into sediments due to interface roughness," J. Acoust. Soc. Am. **107**, 263–277 (2000).
[30]D. Li, G. V. Frisk, and D. Tang, "Modeling of bottom backscattering from three-dimensional volume inhomogeneities and comparisons with experimental data," J. Acoust. Soc. Am. **109**, 1384–1397 (2001).
[31]L. M. Brekhovskikh and O. A. Godin, *Acoustics of Layered Media II, Point Sources and Bounded Beams* (Springer-Verlag, Berlin, 1999), pp. 1–38.
[32]M. Collins, "A split-step Padé solution for the parabolic equation method," J. Acoust. Soc. Am. **93**, 1736–1742 (1993).
[33]E. I. Thorsos and J. Perkins, "Overview of the reverberation modeling workshops," in *Proceedings of the International Symposium on Underwater Reverberation and Clutter* (2008), pp. 3–22.
[34]F. B. Jensen, "On the use of stair steps to approximate bathymetry changes in ocean acoustic models," J. Acoust. Soc. Am. **104**, 1310–1315 (1998).

Author's complimentary copy

Mid-frequency geoacoustic inversion using bottom loss data from the Shallow Water 2006 Experiment

Jie Yang,[a] Darrell R. Jackson, and Dajun Tang
Applied Physics Laboratory, University of Washington, 1013 NE 40th Street, Seattle, Washington 98105-6698

(Received 31 January 2011; revised 21 July 2011; accepted 4 August 2011)

Geoacoustic inversion work has typically been carried out at frequencies below 1 kHz, assuming flat, horizontally stratified bottom models. Despite the relevance to Navy sonar systems many of which operate at mid-frequencies (1–10 kHz), limited inversion work has been carried out in this frequency band. This paper is an effort to demonstrate the viability of geoacoustic inversion using bottom loss data between 2 and 5 kHz. The acoustic measurements were taken during the Shallow Water 2006 Experiment off the coast of New Jersey. A half-space bottom model, with three parameters density, compressional wave speed, and attenuation, was used for inversion by fitting the model to data in the least-square sense. Inverted sediment sound speed and attenuation were compared with direct measurements and with inversion results using different techniques carried out in SW06. Inverted results of the present work are consistent with other measurements, considering the known spatial variability in this area. The observations and modeling results demonstrate that forward scattering from topographical changes is important at mid-frequencies and should be taken into account in sound propagation predictions and geoacoustic inversion. To cope with fine-scale topographic variability, measurement technique such as averaging over tracks may be necessary. © *2012 Acoustical Society of America*. [DOI: 10.1121/1.3666009]

PACS number(s): 43.30.Pc, 43.30.Ma, 43.30.Hw [NPC] Pages: 1711–1721

I. INTRODUCTION

Sediment geoacoustic parameters, in many cases, are the most important parameters for predicting shallow water sound propagation and reverberation. Due to the difficulty of *in situ* measurements, indirect methods have been commonly used to invert for sediment geoacoustic parameters. Among various geoacoustic inversion techniques, bottom reflection/loss measurements have been used to extract sediment geoacoustic properties.

Since the 1960 s, studies on bottom reflection have been carried out[1–3] to understand the interaction between sound and the ocean bottom. Comparisons have been made between measured values of reflection coefficients (or bottom loss) and plane wave reflection coefficients with the bottom modeled as a layered-fluid medium.[1–6] A greater part of these studies were at low frequencies, i.e., below 1 kHz,[1,4–6] with considerable acoustic energy penetrating the bottom. This results in additional complexity in interpreting bottom reflection measurements if bottom properties vary significantly with depth. Such is the case with a so-called transition layer where bottom properties vary linearly with depth. Due to the sound speed gradient, energy refracted within the bottom can be significant in modeling bottom loss (BL) data at low frequencies.[4–6] Analytic solutions have been derived for the reflection of plane acoustic waves from horizontally stratified fluid layer whose density and sound speed vary linearly with depth.[7–9]

As to geoacoustic inversion using bottom reflection, some of the published work focused on estimating sediment properties within a transition layer, i.e., to invert for gradients of sound speed or attenuation within the layer. Using a fluid bottom, Spofford[10] proposed a technique to estimate the sound speed gradient using acoustic data between 50–1600 Hz. Holland *et al.*[11] demonstrated a method to obtain density and sound speed gradients in the transition layer (top 1.5 m) by a Bayesian inversion approach in the frequency band of 300–1600 Hz. Many inversion models assume discrete layering. A unique inversion scheme was presented by Holland *et al.*[12] based on a joint time- and frequency-domain data analysis using wideband signals between 600 and 6000 Hz. The time-domain BL data were used to obtain layer thicknesses and interval velocities, whereas the frequency-domain data were used to determine depth- and frequency-dependent attenuation and depth-dependent density. In addition, geoacoustic inversion using BL data was studied where the sediment was modeled as an elastic[13] or poro-elastic[14,15] medium. Since a fluid bottom is adopted in the present work, the details of the elastic and poro-elastic models will not be addressed here.

As noted above, geoacoustic inversion work has typically been carried out at low frequencies. Despite the relevance to Navy sonar systems, many of which operate at mid-frequencies (1–10 kHz), limited inversion work has been carried out in this frequency band where sound propagation and reverberation can be strongly influenced by variability in the sea bottom, surface, and water column. This paper is an effort to demonstrate the viability of geoacoustic inversion using bottom loss data at mid-frequencies (2–5 kHz). The acoustic data presented in this work were taken during the Shallow Water 2006 Experiment (SW06) off the coast of New Jersey.[16] As one of the mid-frequency efforts in SW06, the acoustic measurement was conducted in the central area

[a]Author to whom correspondence should be addressed. Electronic mail: jieyang@apl.washington.edu

Downloaded 27 Feb 2012 to 128.95.76.55. Redistribution subject to ASA license or copyright; see http://asadl.org/journals/doc/ASALIB-home/info/terms.jsp

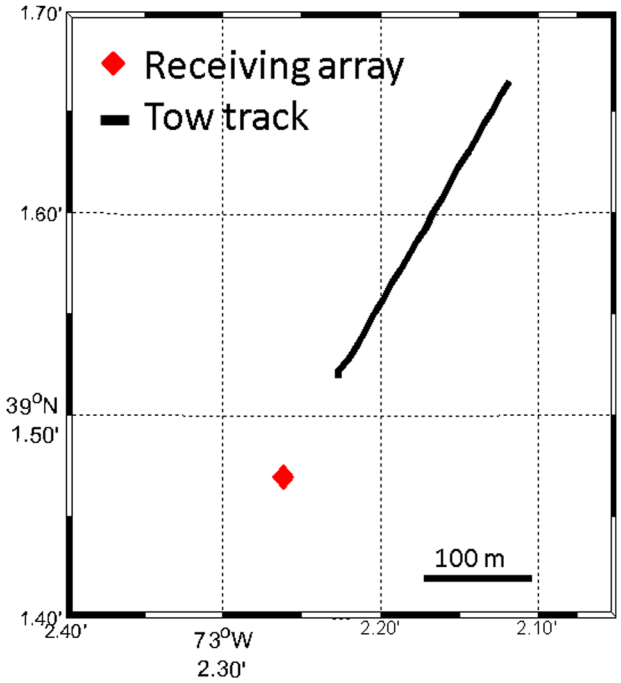

FIG. 1. (Color online) GPS locations of acoustic measurements. Diamond: moored receiving array; black line: acoustic track with a towed source.

of SW06 (location shown in Fig. 1). During SW06, many acoustic measurements were carried out in this area, and one of the main goals is to improve inversion technique by comparing geoacoustic inversion results using different methods with supporting ground truth measurements. The ground truth measurements include several earlier experiments and a geological survey conducted on mid and outer New Jersey shelf to characterize the seabed[17–21] and *in situ* measurements in SW06.[22–24] We demonstrate that it is possible to use mid-frequency data to successfully estimate sediment sound speed; however, it is also found that care needs to be taken to minimize the impact of fine-scale topographical variation.

This paper is organized as follows. In Sec. II, the acoustic data and results are presented, and the bottom modeling and geoacoustic inversions results are shown in Sec. III. Section IV summarizes the main results and discusses the implications of this work.

II. ACOUSTIC DATA AND RESULTS

The acoustic data involved in this analysis were obtained along a track with a slowly towed source. Data were taken on August 19, 2006 during the SW06 experiment and recorded on a receiving array moored at 39° 01.47′ N, 73° 02.26′ W. On the receiving array, there are two subarrays, clustered at depths 25 and 50 m below the surface, and each has four elements. For the sub-array at 25 m, the four elements are at 25.0, 25.2, 25.5, and 26.4 m; for the one at 50 m, the four elements are at 50.0, 50.2, 50.5, and 51.4 m. Linear-frequency-modulated (LFM) chirp signals in the frequency band of 1.5–10.5 kHz were transmitted using an ITC-2015 acoustic source (International Transducer Company) with 10% cosine taper at the beginning and end of the chirp. The focus of this work is on data received at 25 m.

A. Tow data

The acoustic data were taken on August 19, 00:29:00–00:49:00 UTC. The source was towed by the R/V Knorr at a speed of 0.5 knot along an 80 m isobath, and LFM signals were transmitted every 20 s with a source depth of 40 m. The tow started at a range of 105 m and ended at approximately 8 km. The data shown in this work correspond to the beginning part of the tow, i.e., from 105 m to 400 m (Fig. 1). There are a total of 60 pings during this tow interval.

The signals received at 25 m were first pulse-compressed in the frequency band of 1.5–6 kHz. In Fig. 2, the compressed signals for the 25 m receiver are plotted against the ping number on the vertical axis and the reduced travel time on the horizontal axis with a time equal to propagation time for 1495 m/s at the range between the source and receiving array for each ping removed. The first three arrivals were identified as direct arrival, surface and bottom reflections. Since our goal is to study bottom loss, the focus will be on the bottom reflection. As shown in Fig. 2(b), all bottom bounces were aligned at time zero and cut with a 2.5 ms time window. The time series were carefully examined and there was no evidence of secondary reflectors in the bottom reflection signal. The 60 pings shown here correspond to grazing angles from 10° to approximately 43°.

To obtain BL, a sensitivity calibration is needed, and the source beam pattern has to be taken into account. Here, the direct path of the tow data will be used for calibration. The advantage of using the direct path can be seen from Fig. 3 which shows the sound speed profile on the left and geometry of acoustic measurements on the right. When towed at a constant speed, the source was tilted and this tilt angle, θ, is the same for both the direct path and the bottom bounce path. This will simplify beam pattern correction due to the tilt. In Fig. 3, r_0 is the distance between the ship stern and the receiving array obtained from GPS and ship gyro recordings; r_1 is the propagation distance for the bottom bounce, obtained from arrival time. Using the geometry shown in Fig. 3, the tilt angle can be computed via

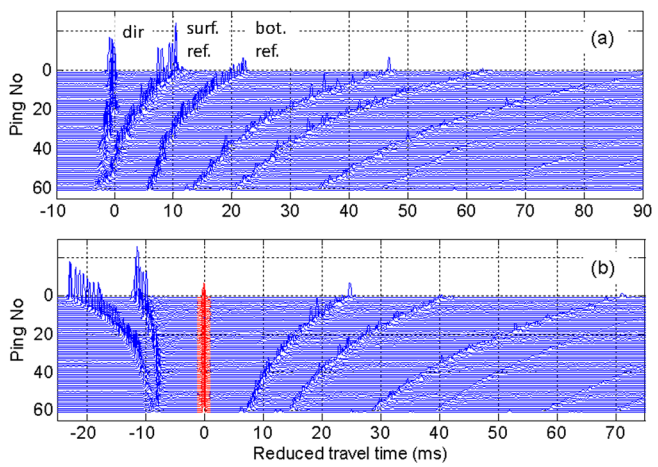

FIG. 2. (Color online) (a) Pulse compressed results for 60 pings with reduced travel time (see definition in text) in the frequency band of 1.5–6 kHz; (b) same data with the bottom bounce lined up at time zero.

Downloaded 27 Feb 2012 to 128.95.76.55. Redistribution subject to ASA license or copyright; see http://asadl.org/journals/doc/ASALIB-home/info/terms.jsp

$$\begin{cases} 2H - Z_r = Z_s \cos\theta + \sqrt{r_1^2 - y^2} \\ y + Z_s \sin\theta = r_0 \end{cases}, \quad (1)$$

where Z_r is the receiver depth, Z_s is the distance from the ship stern to the source, and H is the water depth. It is assumed that the tow line is straight, that is, that the effect of drag on the tow line is negligible compared to the effect of the tension force exerted by the source. The tilt angle obtained from Eq. (1) for each ping falls in the angle range of $1.5° \pm 0.5°$ throughout the acoustic measurements. Consequently, a constant value of 1.5° was applied throughout the tow.

As mentioned, direct path data will be used to calibrate the bottom bounce. Similarly to the bottom bounces, the first 19 direct-path signals were lined up and cut with a 2.5 ms time window. Figure 4 shows their receive levels which were corrected for spreading and the source beam pattern (see Sec. II B) at 2, 3, 4, and 5 kHz. Transmissions corresponding to the shortest ranges (at highest grazing angles) appear on the right-hand side of the plot. The receive levels of the first 7 pings, corresponding to a grazing angle range of 10.7°–9.6°, are relatively stable with variation ±0.5 dB. For pings further down range, i.e., at smaller grazing angles, the intensity variation can be up to 5 dB. This is due to the fact that the direct path straddles the thermocline and slight changes in the water column can have significant effects on this path even at a propagation distance of approximately 150 m (Ref. 25). The first 7 pings were used to obtain an average to calibrate all bottom bounce signals. The average signal was obtained by first lining up the 7 pings and taking a coherent average.

B. Source beam pattern

To obtain BL, it is critical to correct both the direct path and the bottom bounce path for the source beam pattern. Factors that affect the beam pattern correction, such as the source tilt and azimuthal rotation, have been carefully examined. Three-dimensional beam pattern measurements at 2, 3, 4, and 5 kHz were carried out at the APL dockside calibration facility. Results shown in Fig. 5 are vertical beam patterns at one

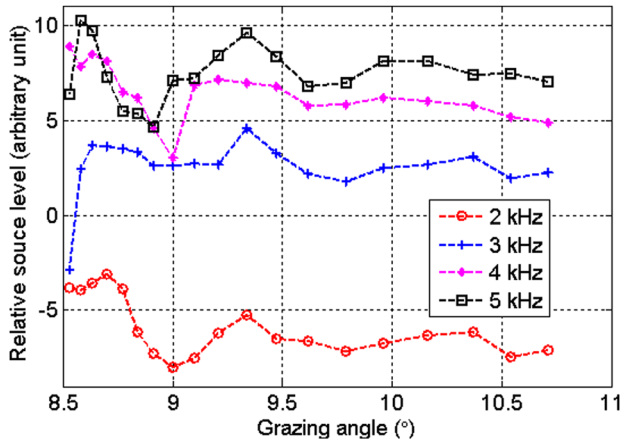

FIG. 4. (Color online) Direct path intensity corrected for spreading and the source beam pattern at 2, 3, 4, and 5 kHz (pings 1–19 have decreasing grazing angles).

of the several azimuth angles in the measurement set with the source sitting upright. Specifically, the figure shows the beam pattern at the azimuth angle which faces the receiver under hydrodynamic considerations of the experimental setup. The direct path from the source to the receiver at 25 m depth corresponds to the angular range of 272°–281° in the beam patterns. Figure 5 shows considerable anti-symmetry in the vertical, i.e., top versus bottom, due to a user-installed suspension system at the bottom of the source. The 3-D beam pattern data will be used in identifying the beam pattern uncertainty due to azimuthal rotation of the source.

C. Bottom loss

Bottom loss can be obtained via

$$\mathrm{BL} = 10 \times \log_{10}\left(\frac{I_0(\chi_0)S_0(\chi_0)/D(\chi_0 - \theta)}{I_i(\chi_i)S_i(\chi_i)/D(\chi_i + \theta)}\right), \quad (2)$$

where $I_0(\chi_0)$ and $I_i(\chi_i)$ are intensities of the calibration and the ith ping; $S_0(\chi_0)$ and $S_i(\chi_i)$ are corresponding spreading losses obtained through ray tracing; and $D(\chi_0 - \theta)$ and

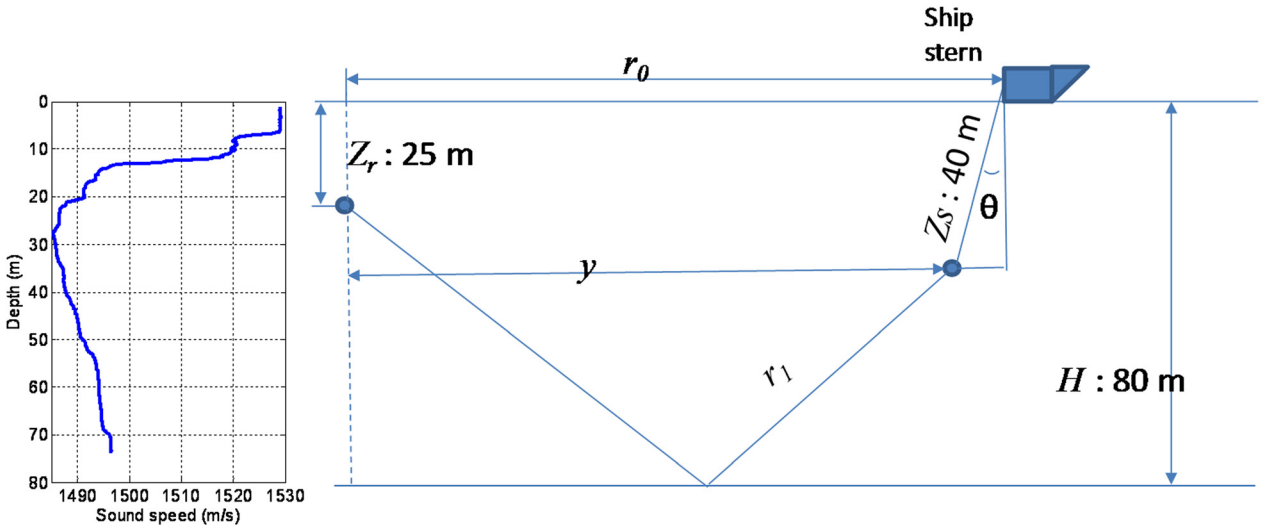

FIG. 3. (Color online) (left) Sound speed profile for the tow; (right) geometry for the towed source data.

Downloaded 27 Feb 2012 to 128.95.76.55. Redistribution subject to ASA license or copyright; see http://asadl.org/journals/doc/ASALIB-home/info/terms.jsp

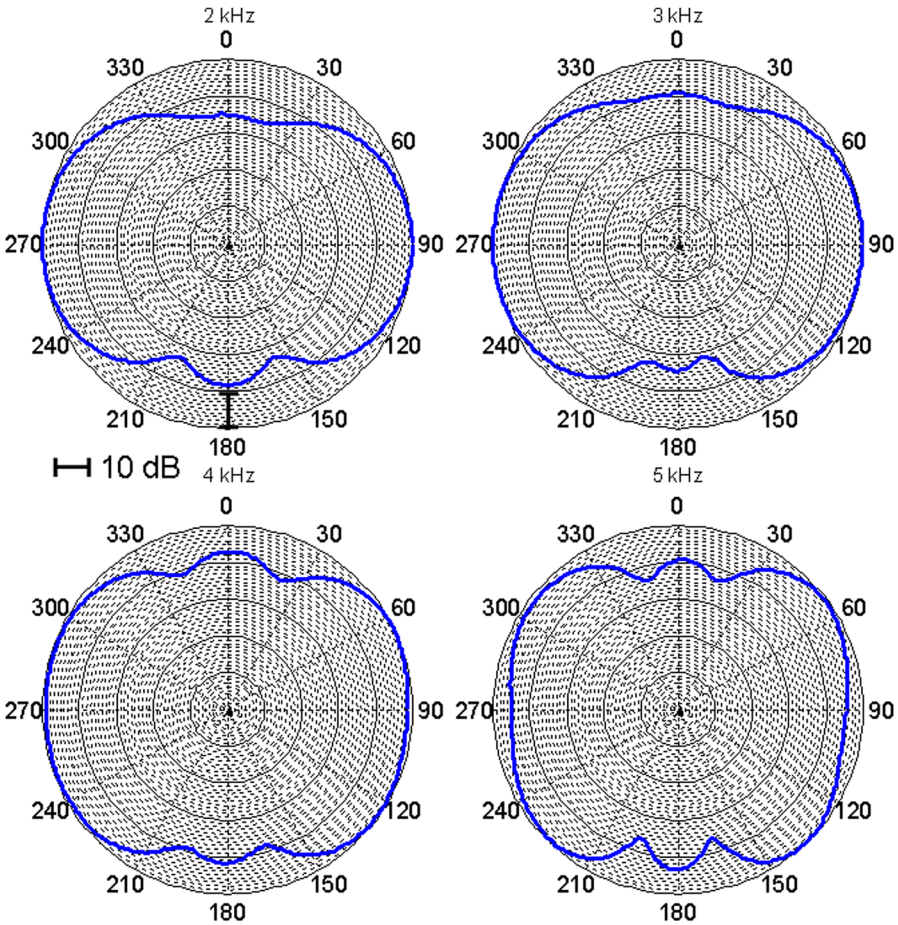

FIG. 5. (Color online) Measured source beam pattern at 2, 3, 4, and 5 kHz at one azimuth angle with source sitting upright. The direct path from the source to the receiver at 25 m depth corresponds to the angular range of 272°–281°.

$D(\chi_i + \theta)$ are source beam pattern corrections with tilt angle taken into account. Both χ_0 and χ_i are launch angles for calibration and BL measurement, respectively.

BL results at four frequencies, 2, 3, 4, and 5 kHz, are shown in Fig. 6 for a 10% bandwidth. Results at different frequencies are quite close to each other, and the critical angle is well defined (around 25° for all frequencies). The result at 2 kHz for grazing angles above 35° is about 2 dB lower than the other three, which is due to insufficient water depth in the beam pattern measurements leading to a problem with multipathing. In addition, all four curves show a feature around 20°. Modeling work was carried out to understand the feature and possible explanations involve local variations in (1) sediment properties; (2) bottom layering; and (3) topography. The modeling results will be shown in Sec. III together with the inversion results.

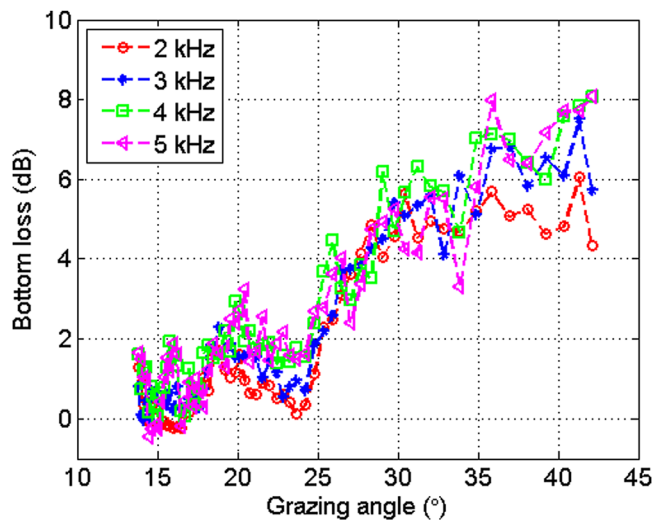

FIG. 6. (Color online) Bottom loss results at 2, 3, 4, and 5 kHz with a 10% bandwidth.

D. Uncertainties in BL data

Consider a general case with measurement variable Y where Y is a function of j variables:

$$Y = Y(X_1, X_2, ..., X_j).$$

Then the uncertainty of measurement variable Y can be written as[26]

$$U_Y = \left[\left(\frac{\partial Y}{\partial X_1} U_{X_1} \right)^2 + \left(\frac{\partial Y}{\partial X_2} U_{X_2} \right)^2 + \cdots + \left(\frac{\partial Y}{\partial X_j} U_{X_j} \right)^2 \right]^{1/2}, \tag{3}$$

where U_{X_i} is the uncertainty for the ith variable, and where the errors in each variable are assumed to be independent.

Following (3), we can write the uncertainty for BL:

$$U_{\mathrm{BL}}^2 = U_{I_0}^2 + U_{S_0}^2 + U_{D(\theta_0)}^2 + U_S^2 + U_{D(\theta)}^2. \tag{4}$$

$U_{I_0}^2$ is the uncertainty of the direct path intensity. Recall that the direct paths of the first seven pings have been used to

Downloaded 27 Feb 2012 to 128.95.76.55. Redistribution subject to ASA license or copyright; see http://asadl.org/journals/doc/ASALIB-home/info/terms.jsp

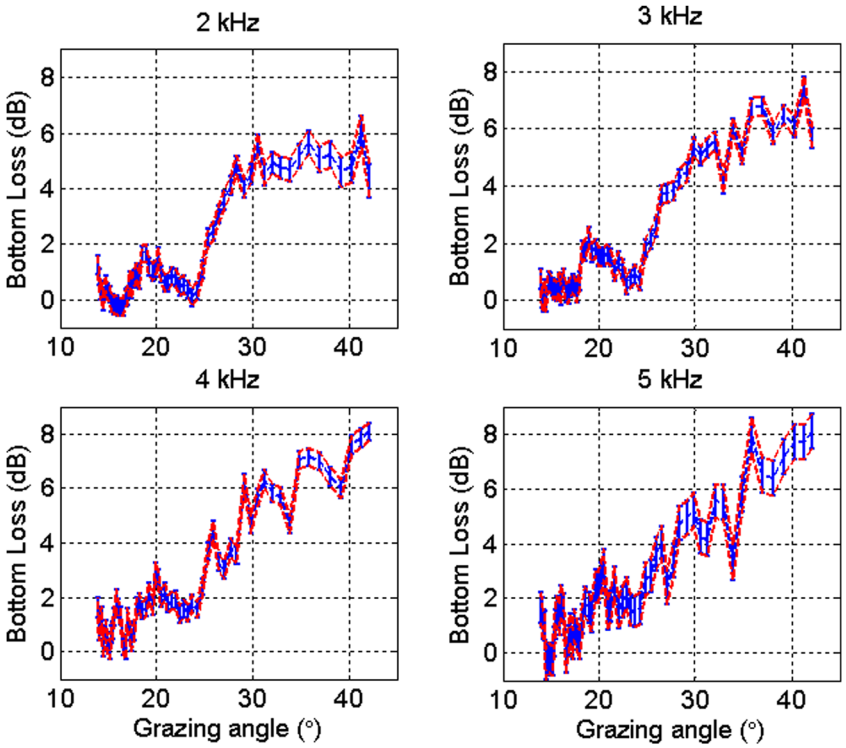

FIG. 7. (Color online) Bottom loss results with uncertainty bounds at 2, 3, 4, and 5 kHz.

find an average signal for calibration, therefore, $U_{I_0}^2$ is taken as the variance of the intensity of the first seven pings.

$U_{S_0}^2$ and U_S^2 are uncertainties of the spreading loss for the direct and bottom-bounce paths modeled by ray tracing due to limited knowledge of the environment. Since the source was towed and the receiving array did not have oceanographic sensors, an oceanographic mooring, approximately 1.5 km away from the receiving array, was used to provide sound speed profiles for modeling. There are 10 sensors on the mooring and the sampling interval is 30 s (sensor depths: 13.3, 15.1, 18.8, 22.6, 26.3, 33.8, 41.3, 56.3, 71.3, 78.5 m). The 60 pings were recorded between 00:29:00 and 00:49:00 UTC on August 19. Within the 20-min recording time, there were a total of 39 profiles recorded by the oceanographic mooring. Since the environmental measurement was not done along the acoustic track, the question now is, how much error is incurred in modeling spreading loss if different sound speed profiles are used? Individual profiles are used to model the intensity of both the direct paths and bottom bounces. At each frequency, six cases have been tried using individual profiles No. 5, 10, 15, 20, 30, and a 20-min average profile. $U_{S_0}^2$ and U_S^2 are defined as the standard deviations of the results (not shown here) from these six cases.

For beam pattern uncertainties, $U_{D(\theta_0)}^2$ and $U_{D(\theta)}^2$, each have three components. The three components are source tilt angle uncertainty due to variations in acoustically determined values, tilt angle uncertainty due to GPS resolution, and source azimuthal-rotation-induced uncertainty. The tilt angle computed using propagation distances varies between $1.5 \pm 0.5°$ and the 0.5° uncertainty in tilt angle was translated into uncertainty using beam pattern data. As shown earlier, GPS recordings were used to find distances between the source and receiver to compute the tilt angle. In this experiment, GPS has a ± 0.5 m resolution which adds extra tilt angle uncertainty which can be similarly converted into uncertainty using beam pattern data. For source rotation induced uncertainty, it was assumed that the source can rotate $\pm 90°$. Three-dimensional beam pattern data were used to provide uncertainty due to the rotation.

With all the uncertainties identified, the BL results are re-plotted in Fig. 7 at 2, 3, 4, and 5 kHz with uncertainty bars. The uncertainties at 3 and 4 kHz are smaller than those at 2 and 5 kHz, which is due to the fact that uncertainty in beam pattern correction dominates. In addition, the uncertainty bound itself is smaller than the BL fluctuations. We consider these fluctuations may be real and possibly due to forward scattering from topographical variation.[27] To take out the fluctuations, one would need to repeat acoustic measurements over multiple tracks and do ensemble averaging.

III. BOTTOM MODELING AND GEOACOUSTIC INVERSION

A simple half space bottom model, with three parameters, density, compressional wave speed, and attenuation, was used for geoacoustic inversion by best matching model with data in the least square sense. The choice of a half-space over a layered bottom model, which was also investigated but not shown here, is based on the fact that little frequency dependence was observed in BL measurements (Fig. 6). One expects frequency-dependent interference with a layered bottom, therefore, a half-space model is appropriate for the present work. In addition, BL obtained with a flat, plane wave model was used to compare with data for inversion. Considering the receiver depth above the water/sediment interface (55 m) relative to the wavelength (0.75 m), the approximation of geometrical acoustics is satisfied and the plane-wave reflection coefficient can be used.[28] Inverted

Downloaded 27 Feb 2012 to 128.95.76.55. Redistribution subject to ASA license or copyright; see http://asadl.org/journals/doc/ASALIB-home/info/terms.jsp

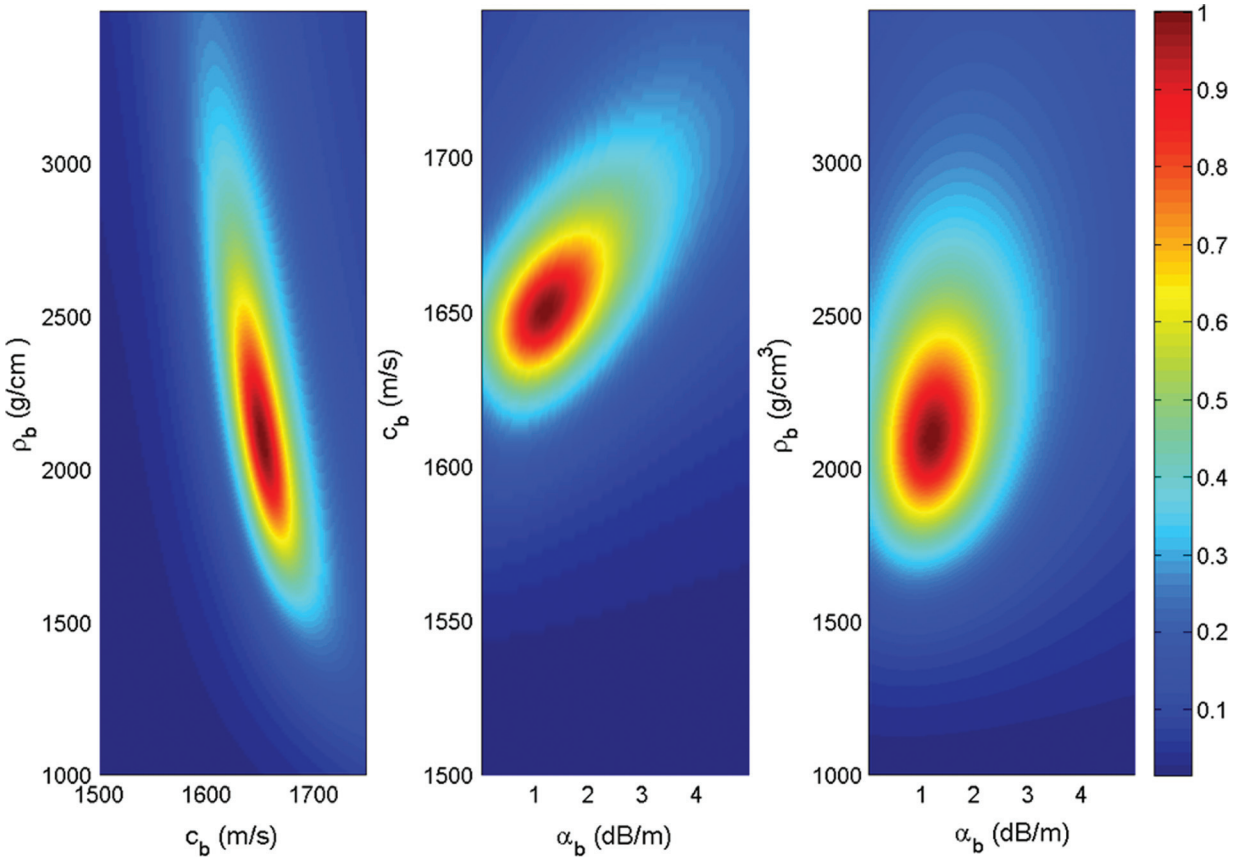

FIG. 8. Cost function surfaces in terms of ρ-c, c-α, and ρ-α through an exhaustive search at 3 kHz.

sediment geoacoustic parameters and their uncertainties are summarized in Sec. III A. Additional modeling work has been carried out in an attempt to understand the interesting feature around 20° in BL. Possible explanations for the feature and modeling results are presented in Sec. III B. Direct measurement should be used as ground truth to validate inversion results. Therefore, in Sec. III C, inverted sediment sound speed results of this work are compared with direct measurements and other inversion results which were carried out within a 2 km × 2 km boxed area.

A. Half-space fluid model

A simple half space bottom model is used with three parameters, density ρ, compressional wave speed c, and attenuation α, and they are allowed to be frequency dependent. An exhaustive search was carried out to estimate the three parameters by best matching model with data in the least square sense. One advantage of doing an exhaustive search is that we can look at correlations between different parameters. The cost function is defined as the squared error between model and data summed over all angles. Figure 8 shows the cost function surfaces in terms of ρ-c, c-α, and ρ-α at 3 kHz, and the red area indicates the most probable region for the inversion results. The correlation between parameters can be clearly seen from Fig. 8: ρ-c has an inverse relation since the product of the two determines acoustic impedance; c and α are slightly correlated;[29] while ρ and α are quite independent of each other, i.e., there is little correlation between the two.

The best fits between data and a half-space model at 2, 3, 4, and 5 kHz are shown in Fig. 9, and the inversion results for ρ, c, and α and their uncertainties are summarized in Fig. 10. The uncertainties were computed as follows.[30] For a linear system of equations $\underline{d} = G\underline{m}$, the least squares solution is

$$\underline{m}_{L_2} = \left(G^T G\right)^{-1} G^T \underline{d}.$$

For a weakly nonlinear problem like the one in this paper, we can expand the problem around the solution point to the first order, and therefore, matrix G can be defined as $G_{ij} = \frac{\partial d_i}{\partial m_j}$. Specifically, for BL with three parameters ρ, c, and α, i.e., $\underline{m} = \begin{bmatrix} \rho \\ c \\ \alpha \end{bmatrix}$, and N data points, G can be written as

$$G = \begin{bmatrix} \frac{\partial BL_1(\underline{m})}{\partial \rho} & \frac{\partial BL_1(\underline{m})}{\partial c} & \frac{\partial BL_1(\underline{m})}{\partial \alpha} \\ \frac{\partial BL_2(\underline{m})}{\partial \rho} & \frac{\partial BL_2(\underline{m})}{\partial c} & \frac{\partial BL_2(\underline{m})}{\partial \alpha} \\ \vdots & \vdots & \vdots \\ \frac{\partial BL_N(\underline{m})}{\partial \rho} & \frac{\partial BL_N(\underline{m})}{\partial c} & \frac{\partial BL_N(\underline{m})}{\partial \alpha} \end{bmatrix}, \quad (5)$$

where $\frac{\partial BL}{\partial x} = 20\log_{10}(e)\mathrm{Re}\left\{R^* \frac{\partial R}{\partial x}\right\} \frac{1}{|R|^2}$ and R is the complex reflection coefficient.

Downloaded 27 Feb 2012 to 128.95.76.55. Redistribution subject to ASA license or copyright; see http://asadl.org/journals/doc/ASALIB-home/info/terms.jsp

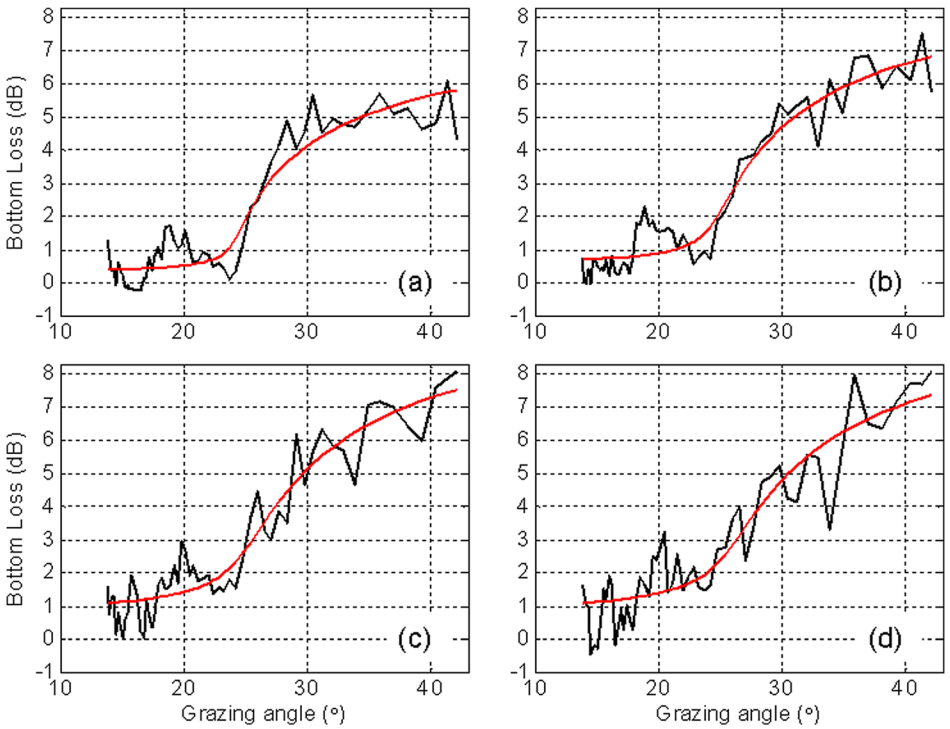

FIG. 9. (Color online) Best match between model and data at (a) 2 kHz, (b) 3 kHz, (c) 4 kHz, (d) 5 kHz including the feature around 20°.

The system of equations is scaled by $W = \mathrm{diag}(1/\sigma_1, 1/\sigma_2, \ldots 1/\sigma_j)$ and the least squares solution is then $\underline{m}_{L_2} = \left(G_w^T G_w\right)^{-1} G_w^T \underline{d}_w$, where $G_w = WG$ and $\underline{d}_w = W\underline{d}$. The covariance of a data vector $\underline{d}$ of normally distributed, independent random variables with linear transformation matrix A is

$$\mathrm{Cov}(A\underline{d}) = A\mathrm{Cov}(d)A^T.$$

With $A = \left(G_w^T G_w\right)^{-1} G_w^T$, the covariance matrix for $\underline{m}_{L_2}$ can be written as

$$\begin{aligned}\mathrm{Cov}\left(\underline{m}_{L_2}\right) &= \left(G_w^T G_w\right)^{-1} G_w^T I G_w \left(G_w^T G_w\right)^{-1} \\ &= \left(G_w^T G_w\right)^{-1}. \end{aligned} \quad (6)$$

The uncertainty is defined as the 95% confidence interval for each model parameter and can be obtained via the covariance matrix:

$$\underline{m}_{L_2} \pm 1.96 \cdot \mathrm{diag}\left(\mathrm{Cov}\left(\underline{m}_{L_2}\right)\right)^{1/2}. \quad (7)$$

Using (7), the uncertainties for ρ, c, and α can be obtained. Figure 10(a) summarizes the inversion results using the entire BL data and Fig. 10(b) using the BL data excluding the feature around 20°. Figure 10 shows that in general, uncertainty increases with frequency for all frequencies. For density and sound speed, the uncertainties are quite small while for attenuation, the uncertainty can sometimes be up to 50%. By comparing Figs. 10(a) and 10(b), it is clear that inverted density and sound speed change little with or without the feature around 20° while attenuation has been greatly reduced. Based on the work of Williams *et al.*,[31] 1% dispersion in sound speed is expected in the frequency band of 2–5 kHz. Dispersion at this level would be masked by uncertainty in sediment sound speed for this work.

As known, BL has different sensitivity to ρ, c, and α at different grazing angles. For grazing angles above the critical, BL is sensitive to density while for those below the critical, BL is sensitive to attenuation. The critical angle depends on sound speed; therefore BL is sensitive to sound speed for angles near critical. As a result, one expects little change in inversion results for ρ and c with or without the feature around 20° while the contrary is expected for attenuation.

B. Possible explanation for feature around 20°

As mentioned in Sec. II, possible explanations for the feature around 20° are local variations in (1) sediment property; (2) interference due to a layered bottom; and (3) topography. For possibility (1), a local soft spot is needed to reproduce the feature. Based on a geological survey on the New Jersey middle and outer shelf,[18] this explanation is unlikely. The 98 grab samples and collocated acoustic measurements using the *In situ* Sound Speed and Attenuation Probe (ISSAP) show that the sediment at the SW06 experimental site is comprised mostly of clayey sands to coarse sands. Specifically for the location of the measurements in this work, the sediment is classified as "ribbons"[18] with a mean grain size between 1 ϕ and 2.5 ϕ with no examples of the very fine-grained sediment, i.e., grain size around 4 ϕ, required to explain the feature.[32] For possibility (2), a model with a layer of finite thickness over a semi-infinite layer was used to invert for local parameters. The model has seven parameters: 2 sets of ρ, c, and α for the finite and semi-infinite layers respectively and a layer thickness. Inversion results (not shown here) yield layer thickness that is inversely proportional to frequency, ruling out the hypothesis of local variation in bottom layering.

To investigate possibility (3), a broadband simulation was carried out to model the experiment using the parabolic

Downloaded 27 Feb 2012 to 128.95.76.55. Redistribution subject to ASA license or copyright; see http://asadl.org/journals/doc/ASALIB-home/info/terms.jsp

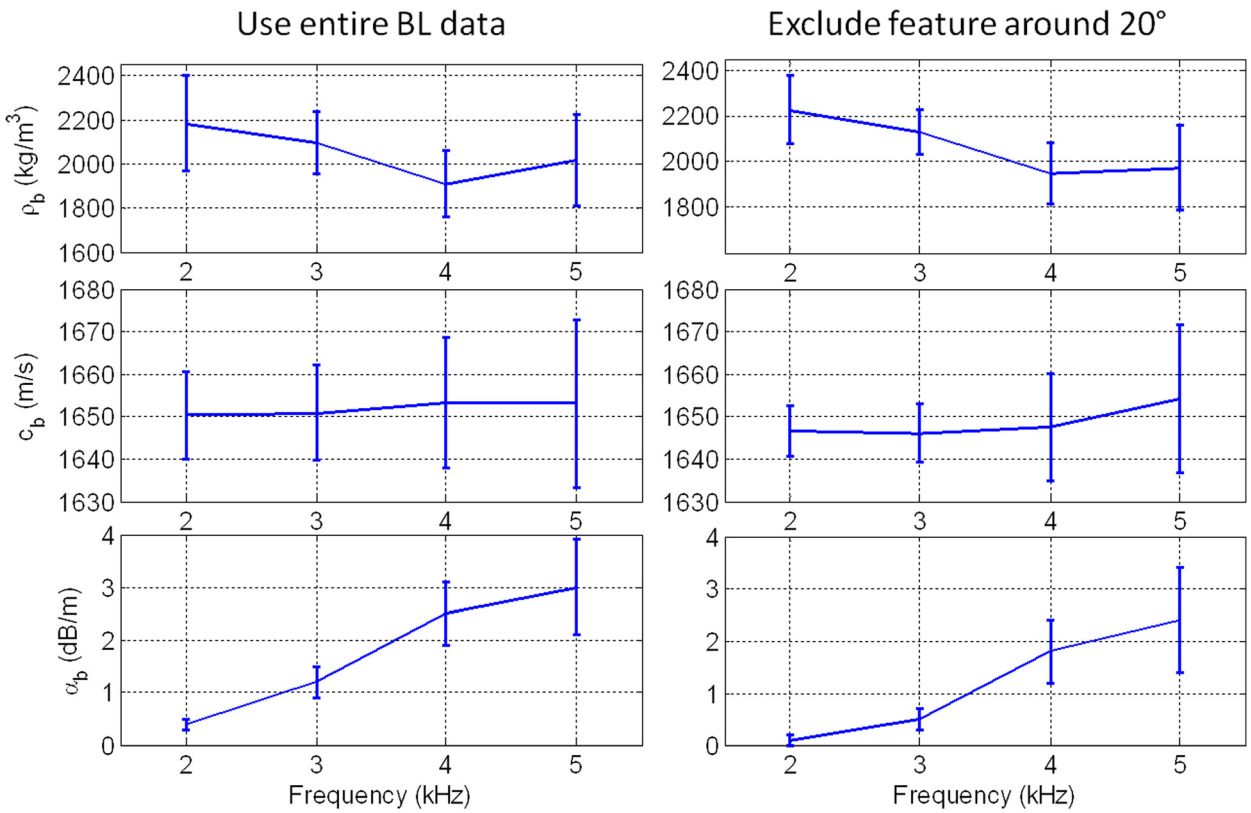

FIG. 10. (Color online) Summary of inversion results for ρ, c, and α (a) using entire BL data and (b) using BL data excluding feature around 20°.

equation (PE) with bathymetry variation. To reproduce the feature, this bathymetry variation was found to span about 50 m resembling a convex surface, and a Gaussian shape is used to represent this bathymetry change. This feature was positioned to cover the range interval of 90–140 m from the source corresponding to grazing angles between 16°–24°. Figure 11(a) shows the simulation results for BL with a flat bottom for reference and Fig. 11(b) with an 8-cm-high Gaussian bottom feature. The simulation results show a BL feature similar to that observed in data, and the width and magnitude match the experiment quite well. The simulation results are surprising in amplitude considering such a gentle topographic change. A simulation using the Kirchhoff approximation was used to check the results obtained from PE. The results from PE and Kirchhoff are in good agreement, demonstrating a maximum 2 dB BL change due to the bottom feature with reference to a flat bottom case. Both PE and Kirchhoff are 2D simulations and no out-of-plane scattering is allowed. In addition, simulation results show that this bottom feature affects acoustics mainly at low grazing angles.

Based on the modeling results, possibility (3) may be the cause for the feature around 20°. The simulation results, however, are unable to reproduce the slight frequency dependence of the feature observed in data (Fig. 6) due to the fact that it was hypothesized as a geometrical lensing effect.

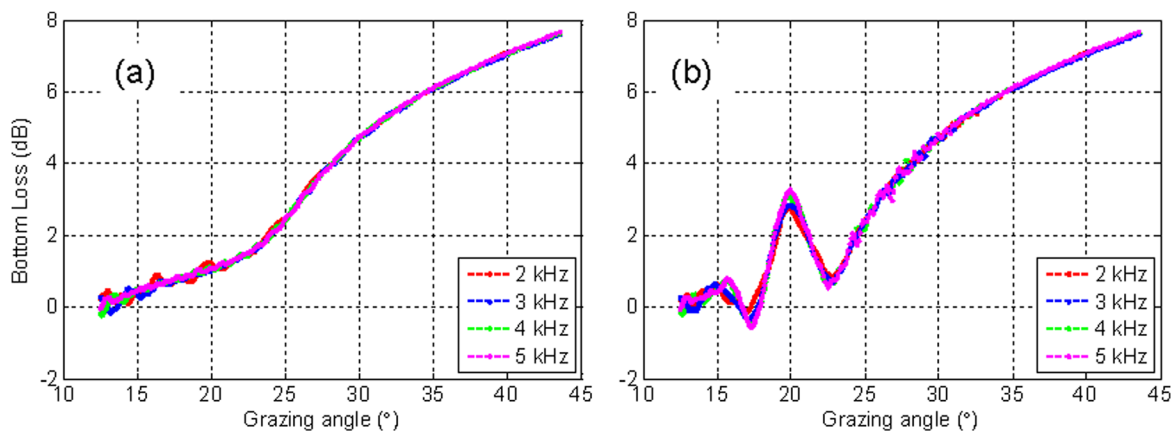

FIG. 11. (Color online) PE modeling results at 2, 3, 4, and 5 kHz with (a) flat bottom and (b) an 8 cm high Gaussian bottom feature.

Downloaded 27 Feb 2012 to 128.95.76.55. Redistribution subject to ASA license or copyright; see http://asadl.org/journals/doc/ASALIB-home/info/terms.jsp

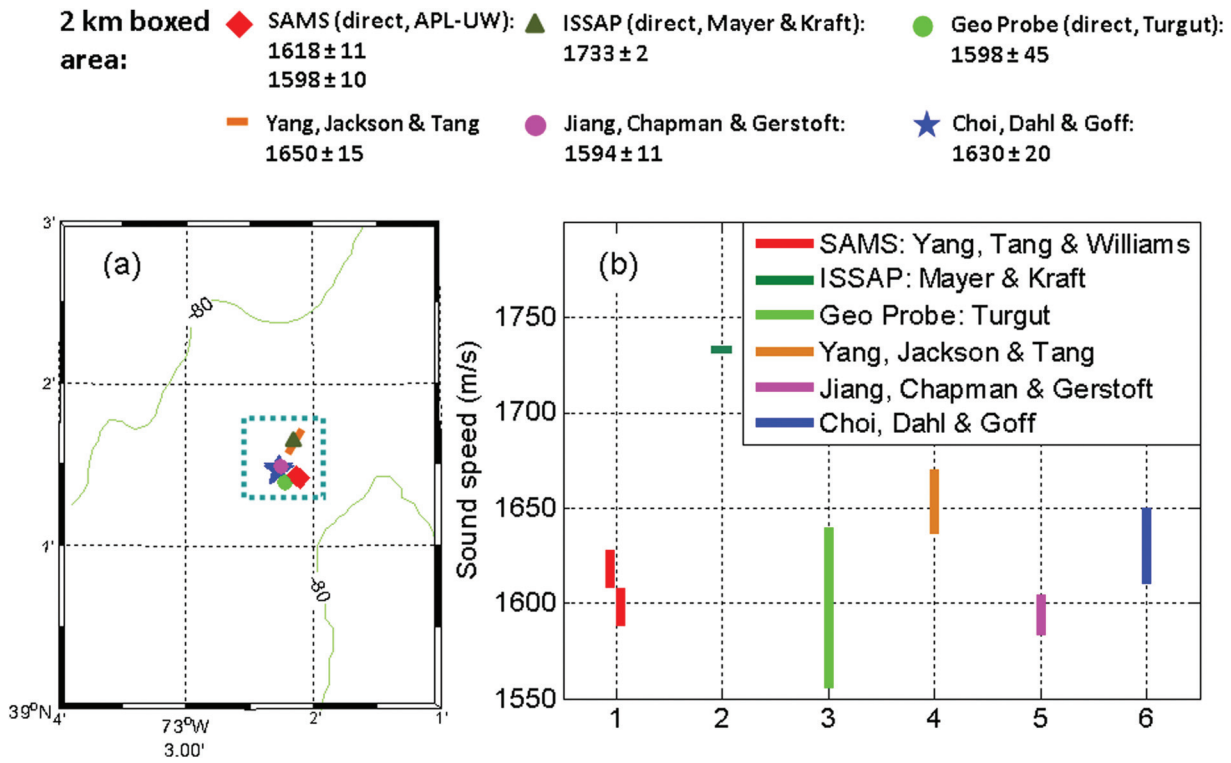

FIG. 12. Comparison of sediment sound speed between direct measurements and geoacoustic inversion results in SW06. (a) GPS locations for each measurement and (b) sediment sound speed results. Water sound speed near water/sediment interface is approximately 1498 m/s for SW06.

This frequency dependence may require further modeling effort in the future and can be due to finer-scale topographical changes than the Gaussian feature. Unfortunately, there is no ship echo sounder data or bathymetry data at the measurement site with enough resolution to confirm the topographical change. However, a bottom feature such as that shown here could occur even for a relatively flat site such as this. The importance of the modeling work is that it indicates how detailed the environmental sampling should be for mid-frequency propagation and inversion studies. In cases where it is not practical to use detailed bathymetry in inversion, averaging over several tracks may compensate the error seen in the present work.[27]

C. Comparison of sediment sound speed and attenuation between direct measurement and inversion

Direct measurement and geoacoustic inversion results of sediment sound speed and attenuation in SW06 are compared within a 2 km boxed area. The GPS plot for all measurements is shown in Fig. 12(a) and the sediment sound speed results are shown in Fig. 12(b). The sediment attenuation results are summarized in Table I.

In the 2 km boxed area, three direct measurements and three geoacoustic inversions are included. The three direct measurements use different instruments and they are Sediment Acoustic-speed Measurement System (SAMS, Ref. 24), ISSAP[22,23] and Geo Probe.[33] The penetration depths of SAMS, ISSAP, and Geo Probe are 1.6, 0.2, and 0.3 m, and measurements were carried out at 2–20, 65, and 20 kHz. The three inversion results included are the one from this work, work from Jiang *et al.*[34] and Choi *et al.*,[35] respectively. The three inversion results are from short range propagation data in the frequency bands of 2–5, 1.5–4.5, and 1–20 kHz, respectively.

For sediment sound speed comparison (Fig. 12) of the three direct measurement results, the ones using SAMS and Geo Probe are within each other's uncertainty bounds. Two of the inversion results, Jiang *et al.*[34] and Choi *et al.*,[35] are consistent with these two direct measurements. In addition, all four measurements as shown in Fig. 12(a) are in close vicinity. The other two results, i.e., the direct measurement result using ISSAP and the inversion result of this work, give higher sound speed and yet do not seem mutually consistent given the uncertainty in each. Note that the ISSAP operates at 65 kHz and, accounting for the 3% dispersion[31]

TABLE I. Comparison of sediment attenuation between direct measurement and geoacoustic inversion within a 2 km boxed area in SW06.

Reference name	Operating Frequency (kHz)	Attenuation (dB/m/kHz)
ISSAP	65	0.60
Geo probe	20	0.22
Yang, Jackson, and Tang	2, 3, 4, and 5	[0.05 0.17 0.45 0.48] (BL exclude feature) [0.20 0.40 0.63 0.60] (entire BL)
Jiang, Chapman, and Gerstoft	1.75–3.15	0.1
Choi, Dahl, and Goff	1–20	0.05

Downloaded 27 Feb 2012 to 128.95.76.55. Redistribution subject to ASA license or copyright; see http://asadl.org/journals/doc/ASALIB-home/info/terms.jsp

expected between 65 and 3 kHz, the ISSAP result would be consistent with the present work. The discrepancy between four measurements with lower values and the other two, considering their geographical locations, is likely due to spatial variation of sediment properties. Substantial spatial variation in sediment sound speed over small spatial scales has been reported in this area through the ONR-sponsored Geoclutter program.[18]

Sediment attenuation results from the same measurements in Fig. 12 except SAMS are summarized in Table I. In Table I, attenuation results of this work at individual frequencies, i.e., 2, 3, 4, and 5 kHz are listed for two cases: estimations using BL data with and without the 20° feature. Table I shows that attenuation of five measurements ranges from 0.05–0.6 dB/m/kHz within the 2 km boxed area. It is of interest to compare results from this work with those from Jiang *et al*. and Choi *et al*. which are in the same frequency range. The attenuation results of this work are consistent with Jiang *et al*. and Choi *et al*. if BL data excluding the 20° feature are used for inversion. As mentioned earlier, BL is sensitive to attenuation at low grazing angles, where BL data are more susceptible to topographical changes. Therefore, the estimation of attenuation is more affected by forward scattering from topographical changes than sediment density and sound speed (Fig. 10). For fine-scale topographic variability, the estimation of attenuation can be improved by repeating the experiment along different tracks and carrying out ensemble averaging.

IV. SUMMARY AND DISCUSSION

In this paper, geoacoustic inversion results using bottom loss data collected from SW06 in the frequency range of 2–5 kHz have been presented. Measured BL data exhibited a well-defined critical angle at all frequencies and little frequency dependence was observed. Uncertainties in BL were carefully identified, and it was found that uncertainties due to beam patterns, excluding fine-scale topography, are the dominant component.

A simple half space fluid model, with three parameters ρ, c, and α, was used for geoacoustic inversion. Inversion results were obtained by best matching between model and data in the least square sense. Inverted sediment sound speeds were used to compare with direct measurements and results using other inversion techniques in a $2\,\text{km} \times 2\,\text{km}$ area in SW06. The comparison yields consistency and discrepancy which are both correlated with the geographical locations for the measurements. This leads to the conclusion that the observed discrepancy may be due to spatial variations of sediment properties. The comparison of attenuation obtained in the same frequency range show that they are consistent and within the uncertainty bounds of this work if the feature at 20° is excluded for inversion.

The present work demonstrates the practicality of inverting geoacoustic parameters using BL data at mid-frequencies. In addition, the observations and modeling results from this work show that forward scattering from topographical changes is important at mid-frequencies and should be taken into account in sound propagation predictions and geoacoustic inversion. Most inversion work assumes flat, horizontally stratified bottom models and scattering from the bottom is usually ignored. In this work, the fluctuations observed in BL exceed the uncertainty bounds and may be due to forward scattering from fine-scale topographical changes. The feature around 20° may also be due to topographical change. Modeling work carried out to explain the feature requires a gentle but consistent topographical change with elevation on the order of 10 cm and spatial span of 50 m. Though this is a small elevation change, the resultant BL variation is about 2 dB with reference to a flat surface case between 2 and 5 kHz. In the present work, fluctuations in BL due to forward scattering from topographical changes do not alter the inversion results for sediment sound speed and density significantly but do affect the determination of attenuation and uncertainty bounds for all inverted parameters. In addition to uncertainty analysis of geoacoustic inversion, the results of this work also have impact on the development of measurement methods that can cope with fine-scale topographic variability, e.g., averaging over tracks.

ACKNOWLEDGMENTS

The authors would like to thank the Woods Hole Oceanographic Institution for providing all ocean mooring data. We thank Andrew A. Ganse at the Applied Physics Laboratory, University of Washington for helpful discussions. This work was supported by the Office of Naval Research.

[1]K. V. MacKenzie, "Reflection of sound from coastal bottoms," J. Acoust. Soc. Am. **32**, 221–231 (1960).
[2]H. P. Bucker, J. A. Whitney, G. S. Yes, R. R. Gardner, "Reflection of low frequency sonar signals from a smooth ocean bottom," J. Acoust. Soc. Am. **37**, 1037–1051 (1965).
[3]B. F. Cole, "Marine sediment attenuation and ocean bottom reflected Sound," J. Acoust. Soc. Am. **38**, 291–297 (1965).
[4]J. S. Hanna, "Short range transmission loss and evidence for bottom refracted energy," J. Acoust. Soc. Am. **53**, 1686–1690 (1973).
[5]D. C. Stickler, "Negative bottom loss, critical angle shift, and the interpretation of the bottom reflection coefficient," J. Acoust. Soc. Am. **61**, 707–710 (1977).
[6]N. R. Chapman, "Modeling ocean-bottom reflection loss measurements with the plane-wave reflection coefficient," J. Acoust. Soc. Am. **73**, 1601–1607 (1983).
[7]A. Robins, "Reflection of plane acoustic waves from a layer of varying density," J. Acoust. Soc. Am. **87**, 1546–1552 (1990).
[8]A. Robins, "Reflection of a plane wave from a fluid layer with continuously varying density and sound speed," J. Acoust. Soc. Am. **89**, 1686–1696 (1991).
[9]A. Robins, "Exact solutions of the Helmholtz equation for plane wave propagation in a medium with variable density and sound speed," J. Acoust. Soc. Am. **93**, 1347–1352 (1993).
[10]C. W. Spofford, "Inference of geo-acoustic parameters from bottom loss data," in *Bottom-Interacting Ocean Acoustics*, edited by W. A. Kuperman and F. B. Jensen (Plenum, New York, 1980), pp. 159–171.
[11]C. W. Holland, J. Dettmer, and S. E. Dosso, "Remote sensing of sediment density and velocity gradients in the transition layer," J. Acoust. Soc. Am. **118**, 163–177 (2005).
[12]C. W. Holland and J. Osler, "High-resolution geoacoustic inversion in shallow water: A joint time- and frequency-domain technique," J. Acoust. Soc. Am. **107**, 1263–1279 (2000).
[13]N. R. Chapman, K. Stinson, S. Levy, J. Cabrera, and D. W. Oldenburg, "Estimation of the elastic properties of seafloor sediments by inversion of precritical reflection data," IEEE J. Ocean. Eng. **13**(4), 215–221 (1988).
[14]N. Chotiros, "An inversion for biot parameters in water-saturated sand," J. Acoust. Soc. Am. **112**, 1853–1868 (2002).

Downloaded 27 Feb 2012 to 128.95.76.55. Redistribution subject to ASA license or copyright; see http://asadl.org/journals/doc/ASALIB-home/info/terms.jsp

[15]M. J. Isakson and T. B. Neilsen, "The viability of reflection loss measurement inversion to predict broadband acoustic behavior," J. Acoust. Soc. Am. **120**, 135–144 (2006).
[16]D. Tang, J. N. Moum, J. F. Lynch, P. Abbot, R. Chapman, P. H. Dahl, T. F. Duda, G. Gawarkiewicz, S. Glenn, J. A. Goff, H. Graber, J. Kemp, A. Maffei, J. D. Nash, and A. Newhall, "Shallow Water '06: A joint acoustic propagation/nonlinear internal wave physics experiment," Oceanography, **20**(4), 156–167 (2007).
[17]T. A. Davies, J. A. Austin, Jr., M. B. Lagoe, and J. D. Milliman, "Late Quaternary sedimentation off New Jersey: New results using 3-D seismic profiles and cores," Mar. Geol. **108**, 323–343 (1992).
[18]J. A. Goff, B. J. Kraft, L. A. Mayer, S. G. Schock, C. K. Sommerfield, H. C. Olson, S. P.S. Gulick, and S. Nordfjord, "Seabed characterization on the New Jersey middle and outer shelf: Correlatability and spatial variability of seafloor sediment properties," Mar. Geol. **209**, 147–172 (2004).
[19]J. A. Goff, J. A. Austin, Jr., S. Gulick, S. Nordfjord, B. Christensen, C. Sommerfield, H. Olson, and C. Alexander, "Recent and modern marine erosion on the New Jersey outer shelf," Mar. Geol. **216**, 275–296 (2005).
[20]S. Nordfjord, J. A. Goff, J. A. Austin, Jr., and C. K. Sommerfield, "Seismic geomorphology of buried channel systems on New Jersey shelf: Assessing past environmental conditions," Mar. Geol. **214**, 339–364 (2005).
[21]S. Nordfjord, J. A. Goff, J. A. Austin, Jr., and S. P. S. Gulick, "Seismic facies of incised valley-fills, New Jersey continental shelf: Implications for erosion and preservation processes acting during late Pleistocene/Holocene transgression," J. Sediment. Res. **76**, 1284–1303 (2006).
[22]B. J. Kraft, L. A. Mayer, P. Simpkin, P. Lavoie, E. Jabs, and J. A. Goff, "Calculation of *in situ* acoustic wave properties in marine sediments," in *Impact of Littoral Environmental Variability on Acoustic Predictions and Sonar Performance* (Kluwer Academic, Dordrecht, 2002), pp. 123–130.
[23]L. A. Mayer, B. J. Kraft, P. Simpkin, P. Lavoie, E. Jabs, and E. Lynskey, "In-Situ determination of the variability of seafloor acoustic properties: An example from the ONR geoclutter area," in *Impact of Littoral Environmental Variability on Acoustic Predictions and Sonar Performance* (Kluwer Academic, Dordrecht, 2002), pp. 115–122.
[24]J. Yang, D. Tang, and K. L. Williams, "Direct measurement of sediment sound speed using SAMS in SW06," J. Acoust. Soc. Am. **124**, 116–121 (2008).
[25]J. Yang, D. Rouseff, D. Tang, and F. S. Henyey, "Effect of the internal tide on acoustic transmission loss at mid-frequencies," IEEE J. Ocean. Eng. **35**(1), 3–11 (2010).
[26]H. W. Coleman and W. G. Steele, Jr., *Experimentation and Uncertainty Analysis for Engineers* (Wiley, New York, 1989), Chap. 3.
[27]K. L. Williams, "Forward scattering from a rippled sand/water interface: Modeling, measurements, and determination of the plane wave, flat surface reflection coefficient," IEEE J. Ocean. Eng. **34**(4), 399–406 (2009).
[28]L. M. Brekhovskikh and Y. P. Lysanov, *Fundamentals of Ocean Acoustics* (Springer-Verlag, New York, 2003), Chap. 4, pp. 87–91.
[29]J. X. Zhou, "Low-frequency geoacoustic model for the effective properties of sandy seabottoms," J. Acoust. Soc. Am. **125**, 2847–2866 (2009).
[30]R. C. Aster, B. Borchers, and C. H. Thurber, *Parameter Estimation and Inverse Problems* (Elsevier, Boston, 2005), Chap. 2.
[31]K. L. Williams, D. R. Jackson, E. I. Thorsos, D. Tang, and S. G. Schock, "Comparison of sound speed and attenuation measured in a sandy sediment to predictions based on the Biot theory of porous media," IEEE J. Ocean. Eng. **27**, 413–428 (2002).
[32]D. R. Jackson and M. D. Richardson, *High-Frequency Seafloor Acoustics* (Springer-Verlag, New York, 2007), Chap. 5.
[33]A. Turgut, and T. Yamanoto, "*In Situ* measurements of velocity dispersion and attenuation in New Jersey Shelf sediments," J. Acoust. Soc. Am. **124**, 122–127 (2008).
[34]Y.-M. Jiang, N. R. Chapman, and P. Gerstoft, "Short range travel time geoacoustic inversion with vertical line array," J. Acoust. Soc. Am. **124**, 135–140 (2008).
[35]J. W. Choi, P. H. Dahl, and J. A. Goff, "Observations of the R reflector and sediment interface reflection at the Shallow Water '06 Central Site," J. Acoust. Soc. Am. **124**, 128–134 (2008).

Downloaded 27 Feb 2012 to 128.95.76.55. Redistribution subject to ASA license or copyright; see http://asadl.org/journals/doc/ASALIB-home/info/terms.jsp

Direct measurement of sediment sound speed in Shallow Water '06

Jie Yang, Dajun Tang, and Kevin L. Williams
Applied Physics Laboratory, University of Washington, 1013 NE 40th Street, Seattle, Washington 98105-6698
jieyang@apl.washington.edu, djtang@apl.washington.edu, williams@apl.washington.edu

Abstract: Knowledge of sediment sound speed is crucial for predicting sound propagation. During the Shallow Water '06 experiment, *in situ* sediment sound speed was measured using the Sediment Acoustic-speed Measurement System (SAMS). SAMS consists of ten fixed sources and one receiver that can reach a maximal sediment depth of 3 m. Measurements were made in the frequency range 2–35 kHz. Signal arrival times and propagation distances were recorded, from which sediment sound speed was determined. Preliminary results from three deployments show that SAMS was capable of determining sediment sound speed with uncertainties less than 1.6%. Little dispersion in sediment sound speed was observed.

© 2008 Acoustical Society of America
PACS numbers: 43.30.Pc, 43.30.Ma, 43.30.Xm [WC]
Date Received: March 26, 2008 **Date Accepted:** May 19, 2008

1. Introduction

Acoustic interaction with the sea bottom is, in many cases, an essential component of sound propagation in a shallow water waveguide. *In situ* geoacoustic properties of the seabed, however, are difficult to obtain. Since the 1950s, *in situ* direct measurements have been carried out to study the sediment geotechnical properties.[1] More recently, sediment geoacoustic properties have been measured within the surfacial layer in the frequency range 1–100 kHz using either manually buried acoustic systems (Refs. 2–4) or specially designed underwater mechanical systems. Refs. 5–8, from the latter category, present systems that can penetrate into the sediment through their own gravitational forces. The *In Situ* Sediment geoacoustic Measurement System (Refs. 5–7) is designed for *in situ* measurements within the topmost 30 cm while the acoustic lance (Ref. 8) has a maximum penetration depth of 5 m.

As part of the experimental effort in Shallow Water '06 (SW06), the Sediment Acoustic-speed Measurement System (SAMS) was used to directly measure the sediment sound speed. SAMS is driven into the seabed by a powerful vibrocore, which allows precise penetration depth up to 3 m with arbitrary step size. The ground truth measurements are valuable not only in studying *in situ* sediment properties but also in providing sediment geoacoustic data to which inversion results can be compared.

This paper is organized as follows. In Sec. 2, the analyses of calibration and sediment data are presented. Section 3 summarizes and discusses future directions. System uncertainty analysis is given in the Appendix.

2. Data analysis

SAMS was deployed during the SW06 field experiment. Four data sets, one in the water column as calibration and three in the sediment, were recorded. For all data sets, three linear-frequency-modulated (LFM) "chirps" were used in the frequency bands 2–11, 10–21, and 20–35 kHz, which are referred to as low-, mid-, and high-frequency (LF, MF, and HF) in later analysis.

2.1 Analysis of calibration data

Calibration data were acquired in a bay environment and relatively far from the positions of the sediment measurements. For calibration, SAMS was deployed such that both sources and re-

 © 2008 Acoustical Society of America

Downloaded 07 Oct 2013 to 128.95.76.55. Redistribution subject to ASA license or copyright; see http://asadl.org/terms

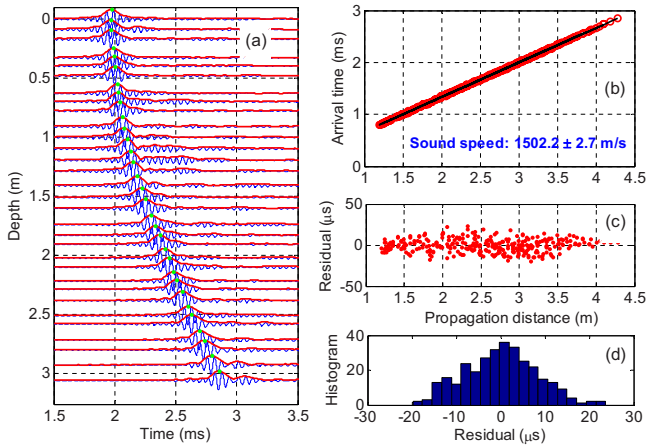

Fig. 1. (Color online) Pulse compression results at MF. (a) Waveforms received from source 10; (b) linear regression results; (c) linear regression residual scatter plot; (d) residual histogram.

ceiver were always within the water column. The analysis of the calibration data is used to augment the system geometry measurements and establish system uncertainty.

SAMS consists of a 3-m-tall triangular frame and a 2-m-long extension beam. Three sources are fixed on the triangular frame with the other seven on the extension beam. The receiver is located in the center of the frame and can be driven vertically into the sediment using a vibrocore. Horizontal distances between sources and receiver are between 1.18 and 2.97 m.

Data were taken at 31 receiver depths with a stepsize of about 0.1 m. At each depth, the ten sources sequentially transmitted three chirps and each was repeated five times. Pulse compression was carried out as an initial step in processing the data. In Fig. 1(a), pulse compressed waveforms received from source ten are plotted at their corresponding receiver depths. Signal arrival time is defined as the time at the peak of the envelope and highlighted with a dot. With signal arrival times defined, the speed of sound in water can be determined from the linear regression of the arrival times and distances between the sources and receiver. Five repeated pings are used to find the averaged arrival times yielding a total of 310 data points. The linear regression result, Fig. 1(b), is 1502.2 m/s with 2.7 m/s uncertainty at the 95% confidence level. The calculation of uncertainty assumes that the residuals (difference between data and fit function) are random and follow a normal distribution of zero mean and constant variance. A scatter plot of the residuals is shown in Fig. 1(c). Both the scatter plot and its histogram [Fig. 1(d)] indicate that the distribution of the residual is close to normal. Similar procedures are repeated for the LF and HF calibration data. The curve fitting results for the speed of sound in water are 1503.4±6.7 and 1503.1±3.4 m/s, respectively.

The sound speeds determined are close to each other with the confidence interval at MF and HF almost completely enclosed by that of the LF. The higher uncertainty at LF is due to a roughly 58% decrease in the total number of data points included in the curve fitting process. Beyond 2 m, the LF calibration data showed signals, possibly due to the tube waves, arriving prior to the direct arrivals and, therefore, were excluded from the curve fitting. Unfortunately, there was no conductivity-temperature-depth (CTD) record when the calibration data were taken. Concurrent ship data only provide temperature and salinity at the sea surface. Therefore, a total of 120 historical summer CTD data around the area were sought for reference. Individual distance to the SAMS calibration position varied from 16 to 52 km and water depth ranged 13–40 m. A strong thermocline was observed starting at around 10 m and water sound speed varied from 1520 m/s at the sea surface to 1495 m/s at 35 m. For calibration, bathymetry showed a 23 m water depth with SAMS suspended 5–6 m below the surface, i.e., measurements were taken at 6–9 m in depth. Compared with historical CTD data, the calibration results, 1503.4±6.7, 1502.2±2.7, and 1503.1±3.4 m/s, respectively, are reasonably within the

Downloaded 07 Oct 2013 to 128.95.76.55. Redistribution subject to ASA license or copyright; see http://asadl.org/terms

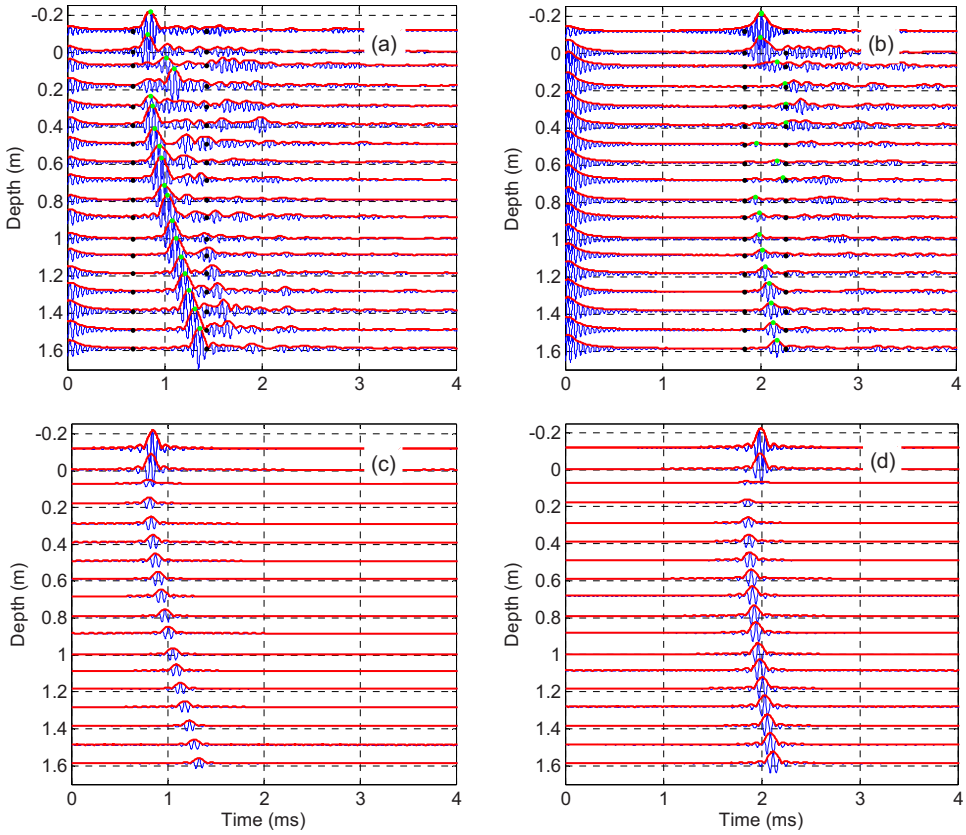

Fig. 2. (Color online) MF Pulse-compressed waveforms from: (a) source 1; (b) source 10 at different receiver depths. (c) and (d) are half-space Green's function simulations of (a) and (b), respectively.

variation range. More importantly, the acoustic data are of good quality and repeatable at different frequency bands, supporting the conclusion that the water sound speeds measured by SAMS are close to the true values at the time.

2.2 Analysis of sediment data

To start, two cases in the MF band from position 2 are chosen to show the characteristics of sediment data. The first case, Fig. 2(a), draws the signals from source 1 at 19 receiver depths with the maximum penetration depth around 1.6 m. Data are processed in the same way as the calibration. The receiver starts at about 10 cm above the sediment surface, which makes the first depth sample less than zero in the figure. In determining the signal arrival time, a time window is specified (bounded by the black dots) within which the peak of the signal envelope is recognized and highlighted with a green dot. It is quite obvious that there are two erroneous readings of the peak time in Fig. 2(a) as the receiver first enters the sediment. For sources that are further away from the receiver, there are more such occurrences as shown in Fig. 2(b). Data of this kind are carefully excluded from analysis. Signal-to-noise ratio drops considerably for the geometries realized in Fig. 2(b) due to the combined effects of longer acoustic path through the sediment and ray bending by the critical angle. A two-half space Green's function is used to simulate the scenario of Figs. 2(a) and 2(b) and the results are shown in Figs. 2(c) and 2(d). The critical angle effect is quite apparent in Fig. 2(d).

Downloaded 07 Oct 2013 to 128.95.76.55. Redistribution subject to ASA license or copyright; see http://asadl.org/terms

Table 1. Summary of sediment sound speed results.

		C_b (m/s)
Position 1	LF	1614.8 ± 8.7
	MF	1622.1 ± 12.5
Position 2	LF	1597.7 ± 11.0
	MF	1598.6 ± 9.8
Position 3	LF	1588.2 ± 15.8
	MF	1611.6 ± 24.8

To find sediment sound speed, the water sound speed close to the water–sediment interface is required. Throughout the experiment, CTD records show a very stable water sound speed at depths beyond 70 m. Based on CTD records, the water sound speed is 1496 m/s. Sediment sound speed is assumed homogeneous within the penetrated depth, 1.6 m. Ray tracing is carried out for each data point by varying sediment sound speed in the model and the closest match of arrival times between measurement and ray tracing determines the *in situ* sediment sound speed. The uncertainties are determined in the same manner as for the calibration (Sec. 2.1). Assuming uncertainty comes entirely from propagation in the sediment, the time and distance that are spent in water are removed from the total time and distance. The uncertainty in sediment sound speed is then calculated using the residuals at 95% confidence level.

Results are summarized in Table 1 and Fig. 3. Results from positions 1 and 2 show similar uncertainty bounds around 10 m/s and little dispersion between the two frequency bands. There is about a 20-m/s sound speed difference between the two positions, which is believed to be the true spatial variation. Results at position 3 have much larger uncertainties than the other two. Signs of signal degradation were observed (not shown here), which results in a 50% higher mean residual than the other two positions. Geological studies around the SW06 region (Ref. 9), using interpreted chirp seismic reflection data, indicate a substantial difference in sediment properties at position 3 from positions 1 and 2, which is believed to be the cause for higher uncertainty at position 3. In addition, acoustic measurements of bottom reflection (Ref. 10) were made in the vicinity of SAMS positions 1 and 2 in the frequency range 1–20 kHz. The geoacoustic inversion results of sediment sound speed, with co-located coring and stratigraphic studies, are consistent with the direct measurement results using SAMS.

3. Summary and future directions

In this paper, direct measurements of sediment sound speed using the Sediment Acoustic-speed Measurement System (SAMS) have been presented. The calibration data were first analyzed to establish the system uncertainty, which is approximately 3 m/s. Sediment data were taken at three positions. Sediment sound speeds and uncertainties are summarized in Table 1 and Fig. 3. Results indicate a 20-m/s sound speed variation between positions 1 and 2. At position 3, the

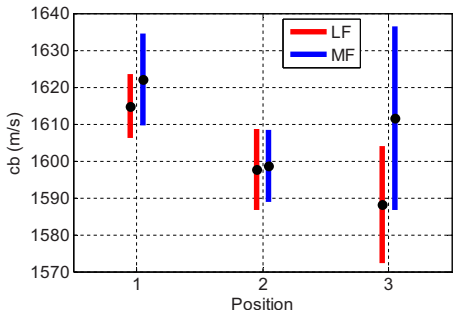

Fig. 3. (Color online) Sediment sound speeds with uncertainties at three positions.

Downloaded 07 Oct 2013 to 128.95.76.55. Redistribution subject to ASA license or copyright; see http://asadl.org/terms

increase in uncertainty may be attributed to the sediment properties based on geological studies around the central experimental area in SW06. The sediment sound speeds found at positions 1, 2, and 3 are 1618 ± 11, 1598 ± 10, and 1600 ± 20 m/s, respectively. Little dispersion in sediment sound speed was observed. Direct measurement of sediment sound speed dispersion has been found in sandy sediments (Refs. 2 and 11). The dispersion was observed to be at its greatest in the frequency range 800–2000 Hz. In this work, the frequency coverage is higher than the pronounced transition region of dispersion, which may explain the observed lack of dispersion. Future directions include improvement of system uncertainty in sediment sound speed, determination of sediment attenuation and its dispersion relation, and depth dependence of sediment geoacoustic properties.

Acknowledgment

This work was supported by the Office of Naval Research.

Appendix: System uncertainty analysis

For a system like the SAMS, the dimension and propagation time uncertainties limit the resolution of sound speed measurement. Uncertainty can come from both measurements and methodology utilized to analyze data. In this work, part of the uncertainty comes from measurement of distances, i.e., horizontal distance and initial depth offset between sources and receiver; initial depth offset between receiver and the sediment surface; and receiver depth reading. The reading of the arrival times falls in the latter category.

Following Ref. 12, a general function q with multiple variables $(x, y, z, \ldots)$ has uncertainty:

$$\delta q = \sqrt{\left(\frac{\partial q}{\partial x}\delta x\right)^2 + \left(\frac{\partial q}{\partial y}\delta y\right)^2 + \left(\frac{\partial q}{\partial z}\delta z\right)^2 + \cdots}. \tag{A1}$$

In Eq. (A1), variables $x, y, z, \ldots$ are independent measurements with uncertainties $\delta x, \delta y, \delta z, \ldots$. For this work, the general function is the speed of sound in water, c_w, which is the ratio of distance and time:

$$c_w = \frac{r(x,y,z,\cdots)}{t} = \frac{\sqrt{x^2 + (h+d)^2}}{t}, \tag{A2}$$

where r is the slant distance, t is travel time; x, h, and d are horizontal distance, receiver depth, and initial vertical distance between source and receiver. Following Eq. (A1), the uncertainty in calibration can be written as

$$\delta c_w = \sqrt{\left(\frac{\partial c_w}{\partial x}\delta x\right)^2 + \left(\frac{\partial c_w}{\partial h}\delta h\right)^2 + \left(\frac{\partial c_w}{\partial d}\delta d\right)^2 + \left(\frac{\partial c_w}{\partial t}\delta t\right)^2}. \tag{A3}$$

The individual uncertainties $\delta x, \delta h, \delta d$ are defined as 0.9, 0.1, and 0.5 cm. Specifically, δx is set to $\frac{1}{4}$ of the source dimension; δd is set to $\frac{1}{4}$ of the receiver dimension; δh accounts for depth reading uncertainty. In Eq. (A3), the most difficult part is to determine δt. The receiver is embedded inside a stainless steel tube with two rectangular windows open on the side. The combination of direct arrival and reflections off the window may slightly change the location of the signal peak. Assuming this window effect is random, δt can be determined using the mean residual obtained from Fig. 1 as 7.5 μs. Figure 4 shows the uncertainty corresponding to each source. For each of them, as depth increases, the uncertainty decreases from top to bottom. The black dashed line is the mean value for each source. It is obvious that sources that are closer to the receiver have higher uncertainty and spreading. The least uncertainty for an individual measurement is around 5 m/s.

In calibration analysis, data recorded from all ten sources were used in the linear regression to find the speed of sound in water, i.e., a relationship between individual (Fig. 4) and overall uncertainty (Fig. 1) needs to be clarified. The overall system uncertainty can be deter-

Downloaded 07 Oct 2013 to 128.95.76.55. Redistribution subject to ASA license or copyright; see http://asadl.org/terms

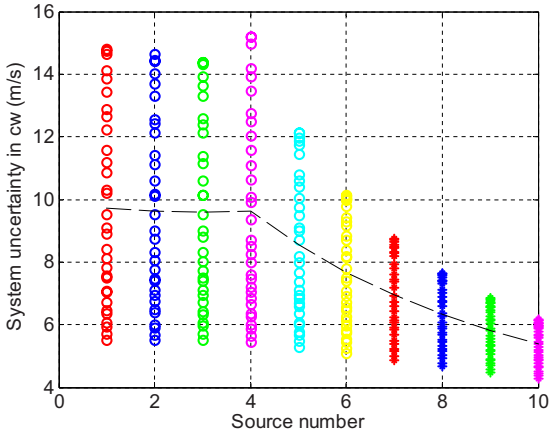

Fig. 4. (Color online) System uncertainty in the speed of sound in water.

mined from the individual uncertainties in Fig. 4 as a two-step process. First, assume an ideal system with no uncertainty, i.e., find propagation times by dividing measured propagation distances by a fixed sound speed. The value c_w=1502.2 m/s, determined from calibration at MF, is used. The linear regression shows a perfect fit between propagation distance and time with zero uncertainty. Second, convert the maximum uncertainty of each source δc_w, as in Fig. 4, to its equivalent uncertainty in distance, i.e., by multiplying δc_w with corresponding propagation time t. Then, the measured propagation distances were added a random quantity in the range of $\pm t \times \delta c_w$. The linear regression is carried out again by forcing c_w=1502.2 m/s. The system uncertainty at 95% confidence interval is calculated in a similar fashion as in Sec. 2. This uncertainty, determined to be ±1.6 m/s, is the overall system uncertainty.

References and links

[1]E. L. Hamilton, G. Shumway, H. W. Menard, and C. J. Shipek, "Acoustic and other physical properties of shallow-water sediments off San Diego," J. Acoust. Soc. Am. **28**, 1–15 (1956).
[2]A. Turgut and T. Yamamoto, "Measurements of acoustic wave velocities and attenuation in marine sediments," J. Acoust. Soc. Am. **87**, 2376–2383 (1990).
[3]A. I. Best, Q. J. Huggett, and A. J. K. Harris, "Comparison of in situ and laboratory acoustic measurements on Lough Hyne marine sediments," J. Acoust. Soc. Am. **110**, 695–709 (2001).
[4]G. B. N. Robb, A. I. Best, J. K. Dix, P. R. White, T. G. Leighton, J. M. Bull, and A. Harris, "Measurements of the in situ compressional wave properties of marine sediments," IEEE J. Ocean. Eng. **32**, 484–496 (2007).
[5]A. Barbegelata, M. D. Richardson, B. Miaschi, E. Muzi, P. Guerrini, L. Troiano, and T. Akal, "ISSAMS: An in situ sediment acoustic measurement system," in *Shear Waves in Marine Sediments*, edited by J. M. Hoven, M. D. Richardson, and R. D. Stoll (Kluwer, Dordrecht, 1991).
[6]M. D. Richarson, D. L. Lavoie, and K. B. Briggs, "Geoacoustic and physical properties of carbonate sediments of the lower Florida Keys," Geo-Mar. Lett. **17**, 316–324 (1997).
[7]M. J. Buckingham and M. D. Richardson, "On tone-burst measurements of sound speed and attenuation in sandy marine sediments," IEEE J. Ocean. Eng. **27**, 429–453 (2002).
[8]S. S. Fu, R. H. Wilkens, and L. N. Frazer, "Acoustic lance: New in situ seafloor velocity profiles," J. Acoust. Soc. Am. **99**, 234–242 (1996).
[9]J. A. Goff, B. J. Kraft, L. A. Mayer, S. G. Schock, C. K. Sommerfield, H. C. Olson, S. P. S. Gulick, and S. Nordfjord, "Seabed characterization on the New Jersey middle and outer shelf: Correlatability and spatial variability of seafloor sediment properties," Mar. Geol. **209**, 147–172 (2004).
[10]J. W. Choi, P. H. Dahl, and J. A. Goff, "Observations of the R reflector and sediment interface reflection at the Shallow Water '06 Central Site," J. Acoust. Soc. Am. **124**, EL128–EL134 (2008).
[11]K. L. Williams, D. R. Jackson, E. I. Thorsos, D. Tang, and S. G. Schock, "Comparison of sound speed and attenuation measured in a sandy sediment to predictions based on the Biot theory of porous media," IEEE J. Ocean. Eng. **27**, 413–428 (2002).
[12]J. R. Taylor, *An Introduction to Error Analysis*, 2nd ed. (University Science Books, 1997).

Downloaded 07 Oct 2013 to 128.95.76.55. Redistribution subject to ASA license or copyright; see http://asadl.org/terms

Effect of the Internal Tide on Acoustic Transmission Loss at Midfrequencies

Jie Yang, Daniel Rouseff, *Senior Member, IEEE*, Dajun Tang, and Frank S. Henyey

***Abstract*—Nonlinear internal waves are a common event on the continental shelf. The waves depress the high-gradient region of the thermocline and thicken the surface mixed layer with consequent effect on acoustic propagation. After the waves have passed, it may take several hours for the thermocline to rise to its prewave level. To examine the effect of the rising thermocline, oceanographic and acoustic data collected during the 2006 Shallow Water Experiment (SW06) are analyzed. Midfrequency acoustic data (1.5–10.5 kHz) taken for several hours at both fixed range (550 m) and along a tow track (0.1–8.1 km) are studied. At the fixed range, the rising thermocline is shown to increase acoustic intensity by approximately 5 dB. Along the tow track, the transmission loss changes 2 dB for a source–receiver pair that straddles the thermocline. Using oceanographic moorings up to 2.2 km away from the acoustic receiver, a model for the rising thermocline is developed. This ocean model is used as input to a broadband acoustic model. Results from the combined model are shown to be in good agreement with experimental observation. The effects on acoustic signals are shown to be observable, significant, and predictable.**

***Index Terms*—Acoustic signal processing, nonlinear ocean internal waves, underwater acoustic telemetry.**

I. Introduction

DENSITY stratification in the ocean leads to the propagation of internal waves. In deep water, these waves are essentially linear and are commonly modeled as a random process [1]. In shallow water, more event-like, nonlinear waves [2] can be generated that display bore-like features [3]. Driven by the interaction of the tide with bottom topography, nonlinear internal waves depress the high-gradient region of the thermocline on the order of 10 m and propagate at wave speeds on the order of 1 m/s. The effects these propagating ocean waves have on acoustic propagation can be dramatic. At low frequencies, they produce an observed rapid decorrelation of acoustic modes [4] and a subsequent recorrelation that can be explained using a coupled mode model [5], [6]. Also at low frequencies, they can cause horizontal refraction leading to focusing and defocusing [7], [8]. The presence of nonlinear internal waves affects the horizontal coherence length at both low [9] and high [10], [11] frequencies.

Manuscript received February 06, 2009; revised September 29, 2009; accepted November 12, 2009. First published February 02, 2010; current version published February 10, 2010. This work was supported by the U.S. Office of Naval Research.

Associate Editor: J. F. Lynch.

The authors are with the Applied Physics Laboratory, University of Washington, Seattle, WA 98105-6698 USA (e-mail: jieyang@apl.washington.edu; rouseff@apl.washington.edu; djtang@apl.washington.edu; frank@apl.washington.edu).

Color versions of one or more of the figures in this paper are available online at http://ieeexplore.ieee.org.

Digital Object Identifier 10.1109/JOE.2009.2038984

In the cited papers, the primary emphasis was on how acoustic signals are affected by nearby nonlinear internal waves. The internal waves, however, are but one manifestation of the internal tide that is generated by the tide passing over the continental shelf break. Due to nonlinearities, the deeper thermocline part of the internal tide travels faster than the higher thermocline part. In a rather short distance, the deepest part of the wave catches up to the shallowest part and high-frequency nonlinear waves form as part of the resulting bore. A second manifestation of the internal tide is the slow rising of the thermocline after the wave has passed. In this paper, the emphasis is on how acoustic signals are affected by these gradual changes in the water column.

The topic is relevant to acoustics because the rising thermocline caused by the internal tide may last for several hours while nonlinear internal waves may transect a given acoustic track for only a small fraction of the tidal period. At short ranges, where the acoustic arrivals can be separated in time, the gradual rising of the thermocline is shown to change acoustic intensity by approximately 5 dB. At longer ranges, the transmission loss is shown to change by 2 dB as the thermocline rises. Calculations using a range-independent broadband parabolic equation model are shown to produce mean transmission loss results consistent with experimental observations at both short and long ranges. The results suggest that the enduring effects of passing nonlinear internal waves on mean acoustic transmission loss should be observable, significant, and predictable. In addition, the results have implications on studies such as geoacoustic inversion using transmission loss data.

The data reported in this paper were collected during the 2006 Shallow Water Experiment (SW06) performed on the continental shelf off the coast of New Jersey [12]. Oceanographic results are described in Section II. Thermistor data show how the high-gradient region of the thermocline is depressed by nonlinear internal waves and rises only gradually to its background state. Results are shown to be consistent with an oceanographic model based on a solution to the Dubriel–Jacotin–Long (DJL) equation. Acoustic results are described in Section III. Seven hours of acoustic data collected in the 1.5–10.5-kHz band at a range 550 m are presented for a period before, during, and immediately after the passage of an internal wave. Subsequent to the passage of the wave, another eight hours of data were collected on a tow track with the range steadily increasing from 100 m to 8 km. Good model/data agreement is demonstrated for both fixed- and towed-source scenarios. The results are discussed in Section IV.

II. Ocean Data and Modeling

Fig. 1 shows the effect of the internal tide on sound speed as observed during SW06. The sound speed is plotted as a function

0364-9059/$26.00 © 2010 IEEE

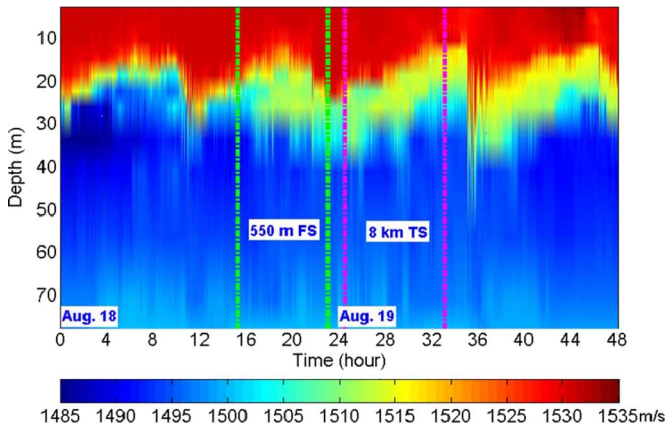

Fig. 1. Effect of the slow rising of the thermocline after passing nonlinear internal waves. Sound speed as function of depth for a 48-h period beginning 00:00:00 Universal Time Zone (UTC) August 18, 2006, during SW06. Nonlinear internal waves depress isotachs at approximately the M2 tidal cycle. Isotachs gradually rise before being again depressed by next wave. Superimposed are regions where two acoustic data sets were collected: source at fixed station (FS) with range 550 m; and towed source (TS). (Mooring data were acquired by the Woods Hole Oceanographic Institution.)

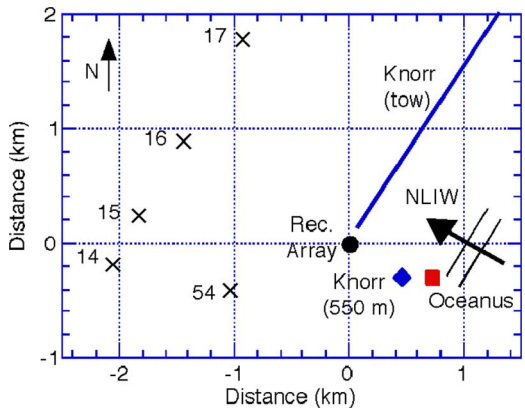

Fig. 2. Positions of deployed assets. The acoustic receiving array's position defines the origin. Five thermistor-chain moorings used in current analysis are labeled 14–17 and 54. (Thermistor chain 54 used to generate Fig. 1.) The *R/V Knorr* position is shown for fixed station (550 m) acoustic transmissions. Position of the *R/V Oceanus* shown at 21:14:00 UTC August 19, 2006, when nonlinear internal wave labeled NLIW was encountered. Beginning of the *R/V Knorr*'s track for subsequent towed source transmissions is also shown.

of depth for 48 h [13]. For this section of data, the thermocline's high-gradient region was thrust several meters downward as internal waves passed at approximately the M2 tidal period of 12.4 h. After a wave has passed, the thermocline rises only gradually to what could loosely be considered a background profile. Consequently, while the main part of the internal wave may be near a sensor for only a short period, the complete internal tide effect may last for several hours.

The pattern displayed in Fig. 1 was observed throughout SW06. The experiment featured a total of 62 acoustics and physical oceanographic moorings deployed in a geometry shaped like a "T" [12]. Of present interest are five oceanographic moorings positioned as shown in Fig. 2 on an 80-m isobath. Additional oceanographic data were collected from the *R/V Knorr* and *R/V Oceanus*.

During the 48-h period shown in Fig. 1, two acoustic data sets were collected. In the first, acoustic signals were transmitted from the *R/V Knorr* at a fixed station to a vertical receiving array 550 m away. In the second, the *R/V Knorr* slowly towed the acoustic source away from the receiving array. Fig. 1 shows the time periods when these two acoustic data sets were collected and Fig. 2 shows the positions of the acoustic assets relative to the oceanographic moorings. In this section, an oceanographic model is developed that can be used to explain the acoustic observations detailed in Section III. Note that the oceanographic moorings do not coincide with either of the acoustic tracks. Consequently, the extent to which these relatively distant oceanographic measurements can be used to model conditions along the acoustic tracks must be tested.

The most dramatic feature of Fig. 1 is the strong depression in the thermocline when nonlinear internal waves pass. The *R/V Oceanus* was positioned as shown in Fig. 2 at 21:14:00 UTC on August 18, 2006, when it was passed by a large amplitude wave. X-band radar measurements from the ship indicated the wave's bearing as 288° and speed as 0.89 m/s [14]. Using these direct measurements as ground truth, the first task is to develop a theoretical model for the rapid thermocline depression caused by the internal wave. The second task is to develop a practical model that uses as input only data collected on the oceanographic moorings.

A. DJL Model for Nonlinear Internal Waves

Fully nonlinear solitary waves in a continuously stratified flow can be described by the DJL equation [2], [15]. A solitary internal wave is a single wave that propagates with an unchanging shape. Unlike other descriptions of these waves, no small-amplitude assumption is made; quite moderate amplitudes, such as those encountered in SW06, exceed the small amplitude requirements of these other approaches.

Although the waves of present concern are parts of a wave train, it has been found, both in SW06 and in other measurements [16], that the DJL equation gives a rather good description of the first wave in a wave train. This is because the first wave is well separated from the later ones and therefore, it can be treated as a solitary wave. For a given background stratification that exists before a wave arrives, there are one-parameter families of solitary waves. Each family has a different modal character. In the Turkington *et al.* [17] iterative algorithm for finding the lowest mode family of solutions of the DJL equation, the free parameter is chosen to be the potential energy of the solution. Given the potential energy, all other characteristics of the wave are determined. To find which DJL solution applies to a particular wave, some characteristic, normally the amplitude, is fitted to the wave. From the corresponding solution, other variables such as the wave speed are determined. Present calculations use a slight modification of the Turkington *et al.* algorithm; the modification improves the convergence when measured stratification is used.

The background stratification used as input to the DJL equation was from a conductivity–temperature–depth (CTD) cast taken on August 18, 2006, at 17:01:00 UTC from the *R/V Knorr*, fully 4 h before the next major internal wave was encountered.

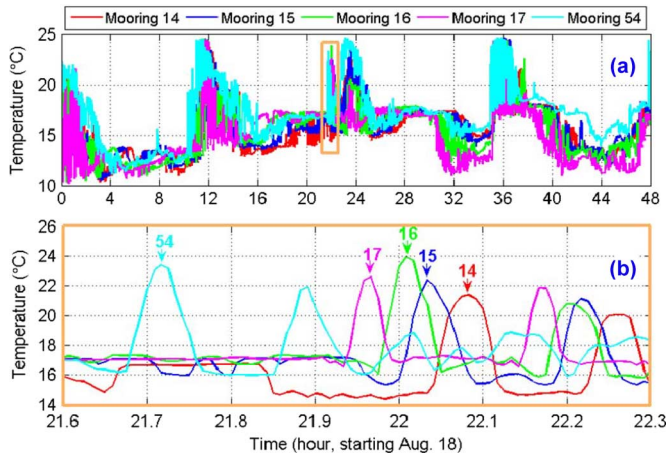

Fig. 3. Temperature record at depth 25 m from the five thermistor-chain moorings shown in Fig. 2. (a) Complete 48-h period. (b) Enlargement with arrows pointing to arrival of the large nonlinear internal wave for each sensor [boxed region in (a)]. Observations used to estimate speed and bearing of wave.

The wave speed of the internal wave is calculated as a function of the internal wave amplitude. Taking the wave amplitude from measurements at mooring 54 (Fig. 2), the predicted wave speed is 0.86 m/s. The conclusion is that the wave speed can be predicted from first principles given knowledge of the ambient stratification and a reasonable estimate of the wave amplitude.

B. Mooring-Based Model

The five oceanographic moorings in Fig. 2 sampled the temperature every 30 s. Moorings 14–17 had three sensors each while mooring 54 had 10. Fig. 3(a) shows the temperature record from each mooring at approximate depth 25 m for the complete 48-h record. Fig. 3(b) is an enlargement emphasizing the time period near when the internal wave observed by the *R/V Oceanus* arrived at the arrays. The arrows indicate when the peak internal wave displacement was observed on each sensor.

To estimate properties of the internal wave using only the mooring data, the wave is modeled locally as a plane wave. Using the arrival times from Fig. 3(b) as input, the bearing and speed of the wave are then estimated by a least squares fit. The resulting calculation gives speed 0.81 m/s and bearing 292°. The agreement with ground-truth speed 0.89 m/s and bearing 288° is good. The moorings were in water depth slightly shallower than the *R/V Oceanus* so a slightly lower wave speed would be expected.

The plane-wave model for nonlinear internal waves is clearly limited. SW06 was performed in a region where new internal waves were spawned rapidly [18]. Wavefront curvature and merging between different waves may be significant. Still, the agreement between the mooring-based model and ground-truth measurements is encouraging; it suggests that the mooring data can be used to infer at least the gross characteristics of the internal wave field as would have been encountered on the acoustic tracks several kilometers away (Fig. 2).

Using the bearing and speed estimated from the plane-wave ocean model, it can be determined that the internal wave takes approximately 16 min to propagate from the acoustic receiving array to mooring 54. Similarly, it takes 10 min for the internal wave to propagate from the *R/V Knorr* to the receiving array for the 550-m range transmission experiment. Based on these calculations, the following ocean model is proposed for use in the acoustic simulations: mooring 54 temperature data are smoothed over a sliding window a minimum of 10 min in duration. Then, the smoothed temperature records are offset by a minimum of 16 min to correct for the propagation time from the acoustic receiving array. Then, the smoothed, offset temperature profiles are combined with salinity data to calculate the sound-speed profile (SSP) at the acoustic receiving array. This SSP is then used in range-independent acoustic simulations as detailed in the following section. The proposed slowly varying, range-independent ocean model would be expected to fail in the immediate vicinity of nonlinear internal waves. However, calculations in the following section will show it to be adequate for capturing the gross effects of the rising thermocline as observed in the acoustic experiment.

III. Acoustic Data and Modeling

As noted in Section II, the present analysis concerns two acoustic data sets collected on August 18–19, 2006. For the first, the *R/V Knorr* was at a fixed station, 550 m from the receiving array. The 550-m range was selected because it was expected to be comparable to the typical width of a nonlinear internal wave. At this range, it was expected that the different acoustic arrivals could be separated from one another and studied individually. For the second, the acoustic source was slowly towed out to a maximum range of 8.1 km. The two data sets allow the effects of the rising thermocline on acoustic propagation to be examined over a range of temporal and spatial scales.

For both data sets, acoustic signals were recorded on a moored receiving system positioned at 39° 01.47′ N, 73° 02.262′ W (Fig. 2). The system [19] included two vertical subarrays, each with four elements: a shallow subarray with elements at depths 25.0, 25.2, 25.5, and 26.4 m, and a deep subarray with elements at 50.0, 50.2, 50.5, and 51.4 m. Signals were transmitted using an ITC-2015 transducer (International Transducer Corporation) positioned at nominal depth 40 m off the stern of the *R/V Knorr*. Linear frequency-modulated (LFM) chirp signals, 20 ms in duration, were transmitted with an approximate repetition rate of 19 s. The midfrequency chirps swept from 1.5–10.5 kHz with a raised cosine window and 10% taper. In subsequent processing, the received signals were pulse compressed using replicas obtained from calibration data. Details of how the replicas were generated are given in the Appendix.

A. Fixed Source

On August 18, 2006, beginning at 15:16:00 UTC and ending at 22:32:00 UTC, acoustic data were collected at a nominal range 550 m. From Fig. 1, this coincides with a period before, during, and immediately after the passage of a nonlinear internal wave. The current analysis emphasizes the period before and after the wave; the period during the wave was studied previously [14].

A total of 1400 acoustic transmissions were recorded at range 550 m. Fig. 4 shows the signals received at depths 25 and 50 m after pulse compression for the duration of the experiment. The

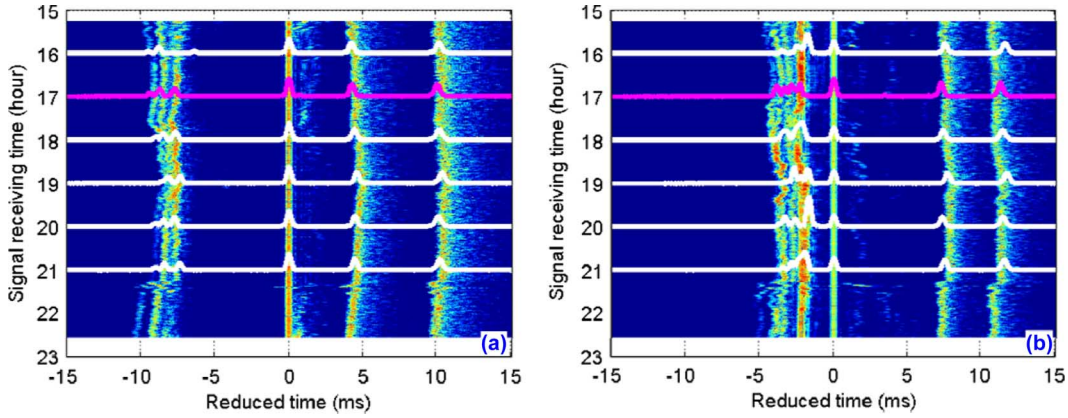

Fig. 4. Acoustic arrival structure with source at fixed station, range 550 m. Pulse compression output versus geotime. (a) Receiver at depth 25 m. (b) Receiver at depth 50 m (35-dB dynamic range). Superimposed are simulation results; see text for details.

signals were aligned using the bottom-bounce arrival as reference; reduced time in the figure is with reference to this arrival. The bottom bounce was observed to be the most stable arrival throughout the entire data set. The figure shows the first 30 ms of the compressed signal, sufficient to show the first four arrival groups and all acoustic paths with at most one reflection off the sea surface and one reflection off the seabed.

There are features in Fig. 4 worth considering in more detail. At depth 25 m, the first group of arrivals, between −10 and −5 ms, consists of three paths: two waterborne direct paths and a sea surface reflection. This first group of arrivals gets more compact, i.e., the relative arrival time difference between the three paths decreases between hours 15 and 19. Shortly after hour 21, there is a strong acoustic effect produced by the passage of an internal wave. It takes 10 min for the main part of the internal wave to pass between the source and the receiver [14]. After the internal wave passes, the arrival time and the time width of the first group become more like what was observed around hour 15. However, gradual changes in the arrival structure between hours 15 and 19 are less apparent than at depth 25 m.

The experimental results in Fig. 4 demonstrate that the effects produced by a nonlinear internal wave on acoustic signals are manifest for several hours. The primary goal of the acoustic modeling is to reproduce the gradual changes in the acoustic arrival structure that are observed in the data after the wave has passed. Of present interest is the slowly varying acoustic intensity for the multiple acoustic arrivals. Rapid fluctuations in intensity—scintillation—are beyond the scope of this study. Given that the interest is only in the slowly varying mean intensity, the modeling approach is to assume a time-varying but range-independent representation for the ocean (Section II). A secondary goal is to see if this relatively simple ocean model can account for the acoustic observations. If it can, it implies that bulk acoustic characteristics can be predicted successfully with relatively sparse environmental information as input.

Acoustic propagation was simulated using the parabolic equation (PE) method [20], [21]. This work focuses on data/model comparison in the frequency band of 1.5–6 kHz. Broadband pulses were generated by Fourier synthesis; to fill the 1.5–6-kHz band, 1798 separate single-frequency PE calculations were made. The sediment parameters (fluid bottom) used were as follows: sound speed 1620 m/s [22], density 1.85 g/cm^3, and attenuation 0.5 dB/λ [23].

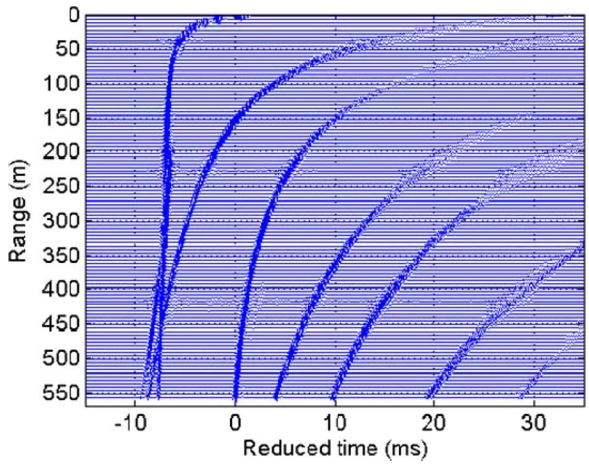

Fig. 5. Simulated acoustic arrival structure out to range 550 m for receiver depth 25 m. Beyond range 450 m, multiple direct and surface bounce paths are not separated in time.

Fig. 5 shows the synthesized time series for receiver depth 25 m as a function of range. The calculation is taken to the 550-m range used in the experiment and the reduced time is again referenced to the bottom-bounce path. The SSP used in the calculation is derived from a CTD cast taken from the *R/V Knorr* at 17:01:00 UTC. The time window 50 ms is longer than used in Fig. 4 and sufficient to include two additional acoustic paths: the surface–bottom–surface bounce path and the bottom–surface–bottom bounce path. As the range increases beyond about 450 m, the early arriving paths merge and form a group. This first group, between −10 and −5 ms, consists of three arrivals. These three arrivals correspond to a fast direct, a surface bounce, and a slow direct arrival. Beamforming results indicate that, in a ray picture, all three arrivals come from above the receiver.

The simulation results, using the CTD cast as input in Fig. 5 at range 550 m, can be compared to the experimental observations. The simulation results are overlaid in Fig. 4 by the solid line (magenta for color online) at hour 17. For both depths 25 and 50 m, the simulations are in good agreement with data predicting both number of arrivals and corresponding arrival times.

To examine the thermocline rising effect and make model/data comparisons as time evolves, it is necessary to use time-dependent SSPs as input to the model. However, the number of CTD casts from the *R/V Knorr* was limited and it is necessary to use as input data collected on the nearby environmental moorings. Using the algorithm developed in Section II, mooring 54 data are used to construct the SSPs. A 10-min sliding window was applied to the temperature data. The measurements were offset by 20 min to compensate for the travel time between the midpoint of the acoustic track and mooring 54. A total of 22 such profiles were generated representing the changing environment over the 7-h fixed position experiment.

Simulation results at selected times are superimposed over the experimental data in Fig. 4 as well. Note that the simulation curves at times other than hour 17 (CTD input) use the mooring data (white lines). Starting once more with depth 25 m, the model/data comparison shows good agreement not only in the arrival time but also in the varying compactness of the first group of arrivals. Similar comparisons of the later arrivals show similar good agreement. For depth 50 m, the agreement between data and modeling is also consistent.

With the arrival structure well characterized, the next test for the model is signal intensity. As noted earlier, the first group of arrivals for depth 25 m is the most sensitive to the rising thermocline. The model should reproduce the observed increase in intensity as the thermocline rises. It should also show a drop in intensity as the thermocline is depressed, the most dramatic instance being during the passage of an internal wave. This can be simply explained as follows: when the thermocline is depressed by the passing wave, the receiver at 25 m can be regarded as out of the sound channel; as the thermocline rises, the receiver at 25 m is then in the channel, and therefore, the received signal has much higher intensity. In addition, the change of thermocline depth is expected to affect paths that go through the mixed layer more than the other paths as seen in the first group of arrivals received at 25 m.

Fig. 6 shows the signal intensity (with mean removed) of the first arrival group at depth 25 m for the entire 7-h period. The thin line shows the raw data and the heavy line is the data averaged over a 10-min sliding window. Consistent with Fig. 4, the correlation between increasing signal intensity and the rising thermocline is apparent between hours 15 and 20. Between hours 20 and 21, the thermocline is slightly depressed followed by strong depression after hour 21 when the internal wave passes. Signal intensity reaches its lowest level when the thermocline is greatly depressed by the internal wave. Comparing measured intensity before and after the passage of the internal wave shows approximately 5-dB difference. Simulation results in Fig. 6 are shown as interconnected dots. The acoustic simulations reproduce the broad characteristics of the data with particularly good agreement before hour 20. Between hour 20 and 22, the simulation over predicts the observed intensity. This is not surprising as the range-independent environmental model used in the simulation is clearly inadequate when the nonlinear internal waves are nearby. The internal waves drive acoustic energy into the seabed and increase loss, a factor not included in the model. At hour 22, after the internal wave has passed, the model/data agreement improves as might be expected.

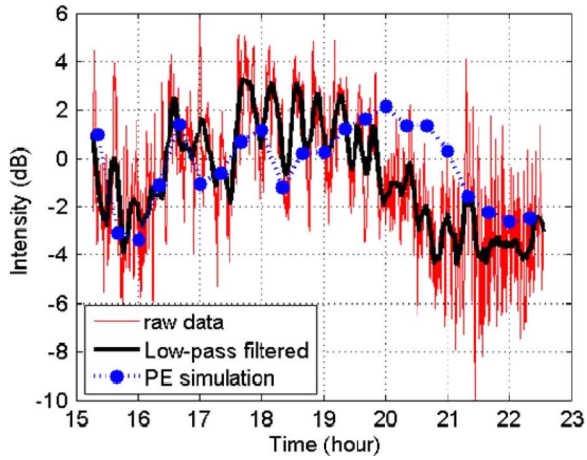

Fig. 6. Model/data comparison for integrated signal intensity of the first arrival group at depth 25 m. Thin line: raw data. Thick line: lowpass filtered data. Dotted line: simulation.

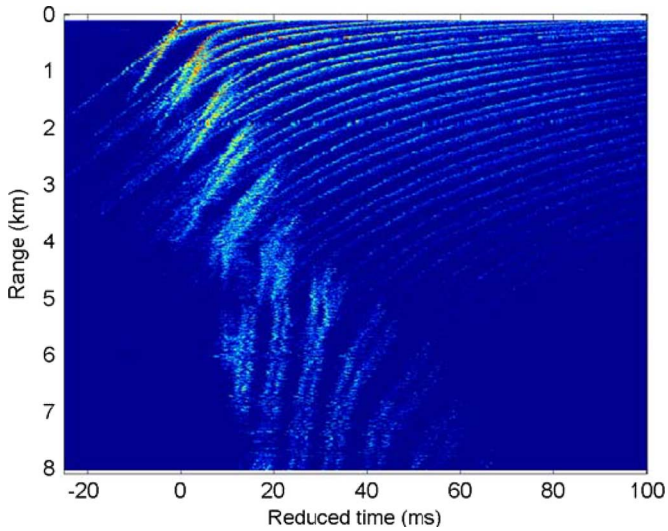

Fig. 7. Acoustic arrival structure for towed source. Pulse compression output versus range at depth 25 m using frequency band 1.5–6 kHz for the entire tow track.

B. Towed Source

On August 19, 2006, beginning at 00:30:00 UTC and ending at 09:03:00 UTC, towed source acoustic data were collected. The tow began approximately 2 h after the fixed source data presented in Section III-A and 3 h after the passage of the last internal wave event (Fig. 1). The source was towed by the *R/V Knorr* at depth 40 m and speed 0.26 m/s along an 80-m isobath. The range to the acoustic receiving array increased steadily from 104 m to 8.1 km; Fig. 2 shows the beginning of the track. Using the same LFM chirp signals as used earlier, 1285 transmissions were recorded.

Fig. 7 shows the complete 8-km towed-source data after pulse compression for the shallow receiver at 25 m. In this figure, the reduced time is the difference between actual signal propagation time and propagation time at a reference sound speed of 1495 m/s. The multiple arrivals, bouncing between the surface and the bottom, are apparent until they bundle together to form distinct groups as modes at approximately 4-km range.

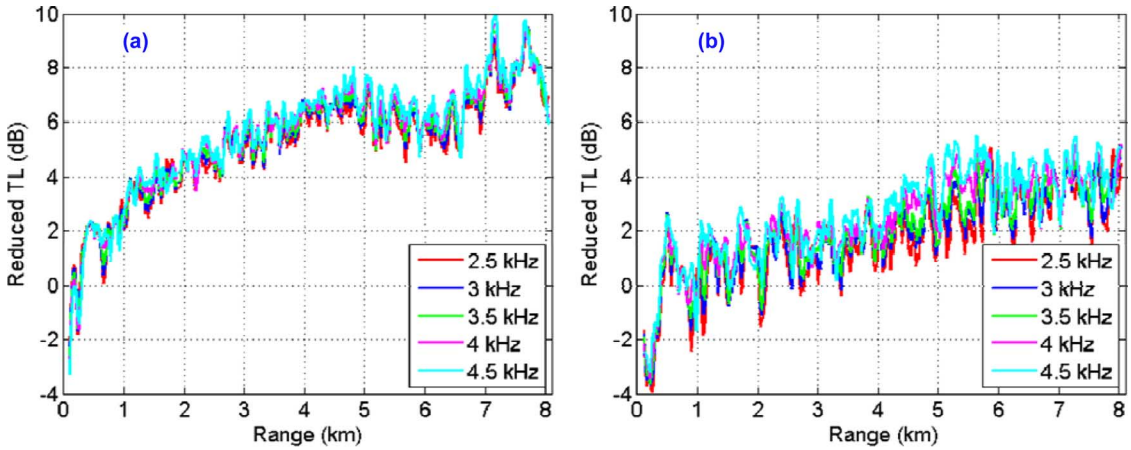

Fig. 8. Reduced transmission loss versus range for towed source. (a) Receiver depth 25 m. (b) Receiver depth 50 m.

At very short range, the first three arrivals are the direct, surface, and bottom bounce paths. As range increases beyond 0.4 km, the direct and surface bounce paths merge as observed at fixed range (Fig. 4) and predicted in numerical simulation (Fig. 5). Another interesting feature is the short paired arrivals observed repeatedly for range up to 4 km between -10 and 20 ms. They appear regularly at certain ranges and last about 10 ms. Using ray tracing technique, these arrivals are identified as ray paths that are reflected off the bottom and turn at the end of the warm mixed surface layer around 20 m. One of the pair of arrivals corresponds to launch angles going upward from the source (40 m) to the receiver (25 m) and the other corresponds to launch angles going downward. The widths of these short arrivals, in terms of range and time, are determined by how wide the ray bundle spans at receiver depth 25 m.

The reduced transmission loss for the shallow (25 m) and deep (50 m) receivers is shown in Fig. 8. Results are plotted at 5 frequencies, each with 1-kHz bandwidth. In this context, the reduced transmission loss corrects for the cylindrical spreading and the frequency-dependent water absorption. The calibration data discussed in the Appendix are used to normalize the tow data at each frequency as well. Results shown in Fig. 8 have been smoothed over range (125 m), which removes the large frequency-dependent multipath interference. Without the smoothing, results would differ greatly between different frequencies.

Several observations can be made from Fig. 8. For both depths, the reduced transmission loss generally increases with range. The shallow receiver exhibits 4–5 dB more loss than the deep at 8 km. The extra 4–5-dB loss for the shallow receiver, in terms of normal modes, is due to the more attenuative modes residing at depth 25 m. For the shallow receiver, the reduced transmission loss is only weakly dependent on frequency. The loss actually decreases by approximately 2 dB between 5 and 7 km before again increasing with range. For the deep receiver, the reduced transmission loss has two "plateaus" at the beginning and the end with a transition region in the middle between 4 and 6 km. The results at five selected frequencies are fairly close in the two plateau regions while there is a slight increase in loss between 5 and 6 km at high frequencies, e.g., at 4.5 kHz.

Fig. 9 shows a sampling of SSPs measured at mooring 54 (Fig. 2) during the towed source experiment. Each profile represents an average over a time window 20 min in duration. Noted next to each profile is the time at the center of the window and the associated range between the towed source and the acoustic receiving array. The double sound-speed duct, discussed relative to Fig. 7(b), is apparent within the first 3 h and diminishes as the thermocline rises. As manifestations of the rising thermocline, the deep sound channel axis shifts from depth 45 to 37 m while the mixed surface layer depth shrinks from approximately 20 to 10 m over the 8-h period.

The goal of the modeling effort is to develop a model that captures the essential features of the experimental results in Figs. 7 and 8. Certain gross features, such as the reduced transmission loss generally increasing with range, can be explained by interaction with the lossy seabed. Other more detailed features, such as the split arrivals in Fig. 7 and the transmission loss plateaus in Fig. 8, depend on the detailed features of the SSP in the water column. From Fig. 9, it is apparent that the towed source data were collected during a period when the thermocline was rising. To capture the detailed feature of the data, the model must include a rising thermocline.

As in Section III-A, the acoustic model assumes a range-independent ocean with the slowly varying SSP derived from mooring data. Clearly, this is an approximation that becomes increasingly coarse as the source–receiver range increases and the towed source gets further from the oceanographic moorings (Fig. 2). A total of 27 SSPs from mooring 54, each a 20-min average, represented the evolving environment over 8.5 h. A particular profile was used in the acoustic simulation only for source–receiver ranges applicable for that 20-min period. The final modeling result is obtained by piecing together the 27 segments of reduced transmission loss at their corresponding ranges. Bottom parameters were unchanged from Section III-A.

Fig. 10 compares the model to data for the reduced transmission loss at receiver depths 25 and 50 m. The comparison is at 2.5 kHz with 1-kHz bandwidth. The thin line represents data while the thick line represents simulation results. In general, for both receiver depths, there is good model/data agreement. As might be expected, the agreement is particularly good for short ranges—less than perhaps 4 km—where the model reproduces

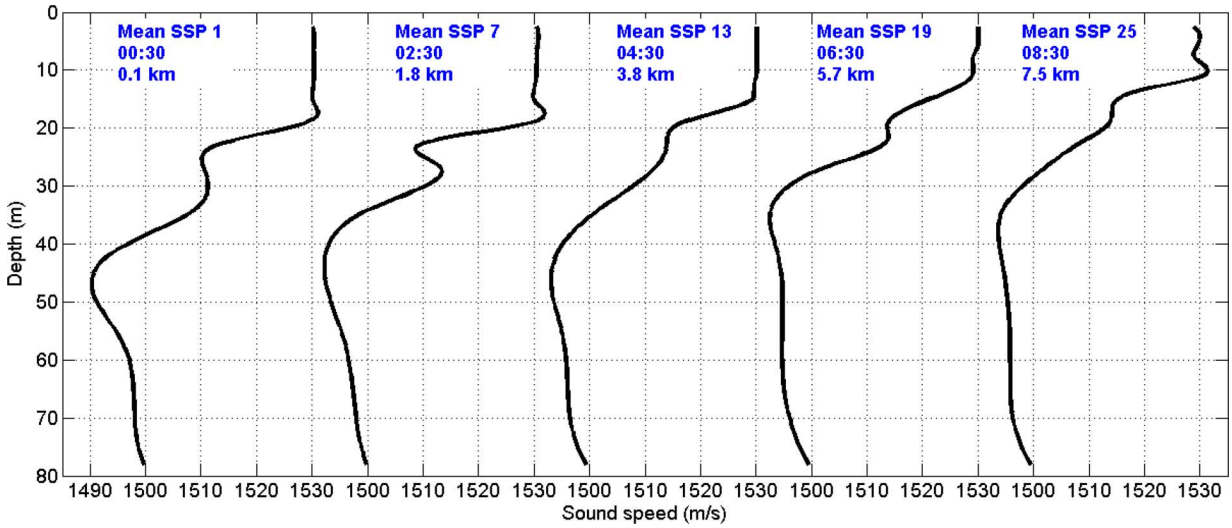

Fig. 9. Time-evolving SSP during the 8-h towed source experiment. X-axis: sound speed for each profile in range [1490 1530] m/s.

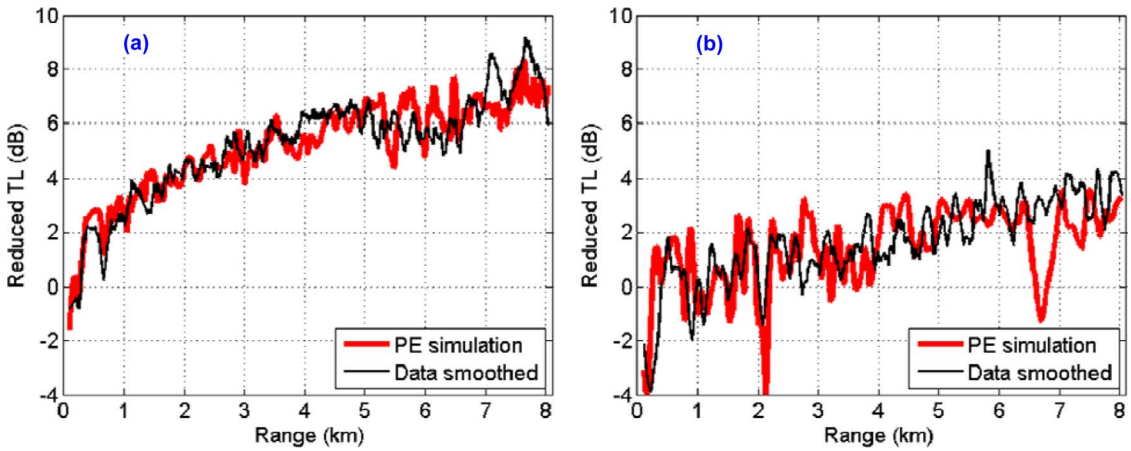

Fig. 10. Model/data comparison for reduced transmission loss versus range, towed source, frequency 2.5 kHz. Thin line: lowpass filtered data; thick line: simulation. (a) Receiver depth 25 m. (b) Receiver depth 50 m.

even the finer features. At depth 25 m, the model captures the plateau between 5 and 7 km and the subsequent increase in reduced transmission loss at greater ranges. The largest error is for the 50-m receiver at ranges between 6 and 7 km where the model underpredicts the reduced transmission loss. It has been observed through numerical experiments that the deep receiver can sometimes exhibit significant convergence-zone-like oscillations due to the complexity of the SSP. The occurrence of such oscillations depends on environmental information such as relative depth between source and the deep sound channel axis and depth of the shallow sound channel axis. The dip for the deep channel happens to be in the valley of that type of oscillation. Furthermore, the 4–5-dB difference in loss between the shallow and deep receivers is also well characterized by simulation results.

IV. Summary

Nonlinear internal waves depress the high-gradient region of the thermocline. After the waves have passed, the thermocline rises only gradually towards its prewave level. Rapid depression of the thermocline followed by gradual rising, both manifestations of the internal tide, was observed repeatedly during SW06. This work emphasizes the effect that the gradually rising thermocline has on acoustic propagation in the midfrequency band. The effect is shown to be significant for the receiver within the thermocline (25 m): at fixed range (550 m), the arrival structure changes and there is a 5-dB change in the intensity of the first arrival group. Similarly, the towed source data shows a 2-dB increase in total intensity as the thermocline rises.

Using nearby mooring data, a simple plane-wave model for the internal wave was developed. The speed and bearing for the internal wave produced by this simple model were shown to be in good agreement with both concurrent radar observations and theoretical calculations based on the DJL equation. The bearing and speed estimates were used to calculate the time offset between the environment as measured at the moorings and what would have been encountered along the acoustic tracks. A model for the SSP results that can be used in acoustic simulations is as follows: the sound speed is treated as range independent but slowly varying in time as the thermocline rises. Without including this time dependence, the 5-dB change in transmission

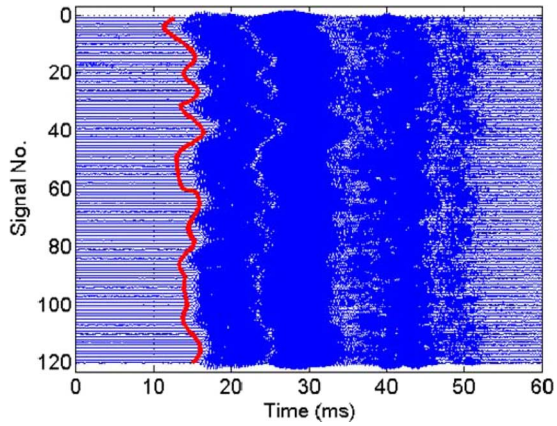

Fig. 11. Calibration data for 120 consecutive transmissions, depth 25 m. Raw LFM signals without pulse compression. Superimposed heavy line shows source–receiver range derived from gyroscope and GPS data and used to correct relative motion.

loss observed in Fig. 6 would not be captured by the model. The time-dependent model also captures the finer features in the towed source data (Fig. 10), particularly for ranges less than 4 km. A single SSP is not adequate for predicting transmission loss levels. In addition, if transmission loss data is used for geoacoustic inversion, as many do, it is important to consider the effect of the rising thermocline.

Internal waves are one manifestation of the internal tide. Another manifestation is the slowly rising thermocline that occurs after the wave has passed. With respect to acoustic propagation, while the effect of internal waves may be more dramatic, the effect of the rising thermocline may be much longer lived. Results from this paper show the latter effect to be both observable in the data and predictable with a simple model.

APPENDIX

The analysis in Section III uses replica to time compress LFM signals. Pulse compression has been widely used in signal processing as it helps to achieve the desired range resolution with a reduced power of the transmitter. This Appendix outlines how the replicas are generated. Compensating for relative motion between the acoustic source and receiver is shown to be an important step in generating reliable replicas.

Calibration data were taken on August 11, 2006. Signals were transmitted from a source at depth 30 m off the stern of the *R/V Knorr* and received 50 m away at the receiving array. Of present interest is the LFM part of the signal sweeping from 1.5 to 10.5 kHz over 20 ms. Fig. 11 shows the LFM part of the signal received at depth 25 m for 120 consecutive transmissions with repetition rate 10 s. Two points should be observed. First, the arrival time wanders by 5 ms over the duration of the calibration. Second, without pulse compression, the different acoustic paths are not separated in time. The direct path signal, for example, overlaps with the surface reflected path.

The wander in Fig. 11 is greater than what can be attributed to ocean variability. The wander instead is presumably due to relative motion between the source deployed off the ship and the moored receiver. Using the ship's global positioning system (GPS) and gyroscope measurements to estimate the source–receiver range independent of the acoustic observations can test this presumption. The heavy line superimposed on Fig. 11 shows the travel time calculated using the estimated source–receiver range divided by the mean sound speed. The agreement is good and suggests the practicality of compensating for source–receiver motion when using multiple transmissions to estimate the replica.

Estimating the replica signal when there is overlap between multiple acoustic paths involves several steps. First, the signal is pulse compressed to separate the different arrivals. The direct arrival is isolated and decompressed. Then, the decompressed direct arrivals from each of the transmissions are aligned after compensating for source–receiver motion. Coherent averaging across the transmissions yields the replica. The procedure is repeated for each element in the receiving array.

ACKNOWLEDGMENT

The authors would like to thank the crew of the *R/V Knorr* for their professional support. They would also like to thank the Woods Hole Oceanographic Institution, Woods Hole, MA, for providing all ocean mooring data.

REFERENCES

[1] W. Munk, "Internal waves and small-scale processes," in *Evolution of Physical Oceanography*, B. A. Warren and C. Wunch, Eds. Cambridge, MA: MIT Press, 1981, pp. 264–291.

[2] K. R. Helfrich and W. K. Melville, "Long nonlinear internal waves," *Annu Rev. Fluid Mech.*, vol. 38, pp. 395–425, 2006.

[3] F. S. Henyey and A. Hoering, "Energetics of borelike internal waves," *J. Geophys. Res.*, vol. 102, pp. 3323–3330, 1997.

[4] R. H. Headrick, J. F. Lynch, J. Kemp, A. Newhall, K. von der Heydt, J. R. Apel, M. Badiey, C.-S. Chiu, S. Finette, M. Orr, B. Pasewark, A. Turgut, S. Wolf, and D. Tielbuerger, "Acoustic normal mode fluctuation statistics in the 1995 SWARM internal wave scattering experiment," *J. Acoust. Soc. Amer.*, vol. 107, pp. 201–220, 2000.

[5] D. Rouseff, A. Turgut, S. N. Wolf, S. Finette, M. H. Orr, B. H. Pasewark, J. R. Apel, M. Badiey, C.-S. Chiu, R. H. Headrick, J. F. Lynch, J. Kemp, A. Newhall, K. von der Heydt, and D. Tielbuerger, "Coherence of acoustic modes propagating through shallow water internal waves," *J. Acoust. Soc. Amer.*, vol. 111, pp. 1655–1666, 2002.

[6] J. A. Colosi, "Acoustic mode coupling induced by shallow water nonlinear internal waves: Sensitivity to environmental conditions and space-time scales of internal waves," *J. Acoust. Soc. Amer.*, vol. 124, pp. 1452–1464, 2008.

[7] M. Badiey, B. G. Katsnelson, J. F. Lynch, and S. Pereselkov, "Frequency dependence and intensity fluctuations due to shallow water internal waves," *J. Acoust. Soc. Amer.*, vol. 122, pp. 747–760, 2007.

[8] J. Lou, M. Badiey, E. A. Karjadi, B. Katsnelson, A. Tskhoidze, J. F. Lynch, and J. N. Moum, "Observation of sound focusing and defocusing due to propagating nonlinear internal waves," *J. Acoust. Soc. Amer.*, vol. 124, pp. EL66–EL72, 2008.

[9] J. M. Collis, T. F. Duda, J. F. Lynch, and H. A. Deferrari, "Observed limiting cases of horizontal field coherence and array performance in a time-varying internal wavefield," *J. Acoust. Soc. Amer.*, vol. 124, pp. EL97–EL103, 2008.

[10] F. S. Henyey, D. Rouseff, J. M. Grochocinski, S. A. Reynolds, K. L. Williams, and T. E. Ewart, "Effect of internal waves and turbulence on a horizontal aperture sonar," *IEEE J. Ocean. Eng.*, vol. 22, no. 2, pp. 270–280, Apr. 1997.

[11] K. L. Williams, F. S. Henyey, D. Rouseff, S. A. Reynolds, and T. E. Ewart, "Internal wave effects on high frequency acoustic propagation to horizontal arrays: Experiment and implications to imaging," *IEEE J. Ocean. Eng.*, vol. 26, no. 1, pp. 102–112, Jan. 2001.

[12] D. Tang, J. N. Moum, J. F. Lynch, P. Abbot, R. Chapman, P. H. Dahl, T. F. Duda, G. Gawarkiewicz, S. Glenn, J. A. Goff, H. Graber, J. Kemp, A. Maffei, J. D. Nash, and A. Newhall, "Shallow Water '06, a joint acoustic propagation/nonlinear internal wave physics experiment," *Oceanography*, vol. 20, pp. 156–167, 2007.

[13] Y. T. Lin, A. E. Newhall, T. F. Duda, and J. F. Lynch, "Merging data sources for full water-column sound speed estimation in the New Jersey Shallow Water 2006 experiment," *IEEE J. Ocean. Eng.*, 2010, submitted for publication.
[14] D. Rouseff, D. Tang, K. L. Williams, Z. Wang, and J. N. Moum, "Mid-frequency sound propagation through internal waves at short range with synoptic oceanographic observations," *J. Acoust. Soc. Amer.*, vol. 124, pp. EL73–EL77, 2008.
[15] R. R. Long, "Some aspects of the flow of stratified fluids. I. A theoretical investigation," *Tellus*, vol. 42, pp. 42–58, 1953.
[16] F. Henyey, T. Duda, and J. Lynch, "Solitary wave model for waves observed in ASIAEX," *Eos Trans. AGU*, vol. 84, no. 52, 2004, Ocean Sci. Meet. Suppl., Abstract OS42D-05.
[17] B. Turkington, A. Eydeland, and S. Wang, "A computational method for solitary waves in a continuously stratified fluid," *Stud. Appl. Math.*, vol. 85, pp. 93–127, 1991.
[18] E. L. Shroyer, J. N. Moum, and J. D. Nash, "Observations of polarity reversal in shoaling non-linear internal waves," *J. Phys. Oceanogr.*, vol. V39, no. 3, pp. 691–701, 2009.
[19] P. H. Dahl, J. W. Choi, N. J. Williams, and H. C. Graber, "Field measurements and modeling of attenuation from near-surface bubbles for frequencies 1–20 kHz," *J. Acoust. Soc. Amer.*, vol. 124, pp. EL163–EL169, 2008.
[20] M. D. Collins, "A split-step Pade' solution for the parabolic equation method," *J. Acoust. Soc. Amer.*, vol. 93, pp. 1736–1742, 1993.
[21] A. P. Rosenberg, "A new rough surface parabolic equation program for computing low-frequency acoustic forward scattering from the ocean surface," *J. Acoust. Soc. Amer.*, vol. 105, pp. 144–153, 1999.
[22] J. Yang, D. Tang, and K. L. Williams, "Direct measurement of sediment sound speed in Shallow Water 06," *J. Acoust. Soc. Amer.*, vol. 124, pp. EL116–EL121, 2008.
[23] J.-X. Zhou, X.-Z. Zhang, and D. P. Knobles, "Low-frequency geoacoustic model for the effective properties of sandy seabottoms," *J. Acoust. Soc. Amer.*, vol. 125, pp. 2847–2866, 2009.

Jie Yang received the B.S. degree in physics from the Ocean University of Qingdao, Qingdao, China, in 1999 and the Ph.D. degree in mechanical engineering from the Georgia Institute of Technology, Atlanta, in 2007.

Since 2007, she was a Postdoctoral Fellow supported by the U.S. Office of Naval Research and then a Physicist with the Applied Physics Laboratory, University of Washington, Seattle. Her research interests are ocean acoustics and acoustical oceanography.

Dr. Yang is a member of the Acoustical Society of America.

Daniel Rouseff (S'86–M'89–SM'95) received the Ph.D. degree in electrical engineering from the University of Washington, Seattle, in 1989.

Upon graduation, he joined the Senior Professional Staff at the Milton S. Eisenhower Research Center, The Johns Hopkins University Applied Physics Laboratory, Laurel, MD. In 1992, he returned to the University of Washington where he is currently a Senior Engineer at that university's Applied Physics Laboratory. In 1997, he was an A.S.E.E.–U.S. Navy Senior Faculty Fellow at the Acoustic Signal Processing Branch of the Naval Research Laboratory, Washington, DC. In 2001, he was a Senior Visiting Fellow in the Department of Applied Mathematics and Theoretical Physics, Cambridge University, Cambridge, U.K. Since 2006, he has also been an Adjunct Research Associate Professor at the Department of Electrical and Computer Engineering, Portland State University, Portland, OR. His primary technical interests are underwater acoustics and acoustical oceanography.

Dr. Rouseff is a Fellow of the Acoustical Society of America.

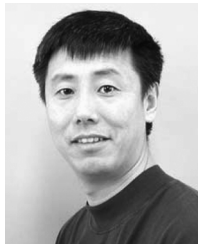

Dajun Tang received the B.S. degree from the University of Science and Technology, Hefei, China, in 1981, the M.S. degree from the Institute of Acoustics, Beijing, China, in 1985, and the Ph.D. degree in oceanographic engineering from the Joint Program of Massachusetts Institute of Technology, Cambridge/Woods Hole Oceanographic Institution, Woods Hole, MA, in 1991.

From 1991 to 1996, he was an Assistant Scientist and then Associate Scientist with the Woods Hole Oceanographic Institution. In 1996, he joined the Applied Physics Laboratory, University of Washington, Seattle, where he is currently a Senior Oceanographer. His research interests are acoustic interactions with the sea bottom.

Dr. Tang is a Fellow of the Acoustical Society of America.

Frank S. Henyey received the Ph.D. degree in theoretical physics from the California Institute of Technology, Pasadena, in 1967.

He held postdoctoral and faculty positions at the University of Michigan and research positions at the LaJolla Institute (where he was Associate Director of the Center for Studies of Nonlinear Dynamics) and Areté Associates. Since 1991, he has been at the University of Washington, Seattle, as a Principal Physicist in the Ocean Physics Department of the Applied Physics Laboratory. He is a seagoing theoretical physicist with interests in ocean acoustics and small-scale ocean hydrodynamics.

Dr. Henyey is a Fellow of the Acoustical Society of America and a member of the American Physical Society and the American Geophysical Union.

REPORT DOCUMENTATION PAGE

Form Approved
OMB No. 0704-0188

The public reporting burden for this collection of information is estimated to average 1 hour per response, including the time for reviewing instructions, searching existing data sources, gathering and maintaining the data needed, and completing and reviewing the collection of information. Send comments regarding this burden estimate or any other aspect of this collection of information, including suggestions for reducing the burden, to Department of Defense, Washington Headquarters Services, Directorate for Information Operations and Reports (0704-0188), 1215 Jefferson Davis Highway, Suite 1204, Arlington, VA 22202-4302. Respondents should be aware that notwithstanding any other provision of law, no person shall be subject to any penalty for failing to comply with a collection of information if it does not display a currently valid OMB control number.

PLEASE DO NOT RETURN YOUR FORM TO THE ABOVE ADDRESS.

1. REPORT DATE *(DD-MM-YYYY)*	2. REPORT TYPE	3. DATES COVERED *(From - To)*
12/30/2014	Final Technical Report	11/01/2010 to 09/30/2014

4. TITLE AND SUBTITLE

Mid-Frequency Reverberation Measurements with Full Companion Environmental Support

5a. CONTRACT NUMBER

5b. GRANT NUMBER

N00014-11-01-0188

5c. PROGRAM ELEMENT NUMBER

6. AUTHOR(S)

Dajun Tang

5d. PROJECT NUMBER

5e. TASK NUMBER

5f. WORK UNIT NUMBER

7. PERFORMING ORGANIZATION NAME(S) AND ADDRESS(ES)

Applied Physics Laboratory
University of Washington
1013 NE 40th Street
Seattle, WA 98105

8. PERFORMING ORGANIZATION REPORT NUMBER

9. SPONSORING/MONITORING AGENCY NAME(S) AND ADDRESS(ES)

Office of Naval Research
875 North Randolph Street
Arlington, VA 22203

10. SPONSOR/MONITOR'S ACRONYM(S)

ONR

11. SPONSOR/MONITOR'S REPORT NUMBER(S)

12. DISTRIBUTION/AVAILABILITY STATEMENT

Distribution Statement A: Approved for public release; distribution is unlimited.

13. SUPPLEMENTARY NOTES

14. ABSTRACT

The goal of this project was to measure mid-frequency (1-10 kHz) shallow water reverberation with full companion environmental measurements so that model/data can be compared without ambiguity. Included in the goal was to make statistical estimates of the uncertainties associated with all the environmental conditions. A key element was to understand the mechanisms that cause clutter, approaching the subject by emphasizing contemporaneous environmental and acoustics studies in order to quantitatively understand dominant physical mechanisms. The major components of the research are transmission loss, bottom and sub-bottom impact on propagation and scattering, surface and water column influence on propagation, culminating in a full understanding of the physics of shallow water mid-frequency reverberation. The experiment was conducted off Panama City, Florida, at nominally at 20m water depth to reduce the burden of making environmental measurements.

15. SUBJECT TERMS

mid-frequency, shallow water acoustics, modeling shallow water reverberation, waveguide propagation, target scattering, SONAR equation

16. SECURITY CLASSIFICATION OF:			17. LIMITATION OF ABSTRACT	18. NUMBER OF PAGES	19a. NAME OF RESPONSIBLE PERSON
a. REPORT	b. ABSTRACT	c. THIS PAGE			Dajun Tang
U	U	U	UU	70	19b. TELEPHONE NUMBER *(Include area code)* 206-543-1290

Reset

Standard Form 298 (Rev. 8/98)
Prescribed by ANSI Std. Z39.18